



**HAL**  
open science

# Growth and atomic structure of a novel crystalline two-dimensional material based on silicon and oxygen

Shashank Mathur

► **To cite this version:**

Shashank Mathur. Growth and atomic structure of a novel crystalline two-dimensional material based on silicon and oxygen. Materials Science [cond-mat.mtrl-sci]. Université Grenoble Alpes, 2016. English. NNT : 2016GREAY019 . tel-01486932v1

**HAL Id: tel-01486932**

**<https://theses.hal.science/tel-01486932v1>**

Submitted on 10 Mar 2017 (v1), last revised 13 Mar 2017 (v2)

**HAL** is a multi-disciplinary open access archive for the deposit and dissemination of scientific research documents, whether they are published or not. The documents may come from teaching and research institutions in France or abroad, or from public or private research centers.

L'archive ouverte pluridisciplinaire **HAL**, est destinée au dépôt et à la diffusion de documents scientifiques de niveau recherche, publiés ou non, émanant des établissements d'enseignement et de recherche français ou étrangers, des laboratoires publics ou privés.

## THÈSE

Pour obtenir le grade de

### **DOCTEUR DE LA COMMUNAUTE UNIVERSITE GRENOBLE ALPES**

Spécialité : **Physique De Matière Condensé & Rayonnement**

Arrêté ministériel : 7 août 2006

Présentée par

**Shashank MATHUR**

Thèse dirigée par **Johann CORAUX** et **Pascal POCHET**

préparée au sein du **Département QUEST** de l'**Institut Néel**  
dans l'**École Doctorale de Physique**

# **Croissance et structure à l'échelle atomique d'un nouveau matériau cristallin bidimensionnel à base de silicium et d'oxygène**

Thèse soutenue publiquement le « **16 Septembre 2016** »,  
devant le jury composé de :

**Prof. Pierre MÜLLER**

Professeur des Universités - Aix-Marseille Université (Rapporteur)

**Prof. Florian BANHART**

Professeur des Universités - Université de Strasbourg (Rapporteur)

**Prof. Denis BUTTARD**

Professeur des Université Grenoble Alpes (Président)

**Dr. Muriel SICOT**

Chargé de recherche à Institut Jean Lamour/CNRS- Université de  
Lorraine, Nancy (Examinatrice)

**Dr. Laurence MAGAUD**

Directrice de recherche à l'Institut Néel/CNRS-UGA, Grenoble (Invited)

**Dr. Johann CORAUX**

Chargé de recherche à Institut Néel/CNRS-UGA, Grenoble (Directeur de  
These)

**Dr. Pascal POCHET**

Chercher à INAC-CEA Grenoble (co-Directeur de These)



# Contents

0.1 Organisation of the thesis . . . . .	5
<b>1 Crystalline two-dimensional (2D) materials</b>	<b>8</b>
1.1 2D crystals . . . . .	8
1.1.1 Graphene . . . . .	10
1.1.2 Silicene . . . . .	12
1.1.3 Transition metal dichalcogenides (TMDCs) . . . . .	15
1.2 Ultra Thin Oxides . . . . .	17
1.2.1 Growth and preparation of oxides . . . . .	18
1.3 From three dimensional to two dimensional silicon oxide	21
1.3.1 Polymorphism . . . . .	23
1.3.2 Two-dimensional silicon oxide on metallic surfaces	26
1.3.3 Structure of two-dimensional silicon oxide . . . . .	27
1.3.4 Defects in 2D silicon oxide . . . . .	32
1.3.5 Epitaxy of two-dimensional silicon oxide . . . . .	46
1.3.6 Growth of two-dimensional silicon oxide . . . . .	52
<b>2 Means and Methods</b>	<b>59</b>
2.1 Scanning tunnelling microscopy (STM) . . . . .	61
2.1.1 Principle of operation . . . . .	61
2.1.2 Tunnelling conductance . . . . .	64
2.1.3 Choice and preparation of the STM tip . . . . .	66
2.2 Reflection high energy electron diffraction (RHEED) . . . . .	67
2.2.1 Data interpretation . . . . .	69
2.3 Surface preparations of the single crystals . . . . .	71
2.4 DFT Calculations . . . . .	71

---

<b>3 Atomic structure of epitaxial 2D-silicon oxide</b>	<b>73</b>
3.1 Probing the atomic structure of monolayer silicon oxide on Ru(0001) . . . . .	74
3.2 Epitaxial relation between the monolayer and Ru(0001)	76
3.3 Degenerate epitaxy leading to formation of domains . .	83
3.4 Degeneracy driven defects: anti-phase domain boundaries	86
3.5 Conclusions . . . . .	88
<b>4 Step-by-step analysis of monolayer silicon oxide growth</b>	<b>91</b>
4.1 Growth protocol . . . . .	92
4.2 Oxygen reconstruction on Ru(0001) . . . . .	92
4.3 Silicon deposition . . . . .	96
4.4 Crystallisation leading to silicon oxide . . . . .	99
4.5 Optimisation of the domain size . . . . .	105
4.6 Tentative Mechanism of monolayer silicon oxide formation	107
4.7 Conclusions . . . . .	110
<b>5 Conclusions</b>	<b>111</b>



# Introduction

Two-dimensional crystals, made of only one or few atomic planes, have long focused the attention of the scientific community, accompanying the development of the field of surface science. Within a broad overview, the initial observations could actually be traced back to the 1920s, when Langmuir provided the first experimental observations of organic molecules organising at the surface of liquids [58] [59].

Since then, with the advent of ever higher resolution techniques, including diffraction and microscopy, and ever more powerful numerical calculations, a vast library of systems has been explored and a fine degree of detail has been achieved in their description. Among these two-dimensional crystals were a very unique kind, one in which internal bonds between constituent atoms are strong enough for the crystal to host collective excitations, while the crystal is sufficiently weakly interacting with its environment. In such a case, the collective excitations are truly specific to the low-dimensional crystal. Ironically, while such two-dimensional crystals were long known to surface scientists, it is not until 2006, just two years after graphene could be isolated and studied in micro-devices, that surface scientists realised that they could contribute uniquely to the exploration of the unique properties of two-dimensional materials.

The exciting properties and possible applications of these materials have fostered extensive efforts towards discovery of novel phases. From high speed electronics, to flexible transparent conductors, nano-electromechanical systems, composites and catalytic systems, numerous fields of research have been deeply influenced by possibilities made accessible to two-dimensional crystals.

A recent fraction of the scientific literature refers to ultra thin oxides as two-dimensional oxides. Beyond this fashionable name

---

are concepts which gain significance in the field of two-dimensional crystals, especially considering the combination of properties within reach when stacking distinct two-dimensional crystal together. It is actually well known that ultra-thin oxides with well-defined flat surface are rich playgrounds to understand their complex structure in details, the resulting electronic and chemical properties, which is of utmost importance to understand the behaviour of optical, dielectric, and catalytic behaviours. In this sense, ultra-thin oxide are often considered as simplified models of three-dimensional oxides, which are little accessible to direct experimental scrutiny (e.g. by microscopy). The exciting properties of oxides, when in the form of lamellar two-dimensional crystals, have marginally been addressed so far. One hurdle to their exploration is probably linked to the need for growth processes yielding high quality materials with controlled stoichiometry.

The oxide of silicon is a widely abundant material. It exists in various forms from amorphous to crystalline, bulk to porous and thin films. It is a very common dielectric material and extensively used in catalytic systems. The first preparation of two-dimensional silicon oxide, dating back to 1991 [118], aimed at proposing a model system to study the process of catalysis [22]. Since then two-dimensional silicon oxide was successfully prepared on various substrates, including ruthenium [121], palladium [2], and molybdenum [113], in the form of either a single or a bi-layer. Precise understanding of the structure has long remained debated. It is know generally acknowledged that silicon oxide is composed of sharing corner tetrahedra with Si atoms at their centers and O atoms at their centers. Along the long-standing goal of high-quality preparation over large surfaces, substantial progresses were recently obtained when growing silicon oxide on Ru(0001), in which case a hexagonal tiling of the tetrahedra, with well-defined crystallographic orientation, was demonstrated. The precise atomic arrangement of monolayer silicon oxide was not, at the time this PhD work started, determined by a direct observation, but rather inferred from spectroscopy. Besides, even if monolayer silicon oxides on Ru(0001) shows well-defined crystallographic orientation, it comprises a large density of defects, whose origin was not discussed.

---

Studies based on theoretical calculations and spectroscopies proposed the silicon oxide to comprise of  $[\text{SiO}_4]$  tetrahedra, with oxygen atoms at the apex surrounding a silicon atom - like the bulk silicon oxide. The corner-sharing random network model proposed by Zachariasen [127], in 1932, was shown to be valid for amorphous regime of the bilayer phase [42] [62]; while a hexagonal arrangement of the tetrahedra was revealed for the crystalline regime (of both bilayer and monolayer) [121] [90]. The atomic structure, of the monolayer bound to metal is more involved and complex. Cross-sectional transmission electron microscopy has revealed the monolayer to bind to the support directly via covalent bonds [7]. However studies on deeper information related to the exact epitaxial relationship and bonding nature have relied on density functional theory based calculations, which are under debate. The scanning tunnelling microscopy and transmission electron microscopy based studies have also revealed the sheet to develop in small domain with very specific domain boundaries. It is a quest to resolve this issue of the formation of small domains and associated defects. Formation of these domains is not well understood and need a solution in order to grow large-crystalline sheets that can be employed in devices or subjected to further study by techniques where the resolution is lower than the domain size.

This PhD work is devoted to the study of the growth and structure of monolayer silicon oxide on Ru(0001). This scope was however not the initial one. The PhD thesis, funded by the LANEF Labex, indeed was intended to prepare another two-dimensional material, silicon carbide. After unsuccessful attempts during the first year of the thesis, and considering promising results obtained in the framework of a research project (NANOCELLS) funded by the French National Research Agency, it was decided to re-define the thesis scope to silicon oxide, which is a promising intermediate to silicon carbide. The work was performed in collaboration between Institut Néel (HYBRID team) and CEA INAC (SiNaPS and L.Sim teams).

---

## 0.1 Organisation of the thesis

---

The first chapter of the thesis is a short bibliography review on the topic of two-dimensional materials, from a broad perspective and with a strong orientation towards two-dimensional oxides and silicon oxide in particular. We choose to discuss a few other two-dimensional materials to illustrate important concepts in the field, that are eventually relevant to silicon oxide. Concerning the latter, we focus our attention to the knowledge which existed, at the time this thesis started, on the structure and growth of the material, trying to identify key open questions.

The second chapter is devoted to the experimental methods relevant in our work. After describing the multi-purpose ultra-high vacuum system with which the experiments were done, we discuss specifically two surface science that we have used extensively. Scanning tunneling microscopy (STM), reflection high-energy electron diffraction (RHEED) are accordingly described.

The third chapter addresses the structure of monolayer silicon oxide on Ru(0001). We unveil the precise atomic structure of the oxide with unprecedented structural and chemical resolution thanks to STM and density functional theory calculations, identifying silicon atoms as corners of hexagonal rings and oxygen atoms as bridges between them. We are also able to identify the binding sites of the silicon oxide on Ru(0001) in a non-ambiguous manner. This detailed structural analysis allows us to identify the prominent source of defects in silicon oxides, namely the existence of three energetically equivalent epitaxial relationships. So-called antiphase domains, which are laterally shifted one with respect to the other are formed due to this equivalency, and the pentagon and heptagon chains which form the antiphase boundary cannot be avoided.

In the last chapter, we study, step-by-step, the complex process of silicon oxide growth on Ru(0001). We find that optimizing the quality of the oxygen reconstruction phase preventing silicide formation does not allow to perfect the quality of silicon oxide. We find that silicon oxides crystallizes at high temperature, and that the crystalline domains increase their lattice parameter as they grow. Strictly speaking, the silicon oxide is found not pseudomorphic, which was

---

overlooked in former lower resolution diffraction techniques. We end up with discussing possible elementary processes governing growth, in terms of a displacive transformation of the oxygen reconstruction covered with silicon, along three equivalent directions, as the main source of defects.

# Chapter 1

## Crystalline two-dimensional (2D) materials

### 1.1 2D crystals

---

Two dimensional crystals are ultra thin crystalline materials with single or few atomic planes. They have strong bonds in-plane and usually weak out of the plane bonds. Due to the lamellar structure, hopping of the electron is hindered perpendicular to their plane. This makes these materials wealthy in terms of unique physical phenomena. Large expectations to study these new phenomena supported by continuously developing fabrication and nano-manipulating techniques led to the discovery of graphene in 2004-2005 by K. Novoselov *et al.* [79][80]. This material, for instance, made it possible to address Dirac-Fermion-like physics in table-top experiments. The sheet being efficient conductor of heat and charge is considered for multiple applications, from transparent conductors to super capacitors. Since then, many other materials in a two-dimensional phase, like transition metal dichalcogenides (TMDCs) [17], silicene [46] and ultra thin (or layered) oxides [33] have revealed other kinds of unique properties, very different from bulk. Furthermore, in some cases (*e.g.* oxides), the few-atomic planes materials represent ideal structure sharing common features with the bulk counterparts, yet unlike the latter, being accessible to much broader range of experimental probes. A tentative library of 2D crystals taken from [35] is shown in Figure 1.1.

graphene family	graphene	hBN 'white graphene'	BCN	fluorographene	graphene oxide
	2D chalcogenides	MoS <sub>2</sub> , WS <sub>2</sub> , MoSe <sub>2</sub> , WSe <sub>2</sub>		semiconducting dichalcogenides: MoTe <sub>2</sub> , WTe <sub>2</sub> , ZrS <sub>2</sub> , ZrSe <sub>2</sub> , etc.	metallic dichalcogenides: NbSe <sub>2</sub> , NbS <sub>2</sub> , TaS <sub>2</sub> , TiS <sub>2</sub> , NiSe <sub>2</sub> , etc.
2D oxides		micas, BSCCO	MoO <sub>3</sub> , WO <sub>3</sub>	perovskite-type: LaNb <sub>2</sub> O <sub>7</sub> , (Ca,Sr) <sub>2</sub> Nb <sub>3</sub> O <sub>10</sub> , Bi <sub>4</sub> Ti <sub>3</sub> O <sub>12</sub> , Ca <sub>2</sub> Ta <sub>2</sub> TiO <sub>10</sub> , etc.	hydroxides: Ni(OH) <sub>2</sub> , Eu(OH) <sub>2</sub> , etc.
	layered Cu oxides	TiO <sub>2</sub> , MnO <sub>2</sub> , V <sub>2</sub> O <sub>5</sub> , TaO <sub>3</sub> , RuO <sub>2</sub> , etc.		<b>OTHERS</b>	

Figure 1.1: A tentative library of 2D crystals. The blue shaded region comprise in the materials that are stable in air; in green are the materials for which the stability in air is debated; in orange are those which are stable under inert atmospheres and in grey are the crystals which have been exfoliated but lack extensive studies. Adapted from [35].

In nature there exist many 3D crystals with layered structures. From such crystals where the inter-layer interaction is only via van de Waals' forces ( $\sim 40$  to  $70$  meV per atom), which is not very strong, a single layer can be delaminated. The process of delimitation can be performed chemically or mechanically, commonly called exfoliation. The mechanical exfoliation process involves an adhesive tape to pick up single- or few- layers from the stack and place them on desirable substrates, like SiO<sub>2</sub>. In chemical exfoliation, a chemical species is intercalated into the 3D-layered crystal. Tetrabutyl ammonium ions [67] or atoms like Li [109], K, Cl or Br *etc.* are the common chemical exfoliants and have been shown to decrease the energy needed to exfoliate graphite by up to a factor of 5. In addition to graphene other lamellar bulk crystals including oxides like titanium oxide, molybdenum oxide and manganese oxides along with several others [67], can be efficiently exfoliated by these techniques. On the other hand, epitaxial growth is an efficient way to grow large scale 2D crystals on crystalline substrates [128]. Using liquid phase or gaseous phase precursors, decomposed or combined at the surface of a substrate, 2D crystals can be grown from the bottom-up approach, in some cases with good or even well-defined crystalline orientation. Such techniques can also be applied to stabilise structures which

---

do not have a layered 3D counterpart, like silicene [104], or some phases of silicon oxide for instance. Depending on the chemical properties of the substrate and of the two-dimensional material, the bonds between both may vary from weak van der Waals ones, to strong covalent ones.

In the following sections we discuss in a partial way the nature and properties of a few materials. Graphene is discussed as the most emblematic example of a two-dimensional crystal, then silicene, transition metal dichalcogenides and layered oxides which noteworthy raise the important questions of the chemical stability and of polymorphism in two-dimensions. In the section on layered oxides we elaborate on silicon oxide which is further presented in this thesis.

### 1.1.1 Graphene

Graphene is a two-dimensional sheet made up of carbon atoms tightly packed into a honeycomb lattice, (Figure 1.2 (a)). It is the building block of all graphitic forms of carbon: fullerenes can be obtained by wrapping [54], carbon nanotubes [43] by rolling and graphite by stacking. The  $sp^2$  hybridisation of carbon bonds account for many of the physical properties in these materials. The  $\sigma$  bonds between the carbon atoms are strong covalent ones with bond energy of 3.1 eV making graphene the strongest known material with Young's modulus of 1 TPa and intrinsic strength of 130 GPa. The  $2p_z$  orbitals perpendicular to the graphene plane form the  $\pi$ -bonds.  $\pi$  electrons are delocalised; the presence of two carbon sub lattices per unit cell and possible hopping of electrons between and within these sub lattices yielding a valence and conduction band touching at a set of points (high symmetry  $K$  points of the Brillouin zone). Around these points, the so-called Dirac points lying at the Fermi level ( $E_F$ ) in pristine graphene, the two bands disperse linearly. This behaviour is linked to Dirac-Fermion-like behaviour often described in graphene [78]. The exfoliation of single layer from highly oriented pyrolytic graphite (HOPG) using an adhesive tape and the demonstration of the ambipolar electric field effect in the metallic monolayer in 2004, thanks to nano-fabrication, ignited widespread interest which led to the award of the Nobel prize to K. Novoselov and A. Geim in 2010.



---

To circumvent the shortcomings of mechanical exfoliation, *i.e.* its low yield and small size of the graphene flakes it yields, growth of graphene on the well-defined surface of substrates has been developed. Thermal decomposition of carbon precursor – so called chemical vapour deposition (CVD) – and temperature induced silicon sublimation from SiC are two main routes [47].

Defects are of several kinds. A common defect is a linear delamination, called wrinkle, which forms upon cooling down of the samples after growth, due to the mismatch of the thermal coefficient of graphene and the substrate and the high stiffness of graphene [60]. Other typical linear defects are grain boundaries, which form due to mis-orientation or lateral displacement [19] [123] of single crystal graphene domains. The former are frequently encountered in systems for which the interactions between graphene and the support underneath is weak, *e.g.* Pt(111) [102]; Ir(111) [21] or in multilayer graphene/SiC(000 $\bar{1}$ ) [29] [23]. The latter case is less discussed and was only reported to our knowledge on Ni(111) [55]. On this substrate, graphene's lattice parameter almost matches with that of the metal ( $\sim 1\%$  difference) and thus graphene binds in commensurate ( $1 \times 1$ ) manner. This epitaxial relationship can be realised in two almost equivalent (hence almost degenerate in energy) ways, with either one or the other carbon sub lattice on top of a surface Ni atom. The two kinds of epitaxy yield domains which are shifted one with respect to the other but have equal crystallographic orientations. The grain boundaries are constituted of non-hexagonal rings of different kinds and density which usually allow for stitching the graphene domains while avoiding the formation of carbon dangling bonds (Figure 1.2 (c-e)).

The electronic properties of epitaxial graphene are expected to be influenced by the metallic support, all the more as its bonds with graphene are stronger. Due to this reason the sheet is often transferred after growth and placed onto inert substrates like silicon oxide on silicon (SiO<sub>2</sub>/Si) [4] or hexagonal-boron nitride (h-BN) [25]. The transfer process includes various etching and adhesive related steps that are liable to induce defects in graphene [61]. An alternative approach consists in intercalation of species that will quench the graphene-substrate interaction [103] [50]. Intercalation also permits

---

to engineer the properties of graphene, for instance to induce electronic band-gaps [94] [40] [40], magnetic moments [114] [87], and strains [91]. Sequential intercalation of Si and O atoms was shown to yield silicon oxide between graphene and a Ru(0001) substrate [65] [74]. Four probe surface resistance measurements on samples gave first hints of a fully decoupled graphene without the need of a transfer (Figure 1.2 (f-g)).

### 1.1.2 Silicene

Silicene is another homo-elemental two-dimensional crystal based on silicon, analogous to graphene. A free-standing silicene consists in a single layer of silicon atoms with a hexagonal arrangement. In the most stable configuration, silicene is predicted to be buckled with a vertical separation between top and bottom silicon atoms,  $\delta \sim 0.44 \text{ \AA}$  [104]. The large length of Si-Si bonds prevents a pure  $sp^2$  hybridisation and the formation of  $\pi$ -bonds. The buckling yields large orbital overlap leading to a mixed  $sp^2 - sp^3$  hybridisation. Similar to graphene, silicene is predicted to be gap-less semiconductor with a Dirac cone at the  $K$ -point of the Brillouin zone. The buckling influences the electronic properties of silicene and makes it prone to symmetry breaking by various stimuli [130]. An application of an electric field perpendicular to the plane of silicene leads to a charge transfer between the buckled atomic planes breaking the inversion symmetry, and is predicted to open a band gap at the  $K$ -point. A mechanical bi-axial tensile strain larger than 5% is expected to weaken the Si - Si bonds leading to hole doping [45]; while a uniaxial strain breaks the symmetry [130], both inducing a band gap opening. On application of out-of-plane electric field [39], a topological phase transition from a quantum spin Hall state to a trivial insulator has been also predicted due to the spin-orbit coupling in silicene.

There is no natural material composed of stacks of silicene monolayers and thus mechanical exfoliation cannot be employed to produce silicene.. The silicene sheets are thus grown using a bottom-up approach in ultra high vacuum chambers by molecular beam epitaxy (MBE) [110] [56] [75] [30]. Only a few metals are suitable as sub-

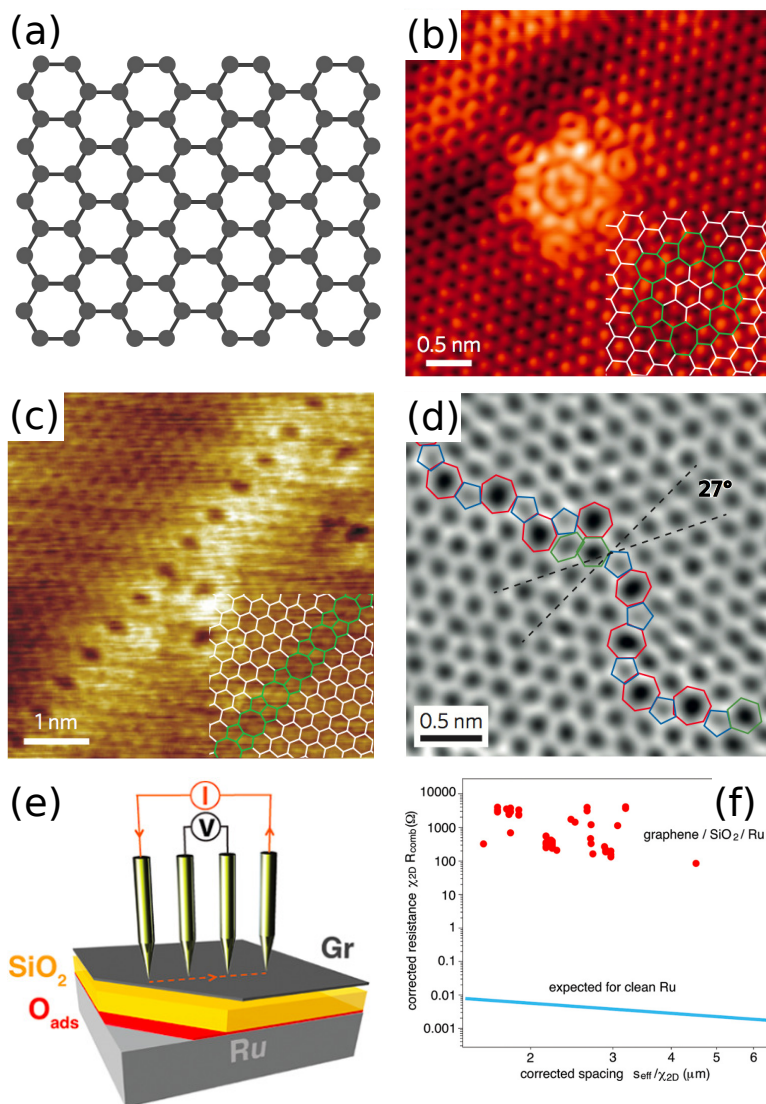


Figure 1.2: A short description of graphene. (a) Honeycomb lattice, (b) Flower defect, (c) A domain boundary stitching in-plane shifted graphene domains, (d) twin boundary stitching domains rotated by 27°, (e) model of silicon oxide intercalation between graphene and Ru(0001), (e-f) four-probe measurements plot between resistance and contact spacing showing effective decoupling of graphene from Ru(0001). Adapted from [11][55][65] [19].

---

strates due to the tendency of Si atoms to form silicides. Silicene grown on Ag(111) shows a complex structure with  $(4 \times 4)$  silicene cell on  $(4 \times 4)$  Ag cells (Figure 1.3 (a)). The silicene lattice in this configuration has 6 atoms in the top plane and 12 in the bottom plane. This in-equivalency in the number of silicon atoms in the two planes results in a band gap of 0.3 eV, primarily due to breaking of the inversion symmetry. The strong substrate - silicene sheet interactions can also lead to gap opening, as observed on Ir(111) [75],  $\text{ZrB}_2(0001)$  [30] and proposed on  $\text{ZrC}(111)$  [1]. To avoid this effect and maintain a free-standing and minimally interacting silicene layer, the growth of monolayer on  $\text{MoS}_2$  substrates [18] has been performed and other materials like AlN or ZnS have been proposed as supports for silicene.

X-ray photoelectron spectroscopy studies of the silicene sheet revealed that exposures to 1000 L (langmuir) of oxygen results in a minor oxidation of the silicene. However, exposing the silicene to atmospheric conditions leads to a complete transformation of the silicene to silicon oxide, as shown by a strong increase of the signal corresponding to  $\text{Si}^{4+}$  core levels [77]. DFT calculations show that the oxidation level of silicene in oxides can range from 1+ to 4+ depending on the amount of oxygen involved in the system. These different oxidation states impose very different properties in silicene oxides, from metallic to insulating [112].

### **1.1.3 Transition metal dichalcogenides (TMDCs)**

Transition metal-dichalcogenides (TMDCs) are two-dimensional crystals with more than one type of atoms. The TMDC monolayers consist of three atomic planes, one of a transition metal atoms (M) (group 4 to 7 elements like Mo, W, Ti, Zr) in a triangular lattice which is sandwiched between two planes of chalcogen atoms (X) (S, Se, Te), with a general formula  $\text{MX}_2$ . Each layer is 6-7 Å thick [122]. The interlayer M-X bonds are covalent in nature, while the layers stack with weak van der Waals' forces to form multilayers or the bulk 3D-crystals. The metals provide four electrons to bind such that the oxidation state of metal and chalcogen atoms are 4+ and 2- respectively. In case of sulphides the layers are stable and non-reactive to

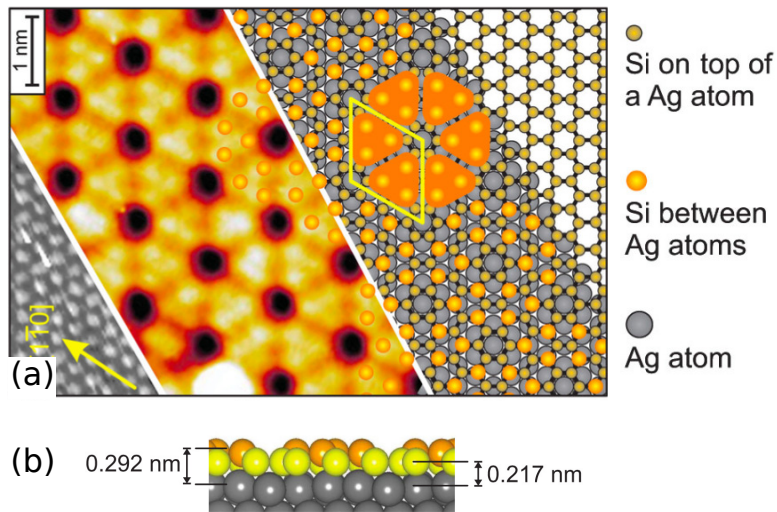


Figure 1.3: Structure of silicene on Ag(111): (a) Top view, (b) Side view. Adapted from [110].

the environment due to absence of dangling bonds and strength of M-S bonds. The metal coordination can be trigonal or hexagonal of which either can be preferential. 1T (trigonal) and 2H (hexagonal) are the most common polymorphs in monolayer TMDCs.

The electronic properties of the TMDCs strongly depend on the coordination environment (the kind of polymorph) of the transition metal and the  $d$ -electrons it provides. Octahedrally coordinated M forms two degenerate  $d$ -orbitals containing  $d$ -electrons; while the  $d$ -orbitals split into three for trigonal M with sizeable band gap between two. The semi-filled orbitals lead to the metallic nature in NbS<sub>2</sub> & VSe<sub>2</sub> while fully-filled orbitals give rise to semiconducting nature in MoS<sub>2</sub> and WS<sub>2</sub>. The chalcogen atom can also tune the electronic band gap. An example is the band gap decrease from 1.3 to 1.0 eV in the MoS<sub>2</sub> → MoSe<sub>2</sub> → MoTe<sub>2</sub> sequence [116]. Interestingly, the band gap of MoS<sub>2</sub> shows a transformation from an indirect band gap to a direct band gap in monolayer state (Figure 1.4 (e)) [70].

The number of  $d$ -electrons also sets the preferred phase of the TMDC. The phase of the TMDC can thus be tuned or altered by changing the number of  $d$ -electrons *via* doping for instance with an electron donating species like an alkali atom [28]. The phase transformation has been shown to be a reversible process [68].

The TMDC monolayers can be exfoliated mechanically using an adhesive tape or chemically using exfoliating intercalates, similar to graphene. These layers can also be grown bottom-up using atomic or molecular species with chemical or physical vapour deposition [111]. Common defects in TMDC layers grown by the bottom-up approach are rotational grain boundaries [129] which exhibit structures reminiscent of graphene. The coexistence of 1T and 2H phase yield a special kind of defect, grain boundary consisting of zigzag lines [27].

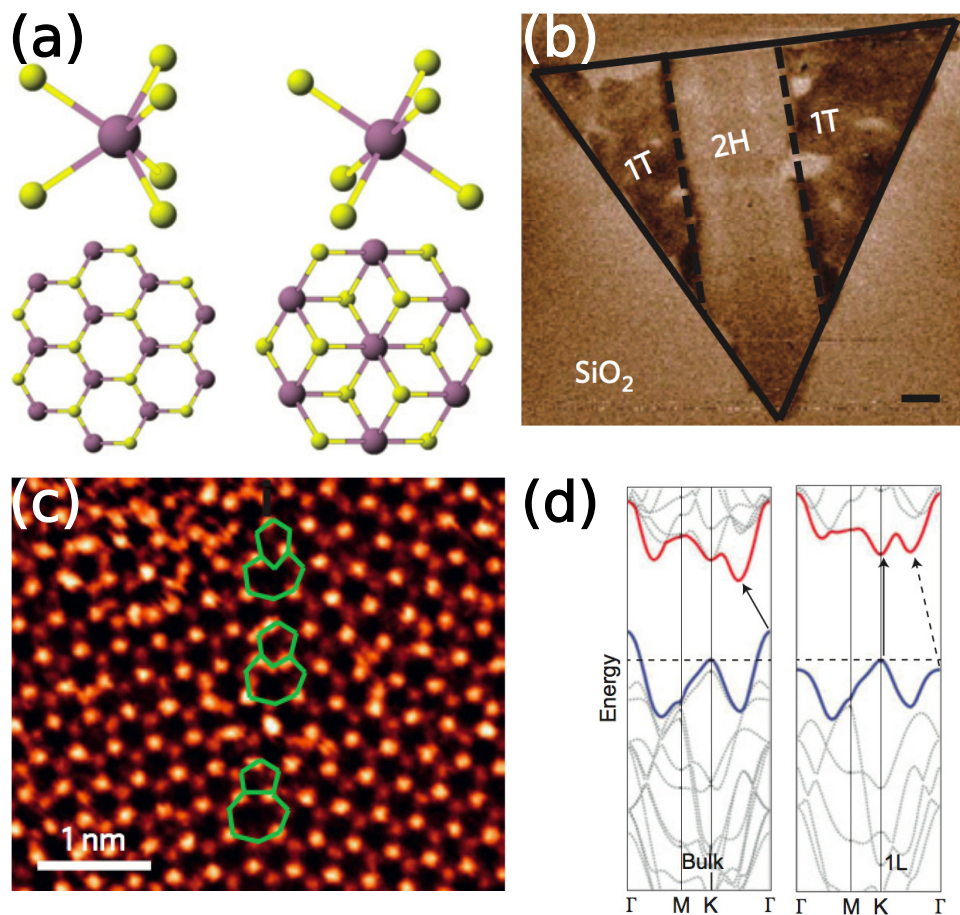


Figure 1.4: Transition metal dichalcogenides. (a) 2H (left) and 1T (right) phases of MoS<sub>2</sub>, (b) Electrostatic Force Microscopy on MoS<sub>2</sub> flake showing 2H (bright) and 1T (dark) regions, (c) a dislocation boundary in MoS<sub>2</sub>, (d) Electronic band structure in bulk (left) and monolayer (right) of MoS<sub>2</sub>. Adapted from [17] [131].

---

## 1.2 Ultra Thin Oxides

---

Ultra thin oxide films are materials with versatile and tailorable properties and applications. Like other two-dimensional materials, ultra thin oxides include films that are limited to few unit cells in the thickness dimension. The bond between the oxygen and the other kind of atom (A) usually has mixed covalent and ionic character [26]. The ultra thin oxides are usually grown on metal surfaces. The relative strength of the bonds with the substrate and of the A-O bond drives the crystallinity of the oxide film. For instance, trilayer oxides  $\text{VO}_2$ ,  $\text{MnO}_2$  or  $\text{CoO}_2$ , which have weak interaction with their substrate form incommensurate and disordered layers [85]. On the contrary, a highly crystalline and commensurate structures form in monolayer  $\text{V}_2\text{O}_3$  on  $\text{Pd}(111)$  [53].

Large epitaxial stress at the oxide–metal interfaces are found as a result of the lattice mismatch at the interface between the two materials. Lattice mismatches as high as 40% in case of ceria(111) on  $\text{Pt}(111)$  or 5% between  $\text{MgO}$  and  $\text{Mo}(001)$  can be relieved by formation of structural defects which stabilise the system along with slightly altered lattice parameters. Interestingly, monoxides (MO) like  $\text{MnO}$ ,  $\text{CoO}$  and  $\text{NiO}$  form a  $c(4 \times 2)$  metal vacancy networks on the surface of  $\text{Pd}(100)$  to release the strain [32]. This leads to an actual stoichiometry of  $\text{A}_3\text{O}_4$ . The  $c(4 \times 2)$  nickel oxide and cobalt oxide form large single crystalline domains while manganese oxide forms small ordered domains, as seen in Figure 1.5 (a).

Apart from epitaxial strain, the chemical potentials of the species also govern the structure of the oxide layer to great extents, all the more in the case of an A atom liable to have different types of oxidation states (Figure 1.5 (b)). Manganese oxide films are reported to form more than nine different  $\text{MnO}_x$  phases at different O chemical potentials. Depending on the oxygen chemical potential, phases with higher and lower oxidation states of Mn are for instance observed at 0.7ML coverage [31].



### 1.2.1 Growth and preparation of oxides

The use of ultra clean conditions found in UHV systems has proven advantageous to the growth of ultra thin oxides with controlled oxidation state of the A atom. The preparation is performed on a substrate, often a metal, with crystal structure similar to that of the oxide so that a well-defined epitaxial relationship can occur preferentially. Techniques for the fabrication of the ultra thin oxides include (i) Reactive evaporation, (ii) Post-oxidation, and (iii) chemical vapour deposition.

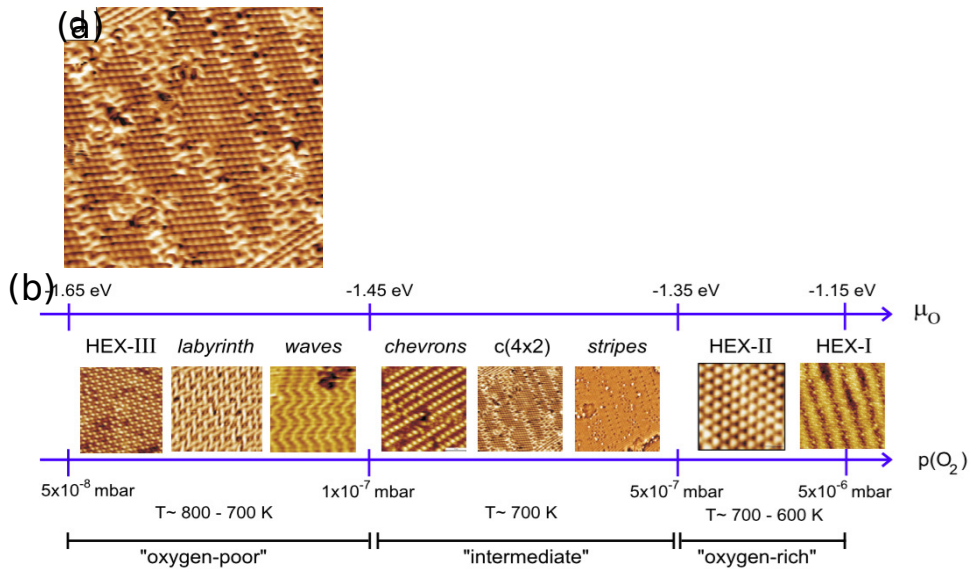


Figure 1.5: (a) Stress relief defects in manganese oxide layer grown on Pd(100) and corresponding crystalline structure revealed by STM, (b) phase diagram of manganese oxide as a function of chemical potential of oxygen. Adapted from [31].

Reactive deposition is a physical vapour deposition method. In this method, the deposition of the desired element (A) is performed in a back pressure of an oxidising agent, usually oxygen. The deposition is done from a physical vapour deposition technique, like electron beam or ion sputtering, thermally or with help of laser ablation, on the substrates for epitaxy. For example, different combinations of temperature of deposition and partial pressures of oxygen during the growth of MnO on Pd(100) promote the growth of specific phases,



---

shown in Figure 1.5. The phases form at different temperature under a specific chemical potential of oxygen. Reactive deposition is also applied to prepare stoichiometric films of complex oxides like strontium titanate. Monolayer and bilayer silicon oxide on Mo(100) and Ru(0001) have been prepared on oxygen pre-covered surface in a reactive deposition manner, discussed later.

Post-oxidation is another widely used method to grow ultra thin oxides. It involves deposition of thin films on the substrates followed by annealing to high temperature under oxygen atmosphere. Heteroepitaxy of FeO on Pt(111) and Pt(100) surfaces by deposition of Fe films on the substrate and its post oxidation have shown a layer-by-layer growth mechanism. The initial dose of the A atoms has been shown to be critical to obtain an epitaxial film of the oxide, specifically on NiO growth on Pd(100). This method has been shown to grow highly stoichiometric films of oxides by repeated annealing cycles that helps in overcoming issues of O diffusion in thick films.

Chemical vapour deposition (CVD) is another method to grow large-scale sheets at low costs. For instance, the growth of ultra thin MgO in cubic structure on Si, sapphire and quartz can be achieved by CVD. The process involves transporting the vapours of the precursor, mainly organo-metallic compounds, to the substrate where the reaction in homogenous or heterogeneous phase results in the formation of the metal oxide sheet. The substrate, precursor and the growth temperature influence the growth kinetics and the crystallinity of the films. This method usually gives less control over stoichiometry than the earlier discussed physical vapour deposition technique of reactive deposition. Often, the residues of the unreacted precursor are left on the substrate.

Ultra thin oxides like alumina ( $\text{Al}_2\text{O}_3$ ) and tin oxide ( $\text{SnO}_2$ ) have also been grown in a modified CVD method, named atomic layer deposition, consisting in sequential cycles of exposure to gaseous precursors. In every cycle, the single precursor reacts with the substrate and self-limits the deposition of more than a monolayer. The second cycle exposes the surface to a second precursor which forms the desired atom layer upon reaction with the first precursor. The layers grown are flat and highly crystalline.

Exfoliation of lamellar oxides from three-dimensional stacks held

---

by van der Waals forces has been an interesting way of achieving ultra thin oxides. Like other two-dimensional materials, layered oxides have been exfoliated using chemical ions like tetrabutylammonium, propyl ammonium [67].

### **Applications of ultra thin oxides**

Oxides find applications in the field of microelectronics as dielectric layers for capacitive control of the density of charges, due to its high permittivity, and in heterogenous catalysis in form of high specific area porous compounds showing great thermal stability and specific catalytic activity. On resorting to ultra thin or layered oxides, many limitations of the bulk oxides can be overcome and new properties can be tailored easily leading to multiple potential applications. The ultra thin oxides have well-defined and readily identifiable structure which resembles the structure of the inner walls of the bulk oxide catalysts. Thus it gives opportunity to access and monitor the process of catalysis directly, which otherwise heavily relies on theoretical calculations and macroscopic phenomenological approaches. Another well-known application of oxides like MgO are tunnelling barrier between two ferromagnetic electrodes, for highly efficient spin-valves [126]. The crystallinity of the ultra thin oxides proved critical to improve the magnetoresistance which now reaches 180%, in contrast to 70% with amorphous oxides like aluminium oxide [5] .

The ultra thin oxides find various applications in the field of rapidly miniaturising electronic devices. Decreasing the thickness of the dielectric layers, in order to increase this capacitance, hence to decrease the potential difference needed to induce a given charge (density), is of major interest in this respect. However, traditional oxides comprise dead layers [84] [15] of non-stoichiometric composition, and have electronic states which yield significant current leakage as this thickness decreases. Hence, rather than reducing thickness, most efforts are so far focussed on dielectric material with increased permittivity. High quality crystalline ultra thin oxides allow for an alternative approach, as they circumvent the main drawback (leakage at very low thickness). Such lamellar oxides indeed have a permittivity which is independent of their thickness, as it was shown with

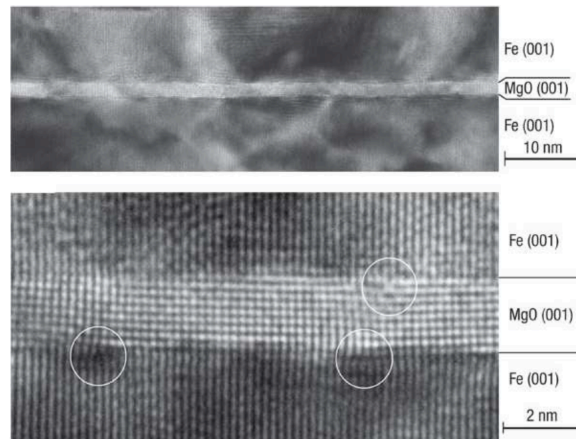


Figure 1.6: Magnetic tunnel junction (MTJ) formed of ultra thin crystalline MgO films sandwiched between two ferroelectric electrodes of Fe. The cross-sectional transmission electron microscopic image shows the crystalline interface between the oxide and the electrodes. Adapted from [126].

$(\text{Ca}_2\text{Nb}_3\text{O}_{10})_n/\text{SrRuO}_3$  perovskite oxide [81] (Figure 1.7).

### 1.3 From three dimensional to two dimensional silicon oxide

Silicon oxide, commonly known as silica (derived from greek word *silex*) is an abundant material in the universe. It is composed of oxygen and silicon. The electronic configuration of silicon is  $1s^2 2s^2 2p^6 3s^2 3p^2$ . In agreement to the octet rule, Si, like C, tends to form four bonds, and oxygen forms two-bonds. The SiO bonds are of mixed covalent and ionic character, with about half the charges in the six electron pairs transferred from Si to O [83]. Silica may have been intriguing to the mineralogists and geologists due to its extremely rich phase diagram showing extensive polymorphism, a notion which we will introduce in section 1.3.1. It exists in both crystalline and amorphous forms with diverse physical properties making it vital in modern technology. Silica has a porous structure that leads to adsorption of various species in the bulk. The adsorbates can be in the form of impurities that cause change in

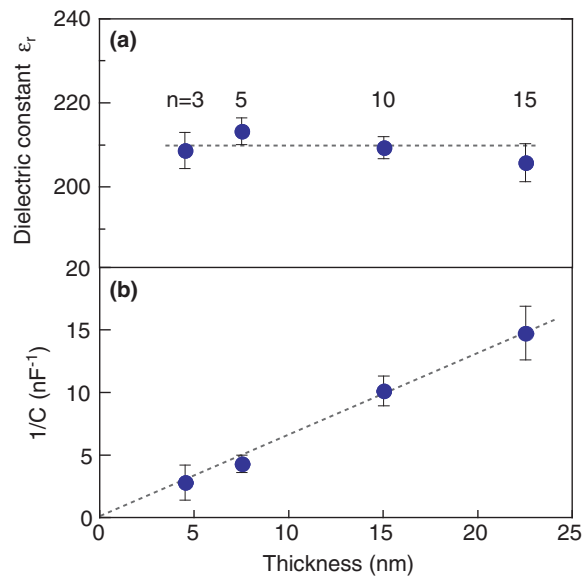


Figure 1.7: (a) The dielectric constant value as a function of thickness of  $(\text{Ca}_2\text{Nb}_3\text{O}_{10})_n$  film. The dielectric constant value does not change on varying the thickness. (b) The reciprocal capacitance from ultra thin films of oxide is a linear function of the thickness that passes through a zero value showing no charge due to a dead layer commonly observed on bulk dielectrics [81].

---

properties of silica, for instance inducing different colours (like blue to pink on water adsorption). These adsorbates can also be in form of metal clusters possessing specific catalytic activity [12]. This makes silica an important component in heterogenous catalysis, as a porous support. Intrinsic catalytic activity of the silica as a solid catalyst has also been evident. Due to the very small coefficient of thermal expansion, silica has the ability to mechanically withstand sudden and large changes in temperature. The amorphous silica has very high ultraviolet transmission and so is used to manufacture optical elements like lenses. The purity of silica and its thermal properties enable its use in the fabrication of semiconductor devices. It can be easily deposited on various materials and thermally grown on silicon wafers. The high dielectric strength and wide band gap makes it an excellent insulator. With these properties it is extensively used in the micro-electronics industry.

### **1.3.1 Polymorphism**

The structure of silica is based on  $\text{SiO}_4$  tetrahedra, and the 1:2 ratio of  $\text{SiO}_2$  requires that each oxygen atom is shared between two tetrahedra. Even though the basis is very simple, silica exhibits multiple crystalline phases (polymorphs). The relative stability of the  $\text{SiO}_2$  polymorphs is displayed in the rich and intricate phase diagram (Figure 1.8). There are three common polymorphic structures of silica: quartz, cristobalite and tridymite. These three forms are found as minerals under atmospheric conditions. At atmospheric pressure, the quartz phase is stable from low temperature to  $857^\circ\text{C}$ ; tridymite is stable between the temperature range of  $857^\circ\text{C}$  to  $1470^\circ$  and cristobalite is stable from  $1470^\circ\text{C}$  to the melting temperature of  $1713^\circ\text{C}$ . The high pressure polymorphs of silica are coesite and stishovite. Stishovite is a rare mineral formed of octahedra of Si. The structure of quartz, cristobalite and tridymite appear simple modifications of each other, but they are not readily interconvertible. The way the tetrahedra are linked is actually very different. To transform from one polymorph to another breaking bonds and forming new ones would be required. This kind of phase transformation is termed as reconstructive transformation. Each polymorph has its own low

---

temperature forms ( $\alpha$ ) and high temperature forms ( $\beta$ ). While the high temperature forms have high symmetry, the low temperature forms have reduced symmetry and bent bonds. When the temperature is changed, the high and low forms transform rapidly into the other by bond bending. This kind of transformation has been termed as displace transformation.

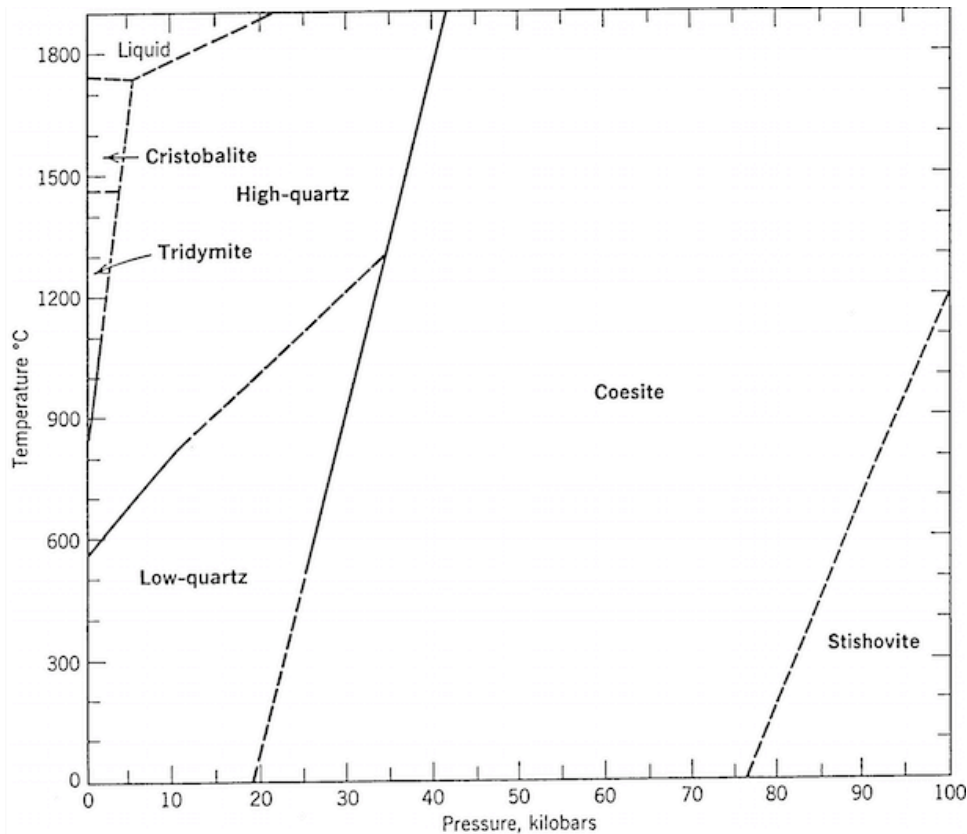


Figure 1.8: Phase diagram of silica.

Quartz has a structure based on chains of three-fold spirals parallel to the c-axis. The spirals are joined by their corners to form large double spirals. These spirals can be right or left handed giving rise to right or left handed crystals. These crystals are mirror-images to each other and are called enantiomorphs.

Tridymite and cristobalite have similar tetrahedra linking pattern. They form layered structures with alternating [SiO<sub>4</sub>] tetrahedra pointing up and down and arranged in a hexagonal lattice, as discussed earlier. The layers are stacked with interlayer bonding through a

shared corner of  $[\text{SiO}_4]$  tetrahedra. The hexagonal symmetry allows linking in multiple manners leading to different stacking sequences. Cristobalite has an ABCABC... and face-centred structure with layers parallel to (111) planes; while tridymite is stacked in an  $\text{AB}'\text{AB}'\dots$  sequence with hexagonal structure with layers parallel to (001) planes (Figure 1.9 (b,c)). The B layer corresponds to a  $180^\circ$  rotation of A. Although the structure of the tridymite and cristobalite are similar, transforming one into the other implies a reconstructive transformation.

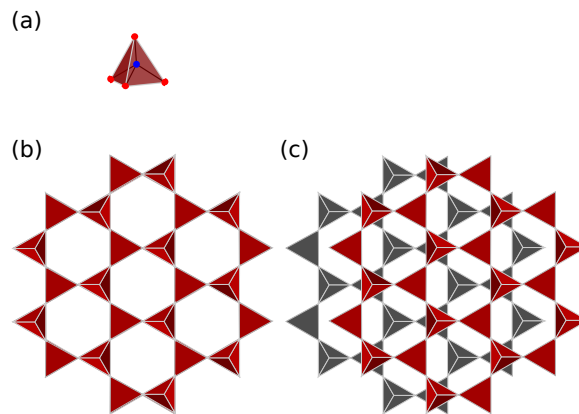


Figure 1.9: (a) Tetrahedron of  $[\text{SiO}_4]$ . (b) The  $\text{AB}'\text{AB}'\dots$  layered structure of tridymite. (c) The ABCABC... layered structure of cristobalite.

Apart from the pure crystalline phases of silica, sheet of silicates, termed as phyllosilicates, exist in nature. Minerals like mica, serpentine and clays belong to this group. In phyllosilicates, the corner-sharing  $[\text{SiO}_4]$  tetrahedra form a tetrahedral layer of hexagonal rings with all tetrahedra pointing in the same direction. These layers bind to Mg or Al forming the octahedral layers which are covalently bonded to another tetrahedral layer of  $[\text{SiO}_4]$  (Figure 1.10). This tetrahedral-octahedral-tetrahedral layers are held together with Al or Mg separating them. The individual layer of  $[\text{SiO}_4]$  is similar to the two-dimensional phase of silicon oxide, discussed in detail in this thesis.

Amorphous silicon oxide grows readily on the surface of silicon wafers exposed to atmosphere. The compound contains majorly  $\text{SiO}_2$ . The oxygen atoms diffusing through the surface break the Si-Si bonds and transform into Si-O-Si. The oxide has a lattice mismatch

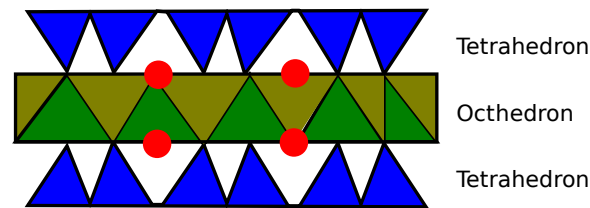


Figure 1.10: Structure of a layered silicate mineral. Two layers of tetrahedron sandwich a metal containing octahedral layer.

of  $\sim 25\%$  with the silicon wafer. Thus no crystallinity is maintained and the oxide forms a disordered structure on silicon. The interface between the silicon oxide grown on silicon has been subjected to multiple studies. But the poor quality and disordered nature hinders conclusive results describing the structure of the interface.

### 1.3.2 Two-dimensional silicon oxide on metallic surfaces

The two-dimensional phase of silicon oxide has been recently under extensive study. Like in bulk, two-dimensional silicon oxide has multiple phases. These two-dimensional phases have been proposed as the ultimately thin dielectric material for microelectronics. Being composed of silicon and oxygen atoms, it is expected to be compatible to the current nano-fabrication technology. The local structure of the phases of two-dimensional silicon oxide are similar to that of some catalytic systems, for instance mobile composition of matter (MCM-41) that contains regularly arranged mesopores. These pores can be used to store atoms and active catalysts for the purpose of heterogenous catalysis. The two-dimensional phase of silicon oxide has also been shown to efficiently isolate graphene from its metallic substrate. As discussed in the previous section, silicon oxide exists in nature in a layered stack structure. But the stacks are not lamellar due to which the mechanical exfoliation of a mono- or a bi- layer is not possible, unlike stacks stabilised only by the van der Waals interaction. The two-dimensional phase of silicon oxide is, thus, grown epitaxially by a bottom-up approach in ultra high vacuum conditions. Works on the growth of a two-dimensional phase initiated with low



---

temperature deposition of silicon atoms on an oxygen-covered Mo surface, followed by oxidation at high temperatures. Since the two-dimensional phase of silicon oxide is more conductive than its bulk counterpart, multiple characterisation techniques could be used to determine the characteristics of this new phase of silicon oxide. The studies based on STM, TEM, IRAS, XPS, LEED, RHEED and DFT are discussed in detail in the following sections. The growth and epitaxy of two-dimensional silicon oxide is also described in detail.

### 1.3.3 Structure of two-dimensional silicon oxide

The 2D phase of silicon oxide, like bulk silicon oxide, comprises  $[\text{SiO}_4]$  tetrahedra and depicts two phases under different thermodynamic conditions. These two phases or polymorphs of 2D silicon oxide are composed of honeycomb atomic lattices (Figure 1.11 (a)) and are identified as monolayer [89] and bilayer [42] [121]. The bilayer comprises two layers of a corner sharing tetrahedra in a honeycomb lattice (Figure 1.11 (b)). All the tetrahedra in each layer point in the (same) direction towards the second layer. The upper and lower layers join together by corner-sharing between the tetrahedra. This is in contrast to bulk silica phases of  $\beta$ -cristobalite and tridymite where one-half of the tetrahedra of the lattice point in opposite direction than the other-half. Two-dimensional silicon oxide depicts the arrangement of the tetrahedra resembling with the structure of the phyllosilicates (Figure 1.10) where the tetrahedra point in the same directions. This bi-layer phase of two-dimensional silicon oxide is completely saturated and thus is stable in nature (with no dangling bonds). A single layer of the tetrahedra, from the bilayer, can also be stabilised on suitable surfaces, and is known as monolayer [16]. The monolayer has been so far stabilised on metallic substrates with high oxygen adsorption energy and lattice matching [124]. The ball models of the two-dimensional phases are shown in Figure 1.11.

A multiple-technique approach including LEED, STM, XPS, IRAS, TEM and DFT has been used to determine the atomic structure of the two-dimensional phases of silicon oxide. The hexagonal lattice of bilayer silicon oxide, with a lattice parameter of  $5.4 \text{ \AA}$ , with high crystallinity denoted by a sharp and bright diffraction pattern has

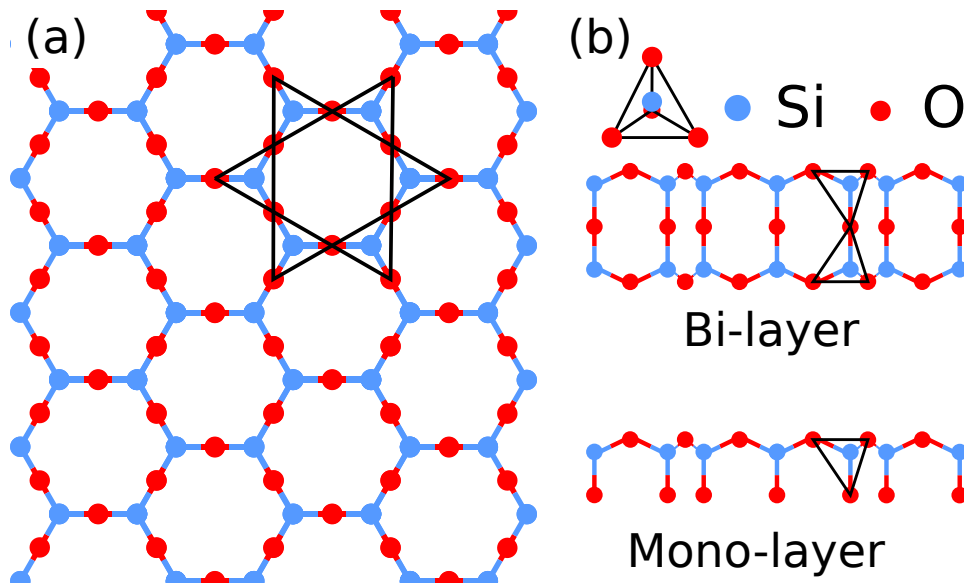


Figure 1.11: The two-dimensional phases of silicon oxide are shown. (a) Top-view shows the hexagonal arrangement of the tetrahedra marked with black triangles. (b) Individual tetrahedron is shown along with side-views of bi-layer and monolayer silicon oxide.

been put in evidence in LEED experiments [66] [42] [2]. This stands in agreement with the parameter obtained by DFT calculations on the free-standing bi-layer silicon oxide [34] [36]. Scanning tunnelling microscopy (STM) and annular dark field (ADF) imaging in scanning transmission electron microscopy (STEM) have resolved the hexagonal lattice down to atomic resolution. In Figure 1.12 (b) the hexagons formed by six bright protrusions forming the corners of the hexagons in STM micrographs, marked with blue balls, can be seen. These bright corners were also observed in the ADF measurements shown in Figure 1.12(c). These bright protrusions were found to be silicon atoms by DFT simulations of the ADF images. These silicon atoms belong to individual corner sharing  $[\text{SiO}_4]$  tetrahedra forming the lattice of bilayer silicon oxide. In this structure, every silicon atom is bonded to four oxygen atoms; of which three form the bases of the tetrahedra and are shared in the plane while the fourth atom, at the apex of the tetrahedron is shared with the tetrahedron of the lower layer. The STEM measurements could also reveal the presence of the dark corners of the hexagons comprising silicon atoms (Figure 1.12

---

(c). C. Büchner *et al.* [14] reported that the STM image ( $5 \text{ nm} \times 5 \text{ nm}$ ) taken from the surface comprises hexagonal rings, exclusively (Figure 1.12 (d)). The bonding nature of the bilayer have been verified by the photoelectron (XPS) and infrared absorption spectroscopies (IRAS). A  $\text{Si}^{+4}$  oxidation state has been attributed to the presence of the core level shift at 102.5 eV in the XPS studies, shown in Figure 1.12(e). The oxygen 1s spectra shows a feature at 531.7 eV corresponding to Si-O-Si bond along with a very low intensity feature at 529.9 eV corresponding to O-metal species. The high ratio between the two oxygen related features of 12:1 indicates that the majority of oxygen is bound to Si atoms. This confirms the tetrahedral bonding nature of the silicon in the lattice, within the  $[\text{SiO}_4]$  tetrahedra. These tetrahedra have a characteristic bonding. The O-Si-O bonds form a  $140.3^\circ$  angle, with a Si-O bond length of 0.162 nm. Such bonding character has been earlier shown to exist in bulk silicon oxide, where silicon is tetrahedrally bonded. The typical bond vibrations detected in infrared-absorption spectroscopy (IRAS) further support the bonding characteristic in the bilayer silicon oxide. The in-phase combination of the asymmetric stretching vibration of the Si-O-Si bonds between the two layers, perpendicular to the surface, is recorded at  $1302 \text{ cm}^{-1}$ . These arise from straight Si-O-Si bonds, *i.e.* forming a  $180^\circ$  angles. The spectrum also features vibrations resulting from the combination of the symmetric stretching of Si-O-Si bonds parallel to the surface at  $642 \text{ cm}^{-1}$ . The experimentally obtained vibrational spectrum, shown in dark grey, is interpreted with the help of DFT simulated bond vibrations, shown in light grey, in Figure 1.12f. The DFT calculations with the above derived parameters postulate the relaxed structures shown in Figure 1.12 (g,h).

A single layer of tetrahedra of the bilayer can also be stabilised on supports. This two-dimensional phase, half the thickness of the bilayer phase is called monolayer silicon oxide. Mo(112) [90] [89] [51] and Ru(0001) [121] [119] [125] are the two widely studied substrates for monolayer stabilisation. As observed for the bilayer phase, the monolayer silicon oxide possess a hexagonal lattice made of  $[\text{SiO}_4]$  tetrahedra. The sharp LEED and the STM microscopy performed on the monolayer silicon oxide provide information similar to the bilayer phase (Figure 1.13 (a-c)). The Ru(0001) has a flat hexagonal

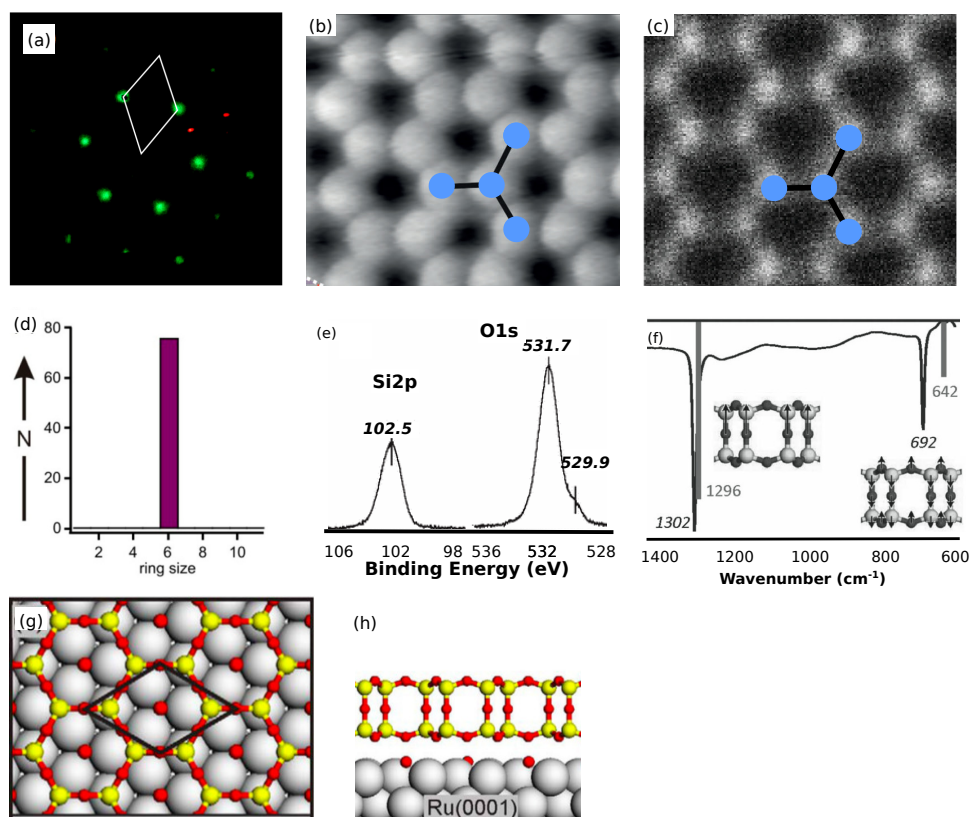


Figure 1.12: Studies performed to determine the structure of bilayer silicon oxide. (a) Sharp LEED pattern demonstrating the 3-fold symmetry and crystallinity of the film. (b) STM micrograph showing the positions of the silicon atoms (blue balls), taken over  $1.9 \text{ nm} \times 1.6 \text{ nm}$  at 3 V and 100 pA. (c) High Angle-ADF measurements taken over bilayer silicon oxide. (d) The crystalline bilayer silicon oxide film consists of hexagonal rings only. This can be seen in the histogram of the ring sizes derived from analysis of an area of  $5 \text{ nm} \times 5 \text{ nm}$ . (e) XPS intensity as a function of binding energy at the vicinities of Si 2p and O 1s core levels. (f) IRAS spectrum as a function of photon wavenumber revealing symmetric and asymmetric vibration modes. DFT relaxed model developed based on the experimental evidences is shown in (g) as top-view and (h) as cross-section. Adapted from [66] [14] [42] [93].

---

surface while Mo(112) has a row-trough surface. This difference in the structure of the substrate induces different aspects in the structure of the monolayer silicon oxide. STM imaging performed on monolayer silicon oxide on Mo(112) shows the hexagons to be shrunk in one direction due to the rectangular lattice of the substrate, while regular hexagons are obtained on the Ru(0001) surface.

XPS studies reveal that the Si  $2p$  region only exhibits a single peak with a binding energy of 103.2 eV, which is typical for a  $\text{Si}^{4+}$  oxidation state. The O  $1s$  peak shows two components centred at 531.3 eV and 529.8 eV which suggests the presence of two oxygen species in different environments. The major peak at 531.2 eV correspond to the oxygen coordinated with two silicon atoms, Si-O-Si bonds and the shoulder peak at 532.5 eV corresponds to oxygen binding to metal support. The ratio between the two kinds of oxygen atoms increases to 3:2 for monolayer, in comparison to 12:1 for bilayer. This confirms the increase in the amount of oxygen bonded to the metal support in case of the monolayer, possibly via Si-O-metal bonds [121].

Infrared-absorption vibrational spectroscopy (IRAS) brings further information on the structure by revealing vibrations of bonds with net dipole moment perpendicular and parallel to the surface. The vibrational modes at  $1059\text{ cm}^{-1}$  correspond to the asymmetric stretching of Si-O species pointing towards the Mo surface. This is in indication for a bonding between the monolayer and the support. The band at  $790\text{ cm}^{-1}$  corresponds to vibration modes with net dipole moment normal to the surface, Si-O-Si symmetric stretching coupled with Si-O-Si bending and the band at  $687\text{ cm}^{-1}$  correspond to vibration modes involving coupled Si-O-Si bending. Altogether these modes are consistent with the proposed model for the monolayer [113]. The DFT calculations performed to simulate the IRAS spectra are shown embedded in Figure 1.13 (f). The DFT calculated spectra replicates the experimentally observed features. It is important to note that the simulated spectra, both IRAS and XPS, mismatch with the experimental data due to small limitations in terms of taking the interaction with the substrate into account.

The monolayer silicon oxide observed with TEM in cross-sectional mode reveals bonding between the monolayer and the support [7], as shown in Figure 1.13 (d). The assessed height value of  $3.4\text{ \AA}$

---

corresponds to metal–O–Si bond length. The bottom oxygen bonds, between the silicon and the metal support were well resolved and characterised with electron energy loss spectroscopy (EELS).

### **Silicon oxide on SiC**

The two-dimensional phases of silicon oxide on the 4H- and 6H- SiC have been studied via LEED and Auger spectroscopy. A typical Auger spectra consisting of Si<sub>L<sub>VV</sub></sub> and C<sub>K<sub>LL</sub></sub> peaks corresponding to the SiC surfaces was observed to contain an extra feature related to O<sub>K<sub>LL</sub></sub> peak. On the (000 $\bar{1}$ ) surface (C-face), a feature at 65 eV was found which was attributed to oxygen bonded silicon atoms. The LEED pattern, shown in Figure 1.14, reveals a surface reconstruction, with a surface unit cell rotated by 30° with respect to the substrate surface unit cell. The quantitative analysis on the structure of the surface reconstruction is consistent with a honeycomb lattice containing two silicon atoms per unit cell. A model with oxygen atom connecting neighbouring silicon atoms allowing for completing the ring was proposed. On the carbon face, the Si atoms bind directly to the C atoms of the topmost SiC bilayer in the surface normal direction. This configuration can be expected as the Si – C bond is favourable over C – O due to electronegativity considerations. In contrast, on the Si face, the Si atoms from the monolayer bind to the Si atoms of the topmost SiC layer via oxygen bonds. This Si-O-Si perpendicular bonds are similar to the ones observed in the monolayer silicon oxide supported by metal substrates [8].

#### **1.3.4 Defects in 2D silicon oxide**

Extensive studies of the atomic structures and the properties of defects in the two-dimensional phases of silicon oxide have been performed. Various kinds of defects have been observed and studied, from point defects to extended defects. They are discussed below.

##### **1. Point defects**

Point defects are formed due to missing or displaced atoms. These defects include vacancies, self- and impurity interstitials

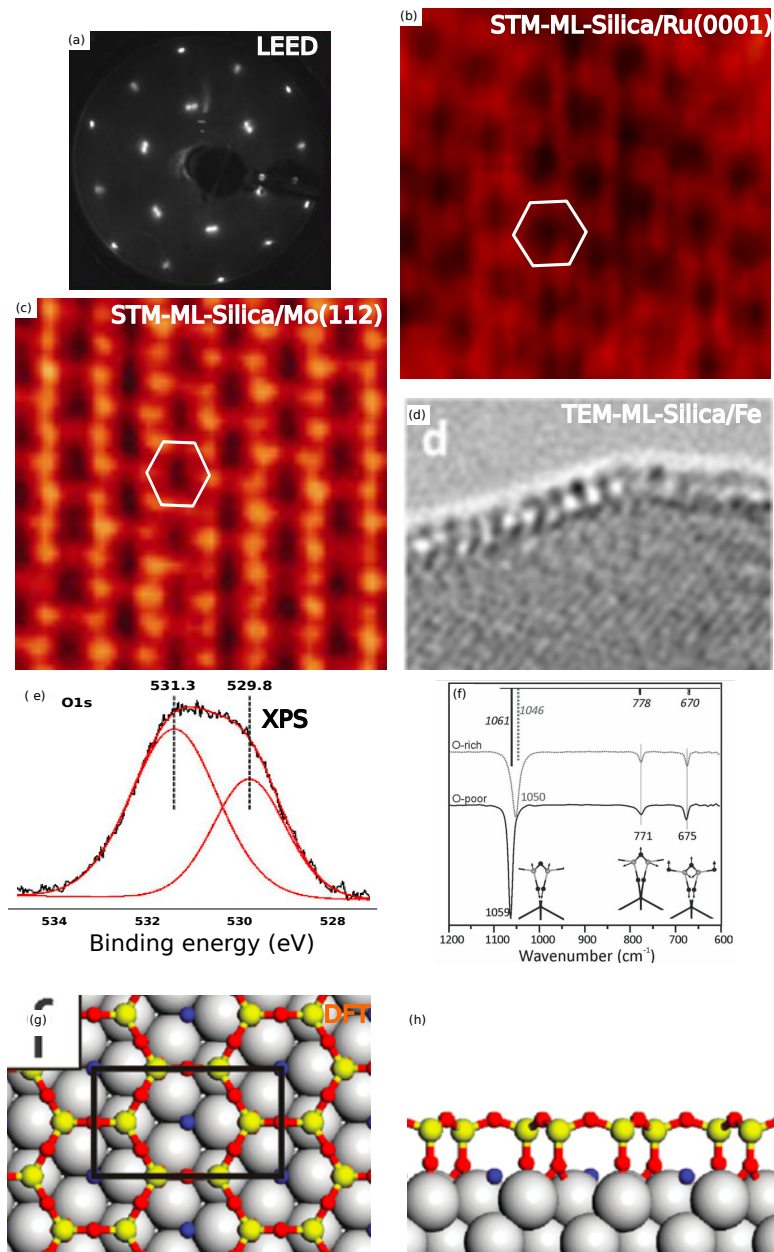


Figure 1.13: Structure of monolayer silicon oxide on metals. (a) LEED; STM on monolayer silicon oxide grown on (b) Ru(0001), (c) Mo(112); (d) Cross-sectional image from TEM; (e) XPS; (f) IRAS with DFT simulations (dark line); (g-h) Top and cross-sectional view of monolayer predicted by DFT on Ru(0001) surface. Adapted from [124] [121] [113][7] [92].

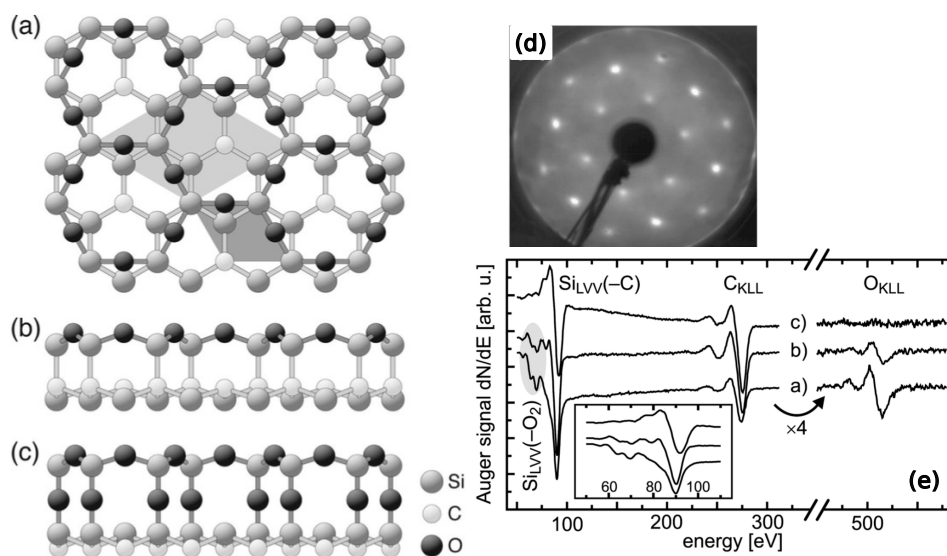


Figure 1.14: (a) ML-Silicon oxide grown on SiC surface. The monolayer depicts a  $R30^\circ$  reconstruction in respect to SiC surface; LEED in (d). Two different phases, one with Si-O-Si on silicon face (b) and Si-O-Si on carbon face (c) on the SiC crystal. (e) Corresponding Auger spectra. Adapted from [8].

and substitutions. Two-dimensional silicon oxide has been experimentally shown to possess many such defects. Simple rotations of the segment of the hexagonal rings by  $90^\circ$  around its mid-point result in transformation of hexagons into two pentagons and two heptagons [42] [10]. These are known as Stone Wales defects [100]. A Stone-Wales (SW) defect observed in the bilayer phase of two-dimensional silicon oxide is shown in Figure 1.15. The construction of such defects does not require any removing or addition of atoms from/to the lattice. In the case of bilayer silicon oxide, four silicon atoms (two in each layer) rotate along with their neighbouring oxygen atoms around the shared oxygen atom. On six successive transformations, a configuration of the bilayer silicon oxide comprising a  $30^\circ$  rotated domain with respect to the surrounding lattice is formed. This rotated domain is separated by pentagons and heptagons arranged in a ring. These kind of defects were observed in graphene, a much simpler system, and have been termed as



*flower defects*. The energy calculations to study the formation of SW defects have shown a special trend in bilayer silicon oxide, shown in the Figure 1.16. The energy of formation of one SW defect in the lattice increases with every rotation till fourth rotation and then decreases from fourth rotation until the flower defect is formed [10]. Each rotation is accompanied by strain field propagating in the surrounding lattice. These strains, in extension are seen in red and in compression as blue, in the insets of Figure 1.16 as deviations in the Si-Si nearest neighbour distances.

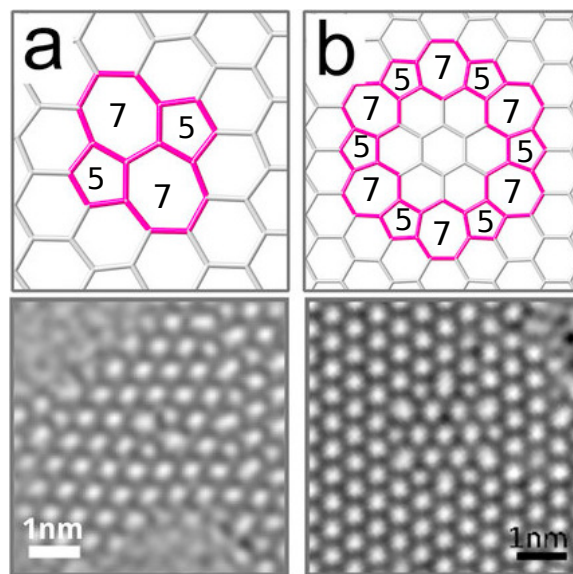


Figure 1.15: Stone Wales defects formed due to one (a) and six (b) transformations are obtained in the DFT calculations (upper panel) and ADF-TEM (lower panel). Adapted from [10].

Missing structural units are vacancies in the lattice. These vacancies can reconstruct and form stable structures, while mono-vacancies can be highly reactive. Di-vacancies have been calculated to be relatively stable. Four different structures of reconstructed di-vacancies have been proposed to be stable by DFT calculations. These structures are presented in the Figure 1.17. Out of these four, only one kind of di-vacancy has been imaged so far (Figure 1.17 (d-e)). This is a 5555-6-7777 structure in the hexagonal lattice, commonly called a butterfly

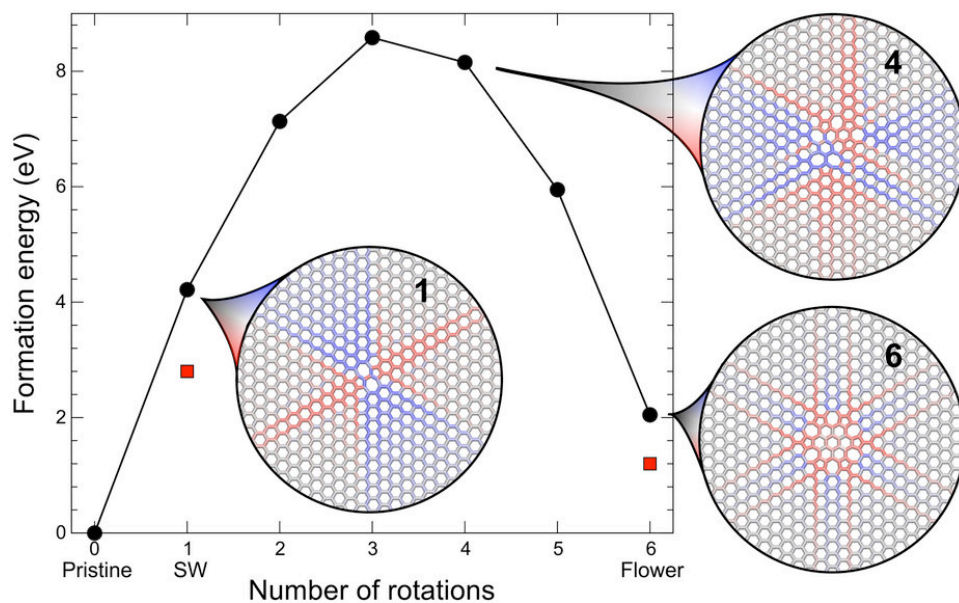


Figure 1.16: The energy calculation for successive rotations in Stone Wales transformation leading to flower defect formation. Adapted from [10].

defect. The formation of such a defect involves removal of two structural motifs along with two bond rotations.

Similarly, extra structural motifs can merge and reconstruct the bilayer silicon oxide lattice leading to formation of non-hexagonal structures in the lattice [10], shown in Figure 1.18 (a,b). At times, the interstitial atoms are found in the lattice [42], as seen in Figure 1.18 that do not reconstruct with the lattice and stay unbound (Figure 1.18(c)). These interstitial atoms are marked in purple arrow in the figure.

In the case of monolayer silicon oxide, the irradiation by the electron beam has been observed to yield defects. Non-hexagonal rings in monolayer silicon oxide have been shown to form upon annealing to 450°C by F. B. Romdhane *et al.* Polygons with 4 to 9 segments have been formed. The morphology of these defects change under electron beam irradiation [7]. The pair of octagons separated by a square readily transforms into pairs of octagons and pentagons via intermediate heptagons and pentagons. This transformation has been recorded with a TEM microscope, as

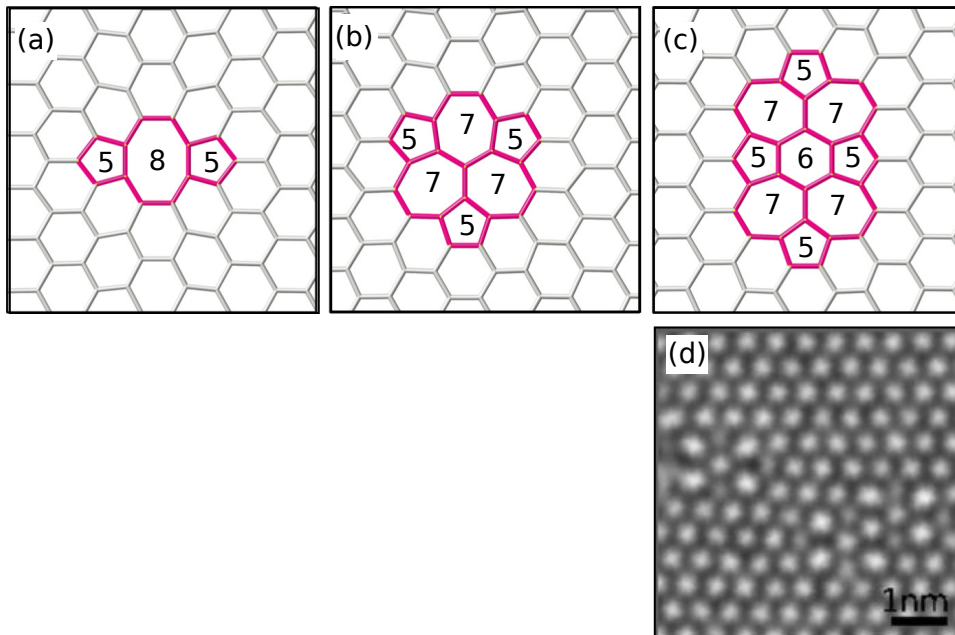


Figure 1.17: Structure of the saturated di-vacancies in the bilayer silicon oxide lattice, (a) 55-8, (b) 777-555, (c) 7777-6-5555. (d) The 5555-6-7777 structure has been observed in the ADF-TEM. The merger of two divacancies can also be seen.

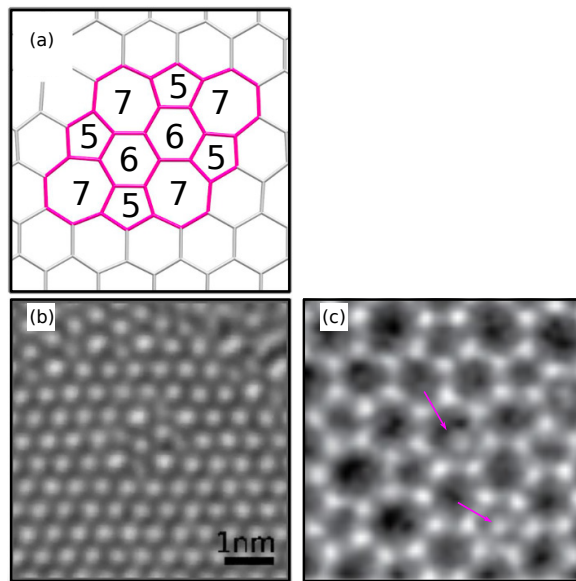


Figure 1.18: Interstitials, in form of structural motif can lead to reconstruction of the local lattice and lead to the formation of defects like 5555-66-7777 (a,b). (c) Single atoms as interstitials might appear in the centre of the rings distorting the lattice. Adapted from [10] [42].

---

shown in Figure 1.19.

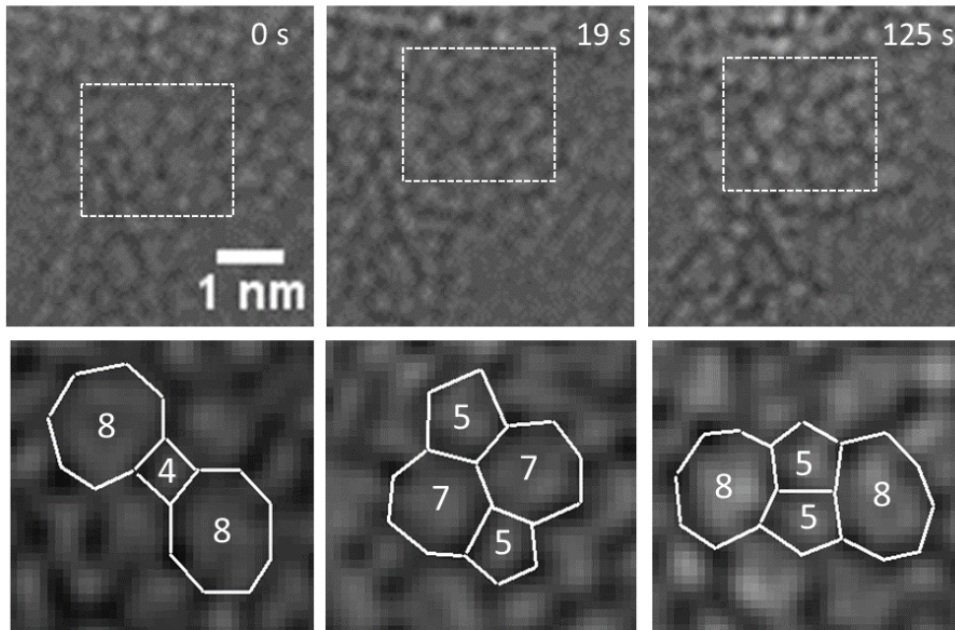


Figure 1.19: Transformation of defects under electron beam irradiation during 125 seconds (upon annealing). The zoom-in of the defects is present in the lower panel. Adapted from [7].

Bing Yang *et al.* have reported a formation of defects on monolayer silicon oxide via vacuum annealing [119]. From LEED studies it was evident that the monolayer rotated by  $30^\circ$  and the lattice constant contracted to  $5.2 \text{ \AA}$ . This new phase of monolayer silicon oxide was observed to be stabilised via formation of a 2D array of defects with 3-fold and 4-fold symmetries. The defects with a hexagon surrounded by three pentagons and three heptagons show a triangular structure and thus have been named as T-defects. Owing to the 3-fold symmetry, T-defects get readily embedded into the hexagonal lattice. They have a structural resemblance to the blister defects predicted for graphene. Another kind of defect comprising an octagon surrounded by two squares, two pentagons and four heptagons was also observed in the vicinity of T-defects. Due to their rectangular shape, they are termed as R-defects. These two defects form arrays in the hexagonal lattice. T- and R- defects also form isomorphs rotated

by  $60^\circ$  (as shown in Figure 1.20 (b-e)). These defects are capable of hosting functional groups like  $\text{OH}^-$  upon reaction with ice that can readily be involved in sensing activities [120].

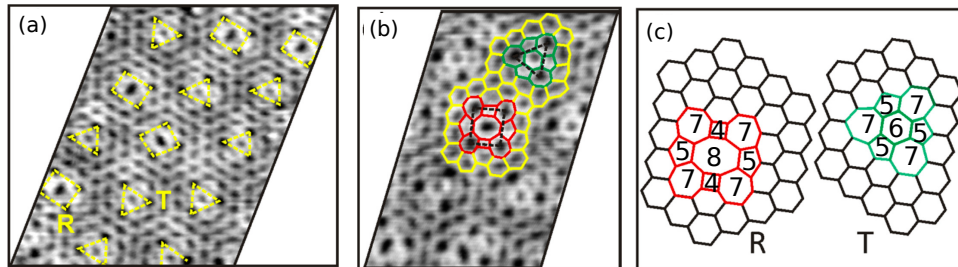


Figure 1.20: (a) An array of T- and R- defects on monolayer silicon oxide grown on Ru(0001) forms on subjecting the monolayer to vacuum annealing. (b) The T- and R- defects are found in vicinity of each other. (c) R- (left) and T- (right) defect structure. Adapted from [119].

### ***Inverse SW defect***

A reverse transformation of a SW defect [41] into hexagonal lattice observed under stimulation by an 80 keV electron beam in an aberration-corrected TEM is shown in Figure 1.21. By tracking the projected positions of the Si atoms, intermediate structures formed during the transformation could be imaged, although with a limited resolution [86]. The kinetic energy thresholds for sputtering out atoms are 16.8 eV and 11.6 eV for silicon and oxygen respectively [10]. These values imply that oxygen atoms are easy to displace under the electron beam irradiation. The displacement occurs in response to strain fields developing in the bilayer silicon oxide, discussed shortly in section 1.3.5.

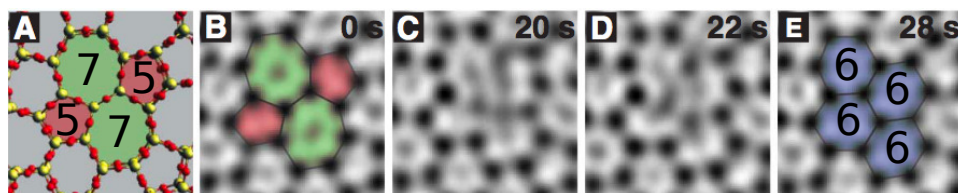


Figure 1.21: Reverse transformation of Stone-Wales defect in bilayer silicon oxide under electron beam irradiation. Adapted from [41].



---

## 2. **Domains and boundaries (1D-defects)**

One-dimensional line defects form network on the two-dimensional phases of silicon oxide [113] [121] [124]. AC-HRTEM and STM have shown their abundance resulting in a mosaic structure containing domains and domain boundaries (Figure 1.22). The domain boundaries are found to be highly directional in both the two phases. In bilayer silicon oxide, multiple kinds of domain boundaries form. The boundaries comprising SW defects, *i.e.* pentagons and heptagons, facilitate the formation of domains rotated by  $30^\circ$ , like also often observed in graphene [20]. An atomically resolved ADF-TEM [10] picture of this boundary is shown in Figure 1.22(a).

Domain boundaries stitching together the atomic lattices with same crystallographic orientations on both the sides are also observed. Such domains are termed as *anti-phase domains* (APDs). In a description along which a phase value would vary between 0 and  $2\pi$ , respectively for two superimposed lattices and for two lattices laterally shifted by one lattice parameter, the anti-phase term refers to a  $\pi$ -phase. They are separated by anti-phase domain boundaries (APDBs). Such domains have been found previously in other two-dimensional materials. The formation of an APDB in the direction parallel to the zig-zag direction of the bi-layer silicon oxide/Ru(0001) [13] comprising octagon-pentagon-pentagon is shown in Figure 1.22 (b).

The APDB in the bilayer phase of silicon oxide form on substrates like Pd(100) also. E. Altman *et al.* have shown that the APDs mutually misalign in the  $[1\bar{1}0]$  direction [2]. The dotted rectangle in Figure 1.23 (a, b) connects the hexagons on the two sides of the APDB. The APDB comprises stretched pores created by octagons (as shown in Figure 1.23 (b)). The octagons are formed by insertion of rotated  $[\text{SiO}_4]$  tetrahedra into the six membered rings. These extra tetrahedra allow connections to the neighbouring tetrahedra in the two domains. The two extra oxygen atoms involved in addition of the tetrahedra bind to the similar tetrahedra in the lower (or upper) layer of the bilayer structure; thus passivating the system, as shown in

cross-section in Figure 1.23.

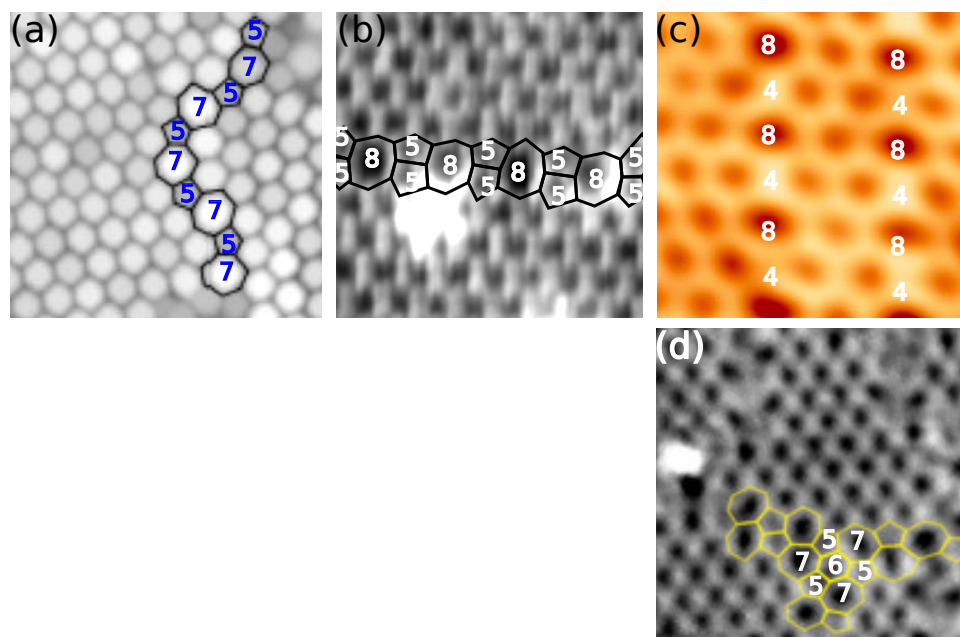


Figure 1.22: (a) The twin boundary, 57, stitching together 30° rotated domains in bilayer silicon oxide. (b) Antiphase domain boundary, 855, parallel to zigzag direction of bilayer on Ru(0001), (c) 84-, Anti phase domain boundary, on monolayer on Mo(112). (d) Three 57 anti phase domain boundaries merging on monolayer on Ru(0001), forming a blister defect. Adapted from [10] [13] [107] [119].

A model of APDB in monolayer silicon oxide grown on row-and-trough surface of Mo(112) has been provided by Todorova *et al.* The model consists in cutting the monolayer in the  $[\bar{1}10]$  direction. Then one-half of the lattice is translated by half the unit cell in the  $[\bar{1}\bar{1}1]$  direction towards the other half [107]. This results in formation of 84- polygons, seen in the STM image in Figure 1.22 (c).

The monolayer silicon oxide films grown on Ru(0001) form 1D defects (APDBs) comprising in pair of pentagons and heptagons, 5577, in the armchair direction. On the merger of these APDBs, formation of a blister defect comprising a hexagon surrounded by three pentagons and three heptagons (predicted for graphene) has been shown by B. Yang *et al.* Figure 1.22 (d).



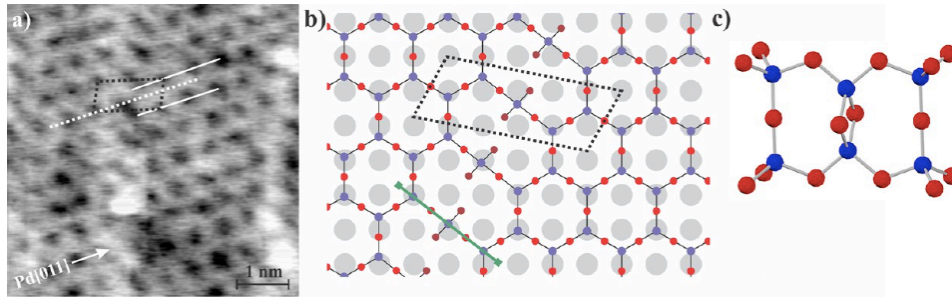


Figure 1.23: Anti phase domain boundary in bilayer silicon oxide on Pd(100) formed by excess of  $[\text{SiO}_4]$  tetrahedra, (a) STM image, (b) ball model of bilayer silica on Pd(100) and (c) cross-sectional model of boundary. Adapted from [2].

### 3. 2D defect network

The thin films of silicon oxide are amorphous in nature, *i.e.* they lack any order on the surface. In 1932, Zachariasen postulated a continuous random network of corner-sharing  $[\text{SiO}_4]$  tetrahedra as the structure of the vitreous 2D glass [127]. This structure has been observed in the STM and TEM experiments on bi-layer silicon oxide alongside the crystalline phase [42] [63]. Interestingly, the amorphous phase is also stoichiometric  $\text{SiO}_2$ . The LEED pattern shows a diffusive ring instead of sharp spots expected from a crystalline surface. The atomic structure in the amorphous silicon oxide is random in the  $xy$ -plane, but the bilayer maintains a well-defined structure in the  $z$ -direction. The Si-O-Si bond between the two tetrahedra layers maintain a the  $180^\circ$  angle. This renders a flat surface appropriate for scanning probe microscopy.

The STM image shows the bright protrusion at the position of oxygen atoms, overlaid with red balls in the STM image (Figure 1.24). Based on the lattice formed by oxygen atoms, the location of the silicon atoms could be extrapolated. The number of silicon atoms involved in forming the rings varies from four to nine in amorphous silicon oxide. The ring size distribution has been studied in STM and TEM images (as shown in Figure 1.24 (a,b)). The majority of the rings are found to consist of six silicon

atoms, while the ring segments range from four to nine over the bilayer film (as shown in Figure 1.24 (d)). The distribution of the ring size is also found to be highly asymmetric. The ring distribution is found to be governed by the bond angles inside the tetrahedron and the bonds between different tetrahedra. HR-EELS measurements, shown in Figure 1.24 (e-f) for silicon and oxygen, corroborated with ADF imaging in Figure 1.24 (g) support the picture of a random arrangement of the polygonal rings. A symmetric distribution of the internal tetrahedron angle of O-Si-O around  $110^\circ$  with a standard deviation of  $10^\circ$  matches fairly well with the regular tetrahedron angle of  $109.5^\circ$ . The average Si-O-Si, *i.e.* the inter-tetrahedra angles, is found to be around  $144^\circ$ . This is in agreement with the bond angles resolved from NMR and XRD on bulk vitreous silica [63] [63] [64] [14].

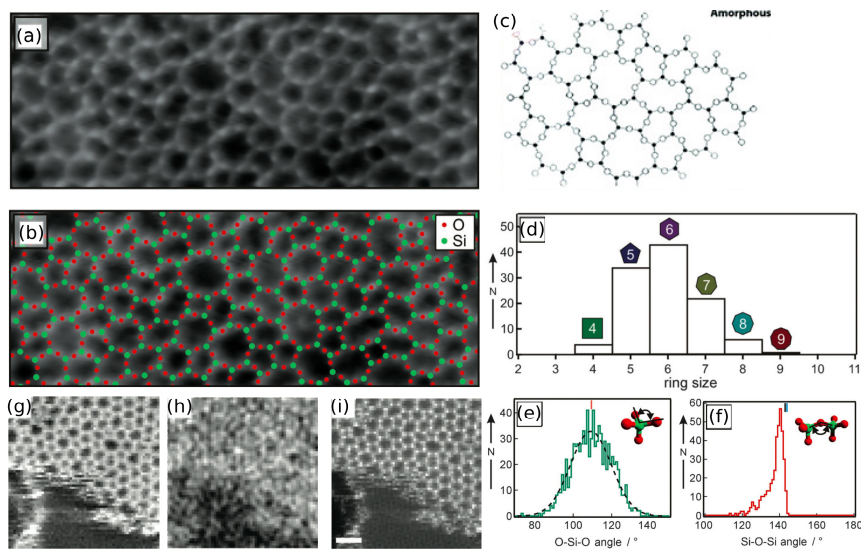


Figure 1.24: Random network of silica rings. (a) STM image ( $8 \text{ nm} \times 3 \text{ nm}$ ) at 100 mV and 100 pA. (b) Ball model overlaid image of (a). (c) Random network model predicted by Zachariassen. (d) Ring size distribution, (e) O-Si-O bond angle distribution and (f) Si-O-Si bond angle distribution in (a). (g-h) HREELS maps of silicon and oxygen and (i) ADF image of the amorphous silicon oxide in the same region. Adapted from [64] [42].

---

The coexistence of the crystalline and amorphous regions in the bi-layer silicon oxide has provided access to the atomic arrangement of the interface by STM [64] [121] and TEM [42] independently, shown in Figure 1.25. A 1.6 nm smooth and stoichiometric transition interfaces the crystalline and amorphous regions. The statistical studies provide information regarding the Si-Si nearest neighbour distances. The Si-Si nearest neighbour distances remain constant in the crystalline, amorphous and the interface regions: disorder is mainly accounted by bond bending shown in Figure 1.25 (c).

### 1.3.5 Epitaxy of two-dimensional silicon oxide

The diffraction studies have provided information about the crystallinity and commensurability of the hetero-epitaxial films of two-dimensional silicon oxide with respect to the metal supports. One unit cell of the two-dimensional silicon oxide corresponds to four lattice cells (two in each direction) of the metal support, Mo(112) and Ru(0001), commonly used. The diffraction also indicates a cellular arrangement of silicon oxide with the support metals. The hexagons are aligned in the  $[10\bar{1}0]$  direction of the (0001) surfaces of Ru and Co [7] [86], and  $[011]$  direction of surfaces with rectangular lattice, like Mo and Pd [88] [2]. The lattice constant is found to be  $5.4 \text{ \AA}$  for monolayer; and from  $5.3 \text{ \AA}$  to  $5.5 \text{ \AA}$  for and bilayer silicon oxide on graphene, Ru, Pt and Pd by different approaches. This indicates, roughly, 4% epitaxial strain in the sheet on metals, in comparison to free-standing layers.

The bilayer silicon oxide maintains minimal interaction with the substrate via van der Waals forces. F. Ben Romdhane *et al.* report a configuration where the bilayer adsorbs over the bridge sites with the binding energy of the bilayer to Ru(0001) and Co(0001) supports to be roughly  $-89 \text{ meV/Si atom}$  (or  $-14 \text{ meV/\AA}$ ) and  $-62 \text{ meV/Si atom}$  (or  $-11.4 \text{ meV/\AA}^2$ ), respectively. These binding energies are within the range of the binding energy in layered materials. The sliding of the bilayer to other sites shows a fluctuation in energy of about  $10 \text{ meV}$ . In contrast, D. Loffler *et al.* employing DFT calculations (with dispersion corrections) showed that the bilayer is adsorbed on

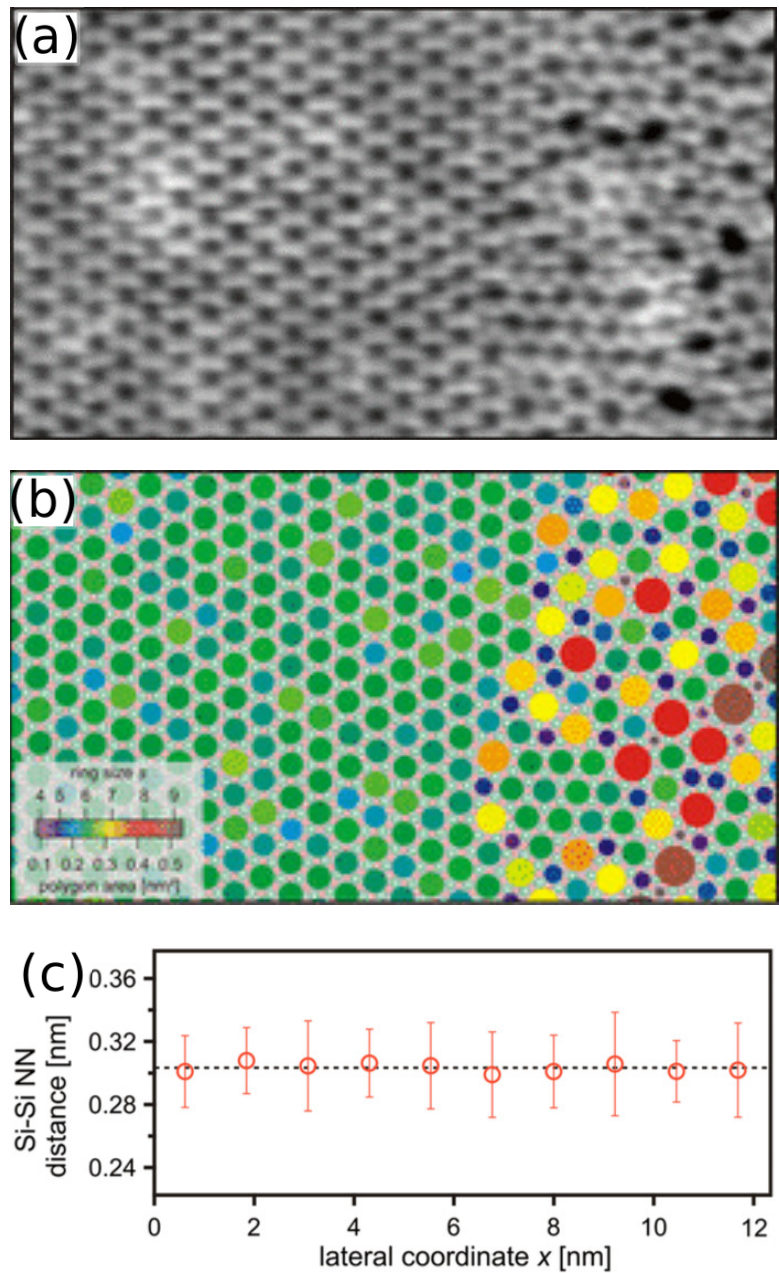


Figure 1.25: The interface between the crystalline and the amorphous regions in bilayer silicon oxide as atomically resolved by STM (a). The interface, in (b), is found to be as small as 1.6 nm. The Si-Si nearest neighbour distance remains constant throughout the STM micrograph, in crystalline and amorphous regions, (c). Adapted from [63].

---

Ru(0001) into the hcp-hollow sites with bridging oxygen atoms of the lower layer always on top of Ru atoms. The binding energy of this configuration is  $-32 \text{ meV}/\text{\AA}^2$ . The bilayers are held  $2 \text{ \AA}$  above the metal surface. This gives opportunity to store atoms at the interface between the bilayer and metal support. The oxygen atoms adsorb as a reminiscent of the growth protocol used, often. The amount of oxygen adsorbed on the substrate is known to change the most stable adsorption configuration of the bilayer. With one spare oxygen atom occupying the hcp-hollow site on the Ru(0001), the corners of the bilayer hexagons adsorb in the fcc-hollow and top sites. In this configuration, the binding energy has been shown to reduce to  $-24.6 \text{ meV}/\text{\AA}^2$ . At maximum, the four hcp-hollow sites available on the Ru(0001) surface under the bilayer can be reconstructed as  $3\text{O}-(2 \times 2)$ . The XPS spectra show a shoulder peak at 529 eV corresponding to this oxygen reconstruction on Ru(0001) under the bilayer silicon oxide [66].

With 4% strain, the monolayer silicon oxide covalently binds to the (0001) surfaces in fcc-hollow and top- sites with a binding energy of  $-3 \text{ eV}$  per Si atom via Si-O-metal bonds [7]. In a different configuration, discussed in Chapter-3, the monolayer is found to be less stable by roughly  $75 \text{ meV}$  and  $210 \text{ meV}$  per Si atom on Ru(0001) and Co(0001) respectively. Similar to the bilayer phase, possible adsorption of a single oxygen atom in the hcp-hollow site inside the monolayer silicon oxide hexagons has been proposed. The core level shifts for oxygen bridging between the Si-metal surface and oxygen bonded on metal are very close in DFT-simulated XPS spectra, shown in Figure 1.26. Due to the extremely small difference in the core level shifts, resolving them experimentally is difficult. The DFT calculations indicate lower ground state energy by  $< 0.1\%$  on bonding of extra oxygen atom, resulting in marginally stabilising the system. Based on such thermodynamics argument the presence of this oxygen atom remains ambiguous [121]. The curious case of this extra oxygen atom will be addressed during the course of this thesis.

Strain in the two-dimensional phase of silicon oxide has been studied via energy calculations. There are two kinds of strains on the monolayer and bilayer silicon oxide on different substrates. The (0001) surfaces, for instance Ru and Co, exert a biaxial strain along both

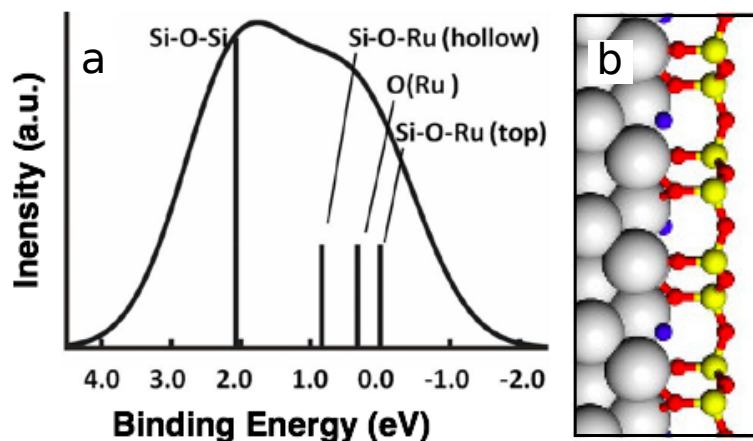


Figure 1.26: (a) XPS spectra calculated by DFT suggesting Si-O-Si, Si-O-Ru(hollow), Si-O-Ru(top) and O-Ru bonds. (b) Side-view of the relaxed monolayer silicon oxide on Ru(0001) calculated via DFT simulations. Adapted from [121].

the primitive lattice vectors that maintains the hexagonal symmetry of the monolayer and bilayer silicon oxide. On the contrary, the (100) surfaces, or the square/rectangular lattices of Mo and Pd, lead to a uniaxial strain. The study on the biaxial strain is provided in Figure 1.27, showing in black and red curves the case of free-standing bilayer and monolayer phases. The curves are asymmetric. The layers appear to be softer on compression, *i.e.* negative strain. This asymmetry arises from the possibility of the lattice to undergo a structural change via rotation of  $[\text{SiO}_4]$ , seen as left-top inset in the Figure 1.27 to maintain the Si-O bond lengths. Expansion leaves no possibility for such rotations and the bond length increases. This increase in bond length costs more energy, thus the strain energy increases.

On the other hand, uniaxial strain is capable of making the film commensurate in one direction while in the other direction the lattice relaxes naturally. A comparative study on the uniaxial (black) and biaxial (red) strain in a bilayer silicon oxide film is shown in Figure 1.28 (b).

The plot in Figure 1.28 (c), between the corresponding strain in the armchair direction (black; marked "a") and the z-direction



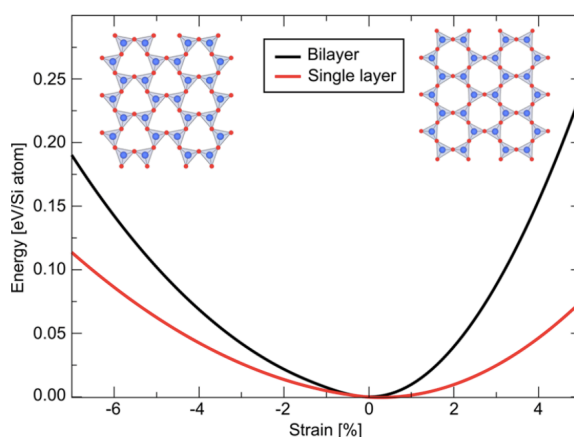


Figure 1.27: Energy-strain curve for monolayer and bilayer silicon oxide. Adapted from [7].

(blue; perpendicular to the surface) is shown. The strain in the "a" direction shows a steep change while the "z" direction remains constant. This implicates that the relaxation occurs uniquely within the plane and not out-of-plane. The bond lengths of all the Si–O bonds is observed to change by less than 1%, Figure 1.28 (e). Actually, most the deformation is occurring via rotations of the tetrahedra, by as much as  $5^\circ$ .

### Relationship between the substrate and oxygen

Xin Yu *et al.* suggested that the heat of dissociative adsorption of oxygen on metals controls the atomic structure of the ultra thin film and the number of layers [125] [124]. Metals, like Mo, with low heat of dissociative adsorption of  $-544$  kJ/mol (and heat of formation for  $MoO_2$  of  $-588$  kJ/mol) only allow the formation of monolayer silicon oxide, selectively; on the contrary Pt, a noble metal, with high heat of dissociative adsorption of oxygen,  $-133$  kJ/mol (and heat of formation for  $PtO_2$  of  $-71$  kJ/mol), forms weak oxide bonds and results in formation of bilayer silicon oxide, exclusively, irrespective of the amount of silicon available, as confirmed by IR-absorption spectra and adjoining along with STM image showing interconnected amorphous bilayer patches. This trend continues to Ru which has an intermediate heat of dissociative adsorption of oxygen of  $-220$  kJ/mol

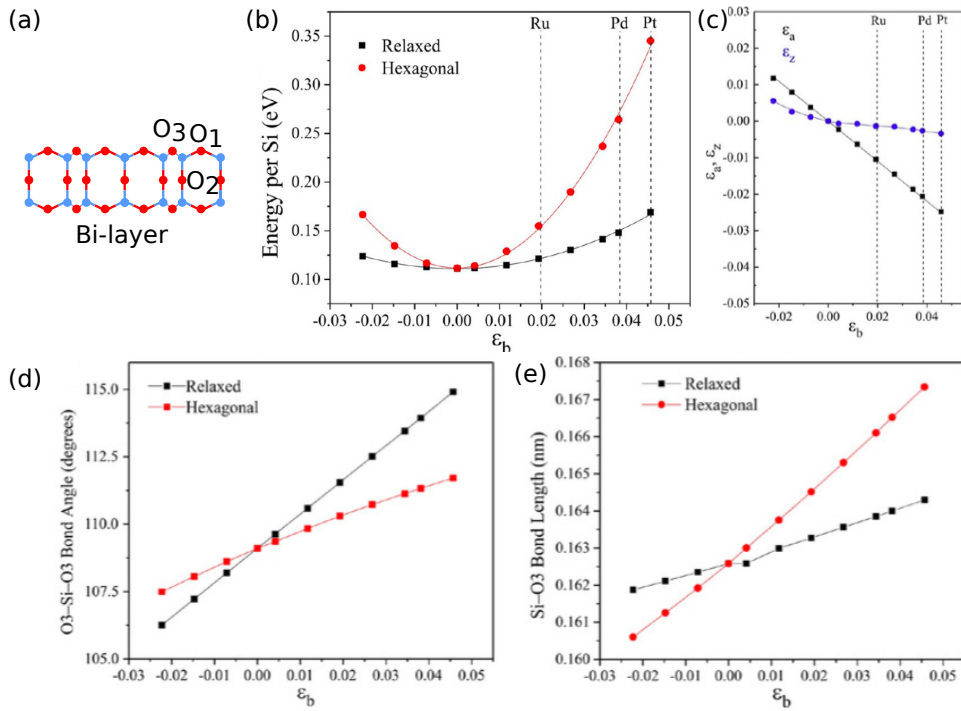


Figure 1.28: (a) Cross-sectional view of bilayer silicon oxide marked with different oxygen atoms considered in calculating strains. (b) Plot between the bonding energy and the uniaxial (black) and biaxial (red) strain on the bilayer. (c) Plot between the relaxed strain in "a" direction and "z" direction and uniaxial (black) and biaxial (red) strain applied. (d) O-Si-O bond angle as a function of uniaxial (black) and biaxial (red) strain is plotted. (e) Si-O bond length versus the uniaxial (black) and biaxial (red) strain is plotted. Adapted from [2].



---

(and heat of formation for  $RuO_2$  of -153 kJ/mol) and supports growth of both monolayer and bilayer silicon oxide. On Ru(0001), in contrast to Pt(111), the amount of silicon available has been shown to control the number of the layers, single or double. The accidental growth of, solely, bilayer silicon oxide on top of graphene which represents a weakly interacting and oxygen resistant system seems a fitting corroboration.

### 1.3.6 Growth of two-dimensional silicon oxide

Multiple growth techniques and mechanisms have been reported in the literature regarding the growth of two-dimensional silicon oxide, employing very different recipes.

#### Reactive deposition

As mentioned earlier, reactive deposition is a commonly used technique to grow oxides. It has been applied to grow the two dimensional phase of silicon oxide as well. In this technique, the clean surface of the metal crystal is exposed to a silicon flux from an electron beam evaporator (or thermal annealing of a piece of silicon wafer) in presence of oxygen. Todorova *et al.* have reported a growth of the monolayer silicon oxide on a Mo(112) via Si evaporation under an exposure of the surface to  $5 \times 10^{-8}$  mbar of oxygen at 900 K for 5 minutes. Subsequently, depositing Si at 0.07 monolayer per minute under same pressure and temperature and annealing at 1250 K resulted in  $c(2 \times 2)$  reconstructed surface. The IRAS and XPS revealed the presence of the monolayer silicon oxide [107].

In Figure 1.29, the temperature dependence on the growth of the monolayer on Ru(0001) surface is shown, with 0.7 ML silicon deposition under  $2.5 \times 10^{-8}$  mbar oxygen at temperatures ranging between 670 K and 1120 K. With the increase in the temperature, the nucleation density is observed to decrease (Figure 1.29 (f)). While the island size is small and below the resolution (of 15 nm) at 670 K, it grows larger at higher temperatures. The size of the islands is observed to saturate at the temperature of 1120 K indicating desorption or a 3D growth. At high temperatures it is evident that

---

growth occurs at the step edges, and is more fractal [52].

### **Post oxidation**

The post-oxidation technique for the growth of two-dimensional silicon oxide includes a stringent recipe. It comprises in the following steps:

- Starting from a clean Ru(0001) surface (Figure 1.30 (a,e)), a  $(2 \times 2)$ -3O layer is formed by exposing the Ru(0001) surface to  $1 \times 10^{-6}$  mbar of oxygen at 1170 K for 10 minutes. This reconstruction is seen in the LEED pattern in Figure 1.30 (f)
- Si is deposited at room temperature and low oxygen pressures resulting in a rough surface, seen in Figure 1.30(c,g)
- Final post-oxidation under  $10^{-6}$  mbar oxygen at 1045 K for 10 minutes and cool down at 1 K/sec. The oxygen back pressure is reduced at 470 K (Figure 1.30(d,h)).

The growth of the monolayer silicon oxide, upon deposition of 1 monolayer equivalent (MLE) of silicon, in the post deposition technique has been well established for Mo(112) and Ru(0001). Modulating the silicon dose, from 1 MLE up to 2 MLE, directly on an oxygen pre-covered Ru(0001) surface or 1MLE extra on top of monolayer silicon oxide has been shown to yield bilayer phases. On depositing 1.5 MLE silicon, patches of bilayer silicon oxide coexisting with monolayer silicon oxide are seen in the STM images [121]. The LEED patterns from this surface show  $(2 \times 2)$  superstructure spots along with a diffusive ring. This diffusive ring emerges from the vitreous component in the bilayer silicon oxide (Figure 1.31). On increasing the silicon dose to 2 MLE, the complete monolayer converting into bilayer silicon oxide phase was observed by B. Yang *et al.* The temperature during post-oxidation has remained critical in determining the quality of these bilayer films, as shown in Figure 1.32. At temperatures of 995 K and 1045 K, the film is completely closed including at the step-edges. On increasing the temperature to 1270 K the bilayer is strongly de-wetted, as seen as wide dark areas near the step-edges appear. This de-wetting has been rationalised as a

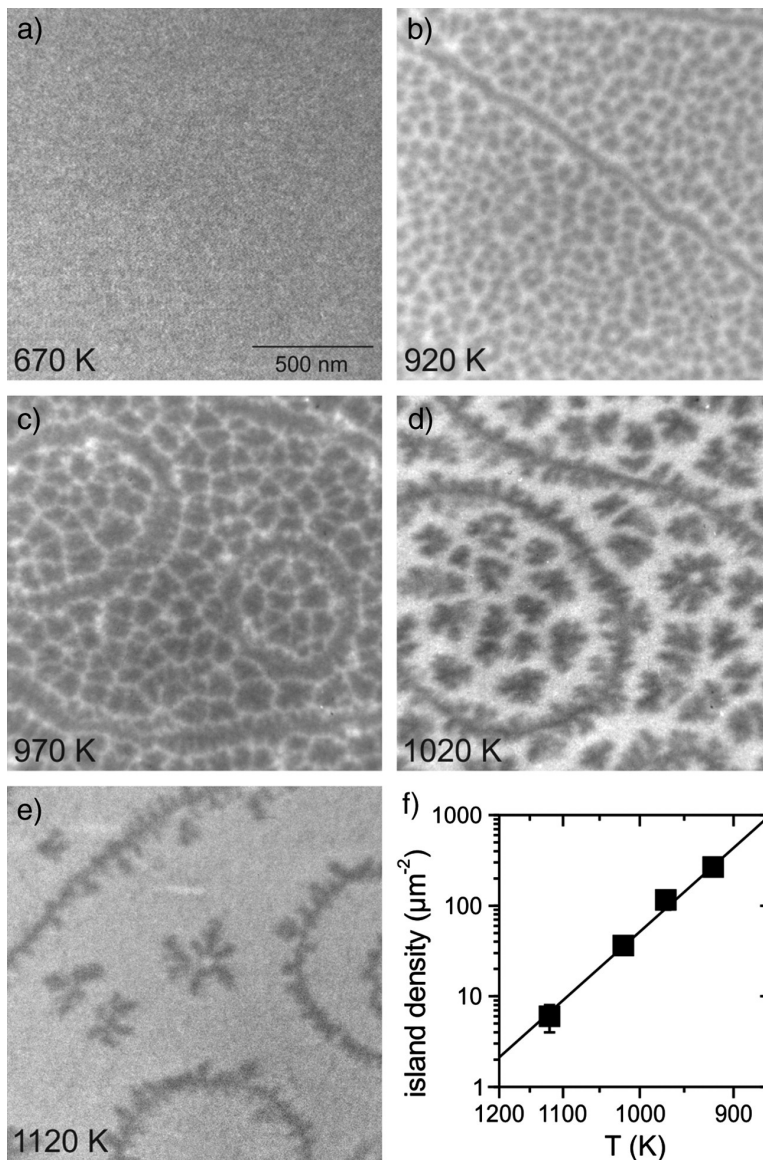


Figure 1.29: LEEM study on the growth of monolayer silicon oxide by reactive deposition as a function of temperature. The nucleation density is shown to decrease on increasing the temperature of silicon deposition from (a-e). (f) Decrease in nucleation density against temperature. Adapted from [52].

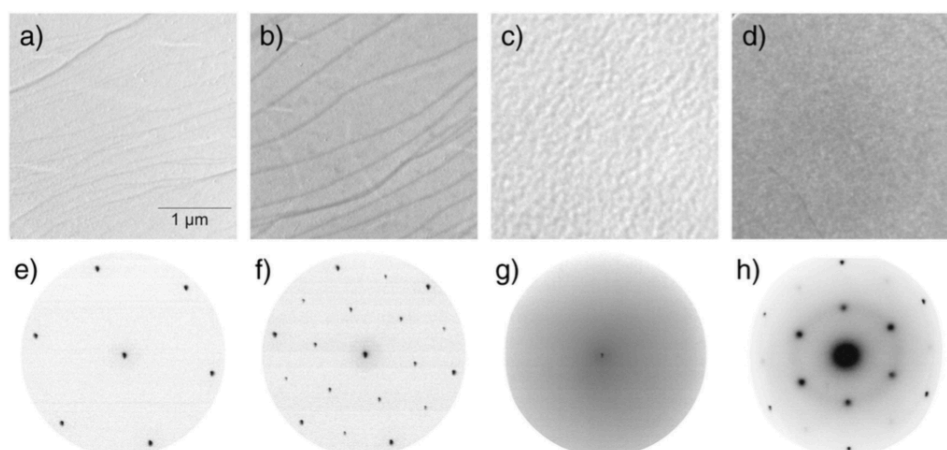


Figure 1.30: LEEM and LEED study during different steps during the growth of bilayer silicon oxide by post-oxidation. (a, e) bare Ru(0001), (b, f)  $(2 \times 2)$ -3O/Ru(0001) reconstruction, (c, g) Si deposition and (d, h) post-oxidation. Adapted from [52].

implication of high strain in the film near the edges or near bonding of the film to un-saturated silica rings. These de-wetted areas show black and grey patches, representing monolayer silicon oxide and oxygen reconstruction on the Ru(0001) surface. The temperature effect can be seen in the LEED patterns. Interestingly the growth of a  $30^\circ$  rotated phase along with a vitreous phase (observable as a ring in LEED pattern) occurs. The rotated phase has been discussed earlier in the section dedicated to defect to grow in the vicinity to the amorphous regions.

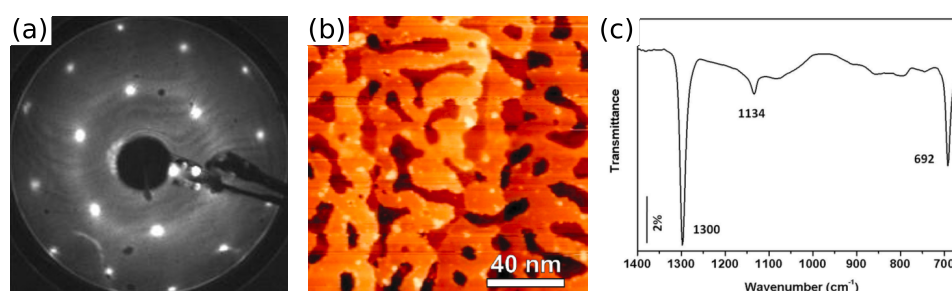


Figure 1.31: Growth of 1.5ML silicon oxide having monolayer and bi-layer components studied by (a) LEED, (b) STM and (c) IRAS. Adapted from [121].

---

The cooling rate after the post-oxidation step, in the case of bilayer as well has been found crucial in controlling the formation of the vitreous phase [121]. The effect of the cooling rate on the structure of the monolayer silicon oxide on Ru(0001) appears, on the contrary, negligible, presumably due to the strong bonding in this case.

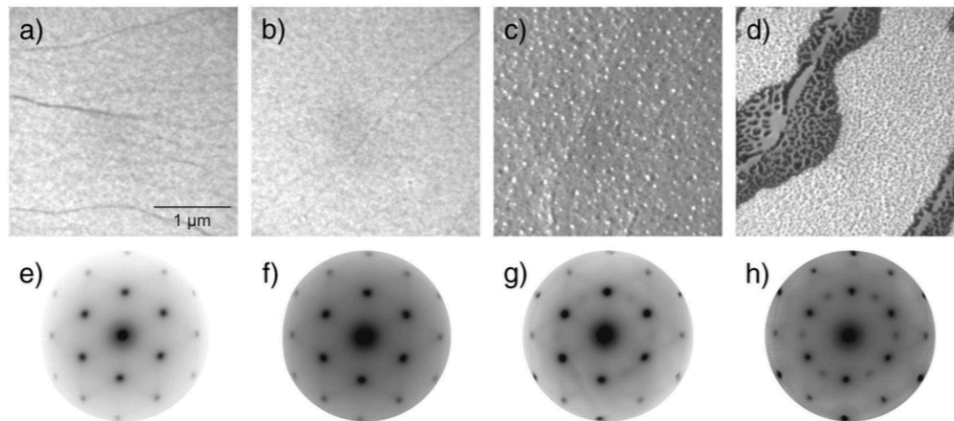


Figure 1.32: LEEM images and corresponding LEED patterns after post-oxidation of bi-layer silicon oxide on Ru(0001) at (a, e) 995 K, (b, f) 1045 K, (c, g) 1095 K and (d, h) 1270 K. Adapted from [52].

### **Chemical Vapour Deposition (CVD)**

The bilayer silicon oxide phase was shown to grow accidentally during the growth of graphene on polycrystalline Cu foils, characterised by diffraction studies shown in Figure 1.33. The Cu foils were attached to a quartz holder and placed into a quartz tube [42]. The tube was pumped down to  $10^{-2}$  mbar and a mixture of Ar/(5%)H<sub>2</sub> was introduced at a pressure of 5 mbar. The Cu foil was heated up to 950° C. At high temperature the Ar-H<sub>2</sub> mixture was cut and hexane vapour under a pressure of 0.5 mbar was introduced for 1 minute. The samples were cooled down. The samples under TEM investigations showed bilayer silicon oxide on top of graphene on Cu. This growth was suggested to occur in response to a leak during the switching of the Ar-H<sub>2</sub> mixture to hexane that oxidised the Cu foil and lead to a reaction with the quartz substrate at the contact surface. The bilayer silicon oxide on graphene could be transferred onto commercial

TEM grids by etching the Cu in 15% nitric acid followed by a fishing technique. Both, the crystalline and the vitreous phases of the bilayer silicon oxide are visible in the FFT-mode of STEM experiments, shown in Figure FFT-STEM. The 7% lattice mismatch between graphene and bilayer silicon oxide is also evident.

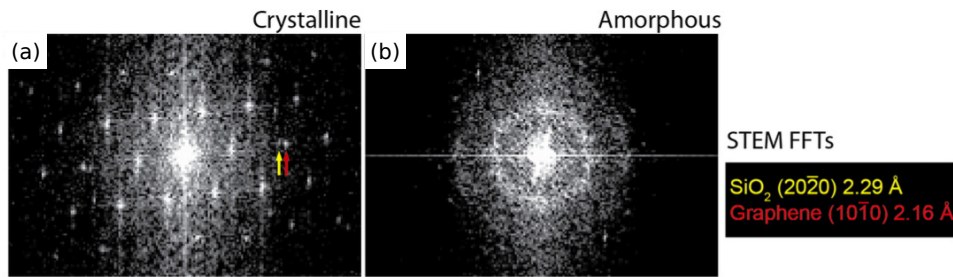


Figure 1.33: FFT-STEM on HBS on graphene in (a) crystalline region and in (b) amorphous region. Adapted from [42].

### Surface segregation from metal platelets

At 450° C, monolayer and bi-layer silicon oxide have been grown by F. Ben Romdhane *et al.* on the surface of metal platelets. The 5 nm thin film of metals, Co, Ru and Fe, were deposited by sputtering onto 10 nm thick SiO<sub>2</sub> films. These metallic films transformed into isolated crystalline nano-platelets (10 nm thick) of Co and Fe or crystalline film of Ru upon annealing to 700° C, shown in Figure 1.34 (a). After cooling down to 450° C monolayer silicon oxide started to grow (Figure 1.34 (b)). The hexagonal lattice of silicon oxide overlapping with the lattice of Co can be seen in the Figure 1.35 (a). The nucleation was observed at the intersection of the planar defects with the metal surface, after which the network grows laterally in the  $[10\bar{1}0]$  direction at a speed of 0.4 nm/sec, (Figure 1.35 (a-d)) [7].

The formation of the monolayer silicon oxide is proposed to occur via bulk or surface diffusion of the atomic species. DFT proposes an interstitial migration barrier of 0.8 eV on Ru and 1.2 eV on Co surfaces that can be overcome at the temperature at which the experiments are performed. The Si atoms, diffusing through the grain boundaries, and oxygen, evolving from the *amorphous*-SiO<sub>2</sub> substrate or the native oxide of metal particles, undergo a surface reaction to form silicon

---

oxide and get pinned at the planar surface defects or step-edges where the monolayer and bilayer silicon oxide nucleate [7].

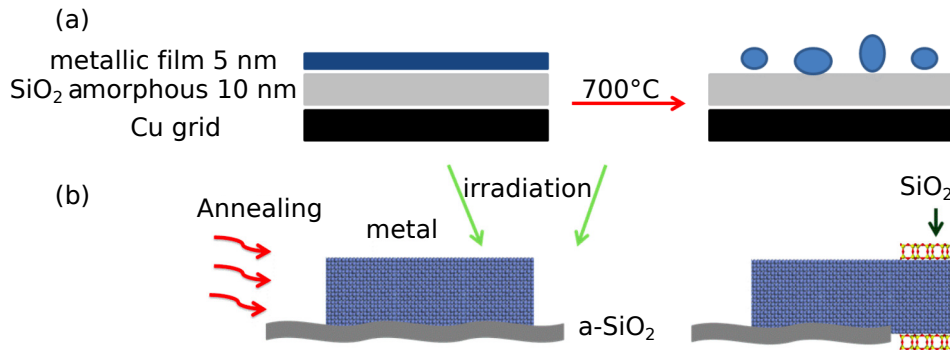


Figure 1.34: The schematic for the growth of two-dimensional silicon oxide by surface segregation. (a) Transformation of the metal thin film into nano-platelets at 700° C. (b) Annealing of the nano-platelets on SiO<sub>2</sub> at 450° C yielding the two-dimensional phase of silicon oxide. Adapted from [7].

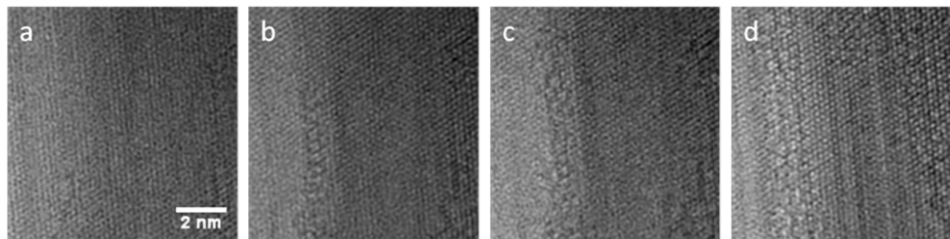


Figure 1.35: Nucleation of monolayer silicon oxide on Co(0001) and its growth in seen in a span of 250 seconds (a-d). Adapted from [86].

# Chapter 2

## Means and Methods

A multi-technique ultra high vacuum (UHV) ensemble (Figure 2.1 (a)) composed of four chambers is used as a platform to perform the experiments related to the growth and structural characterisation of the monolayers, like graphene, silicon oxide, etc. Connecting all chambers is a 3.5m long tunnel, also held under UHV, through which the samples can be transferred between the chambers. This tunnel is divided into two parts *via* a pneumatic valve. The first part is pumped by a turbo molecular and a primary rotary pump down to  $2 \times 10^{-8}$  mbar. This section is a fast load-lock used as the entry point for the samples mounted on top of a Zr-Ta-Mo alloy based plate jacketed into a molybdenum sample holder (called as "molybloc"). The second part of the tunnel, held in the low  $10^{-10}$  mbar range, connects the four UHV chambers. There are three transfer rods for picking and placing of the samples from/to the tunnel to/from the sample stages of the UHV chambers.

The first chamber, labelled as Chamber1 in Figure 2.1, hosts a sample holder with a heating stage in range of  $30 - 750^\circ \text{C}$ , and is capable of accommodating eight materials as targets for pulsed laser deposition (PLD). A collimated electron beam with an energy range of  $10 - 50 \text{ keV}$  is housed for reflection high energy diffraction (RHEED) studies. This chamber is also equipped with two electron-beam evaporators.

The second chamber, labelled as Chamber2 in Figure 2.1, has a base pressure of  $2 \times 10^{-10}$  mbar, is equipped with a variable heating furnace working in the range of  $30 - 1500^\circ \text{C}$ . This chamber



---

is equipped with an ion gun that can be used to clean the surface of single crystals. A secondary electron detector, to detect the secondary electrons emitted from the surface upon being hit by ions from the gun, makes it possible to visualise the etching process. This chamber also possesses a gas inlet 1 cm in diameter which can be placed 1 cm away from the sample surface to locally increase the partial pressure of a gas introduced through a leak valve. An Auger electron spectroscope is also available in this chamber to obtain chemical information of the surface. The chamber is often used as a repository for the samples.

The third chamber (inside view in Figure 2.1 (b)), labelled as Chamber3 in Figure 2.1, with a base pressure of  $2 \times 10^{-10}$  mbar, was recently installed into the ensemble, and is the most exploited chamber during the tenure of this thesis. Part of the movements of the different parts (sample holder, quartz microbalance, molybloc holder) are motorised and controlled with a computer. Using a long transfer rod the molyblobs can be transferred to the molybloc holder of the chamber from the tunnel. Later with a wobble-stick, the plates carrying the samples can be placed into an electron beam-assisted sample heating stage. This heating stage is controlled by a feedback thermocouple to operate within the range of  $30 - 1200^\circ \text{C}$  (using electron bombardment to reach temperatures  $> 500^\circ \text{C}$ ). The thermocouple is placed about 1 cm away from the sample itself. So for more reliable temperature measurements a pyrometer is used. With the help of copper brades connecting the sample holder to a small He reservoir, the sample can also be cooled to  $-170^\circ \text{C}$ . The chamber also includes a two pocket electron beam-assisted evaporator from which silicon was for instance deposited during the experiments. The deposition rates are monitored using a quartz microbalance which can be positioned at the sample location. To prepare the single crystal surfaces or intentionally induce defects in the grown films, this chamber is equipped with microwave assisted ion sputter gun. The process of surface preparations is described in the next section. There is also an adjustable quartz nozzle (attached to the gas leak valve) for gas leak close to the substrate surface to achieve high local pressures of the gas. While leaking oxygen on a Ru(0001) surface, a local pressure three times larger can be obtained when

---

placing the quartz nozzle close, 2 cm from the surface compared to the case when the nozzle-sample distance is 10 cm. An electron gun to perform RHEED experiments is available. The diffraction patterns observed by shining the electron beam on the surface, is revealed on a fluorescent screen. The patterns are recorded with a high speed camera interfaced through a high speed bus controlled by a software. Data acquisition is controlled by a software developed at CEA-INAC by Yoan Curé. This setup is capable of monitoring the deposition and growth of the ultra-thin films *in operando* as growth proceeds, with video rate, and high dynamical data range, coded across 16 bits. This chamber also encompasses a residual gas analyser to monitor the gaseous species present inside the chamber and a dedicated evaporator for alkali atoms (which was not used in the framework of this work).

Lastly, the fourth chamber, labelled as Chamber4 in Figure 2.1, with base pressure  $< 5 \times 10^{-11}$  mbar, hosts a room temperature Omicron scanning tunnelling microscope (STM), detailed in next section, used for surface scrutiny. It also includes a large carousel to store samples and STM tips under high vacuum.

We note that during the PhD thesis, the whole system was moved to a new experimental room, which resulted in a long interruption period of almost six months, and was followed by many failures of some of the key parts of the UHV system.

## **2.1 Scanning tunnelling microscopy (STM)**

### **2.1.1 Principle of operation**

Scanning tunnelling microscopy (STM) is a powerful technique used to study structural and electronic characteristics of the surface of conducting samples. This technique is based on the quantum mechanical tunnelling effect according to which a particle can tunnel through potential barriers higher than its potential energy if resonant states or an overlap in the wave function of the particle are available on both sides of the barrier. The wave function of the particle, which is an electron in this case, in a potential barrier of width  $d$  is given

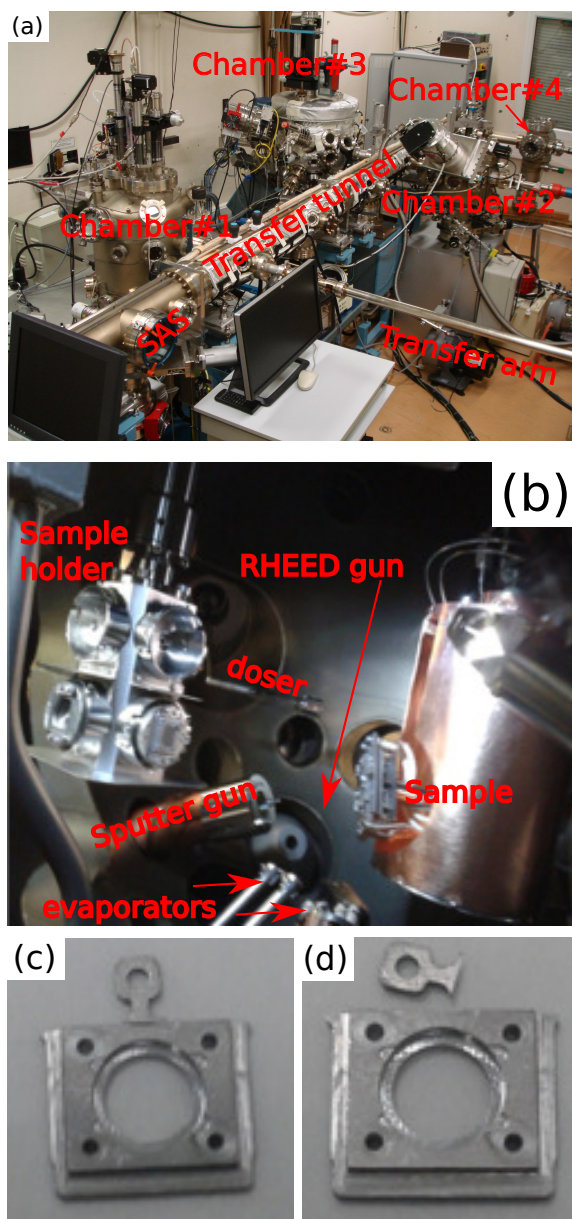


Figure 2.1: (a) UHV ensemble. (b) Inside view of the chamber # 3 used for the growth of the monolayers hosting a electron beam assisted heating stage, sputter gun, reflection high energy electron diffraction (RHEED), electron beam assisted evaporator. Omicron plates for mounting metal single crystals - (c) intact and (d) broken.

---

by [115]

$$\psi(d) = \psi(0)e^{-kd} \quad (2.1)$$

where  $d$  the inverse decay length,  $k$  is the electron wave vector given by

$$k = \sqrt{(2m(V_B - E)/\hbar^2)} \quad (2.2)$$

where  $V_B$  is the height of the barrier, and  $E$  is the electron energy

The probability of the electron to tunnel is given by the square of the wave function which is proportional to the tunnelling current.

$$|\psi(d)|^2 = |\psi(0)|^2 e^{-2kd} \quad (2.3)$$

$$I \propto e^{-2kd} \quad (2.4)$$

Thus, the electron has a non-zero probability to tunnel through the barrier. That gives rise to a tunnelling current which decays exponentially with increasing width of the barrier.

In STM, a conductive tip is brought close to the surface of the sample. At this stage both the Fermi levels, in tip and sample, are equal giving rise to a non-zero tunnelling conductance. Application of a bias between the tip and the sample generates a finite tunnelling current through the vacuum. Since according to equation 2.4 the tunnelling current decays exponentially on increasing the barrier width, the tip – sample distance is maintained  $< 10 \text{ \AA}$ . The tip is connected to piezoelectric transducers that allow raster scanning of the surface in the x-y direction.

We use our STM in a constant current mode, where with the help of a feedback setup the tunnelling current is kept constant by manipulating the tip-sample distance accordingly while scanning. The feedback loop consists of a current amplifier that transforms the tunnelling current into voltage and compares to the set values. In order to maintain the reference setting, the tip moves in the  $z$  direction thanks to a bias applied to piezo-electric element holding the tip, to fit the tip-sample distance and the current value. This bias applied to the piezo-electric element is recorded in terms of the

topography of the surface. The other imaging mode in which the current varies in response to a change in real height of the surface is also often used.

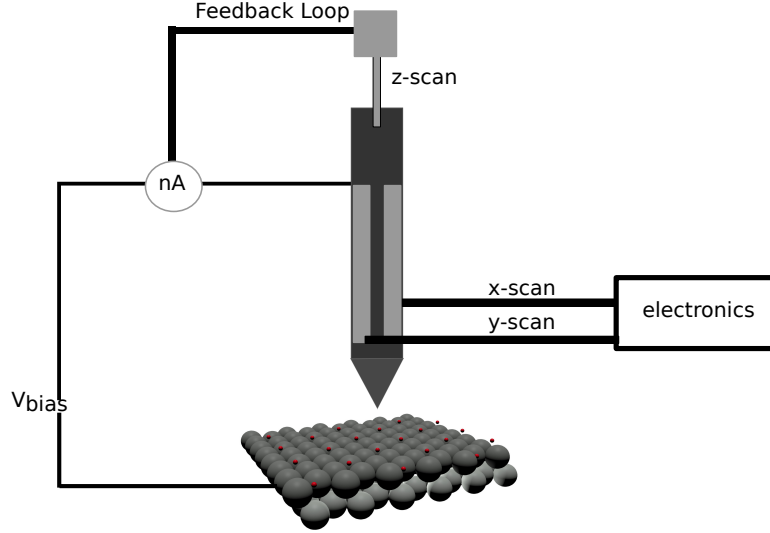


Figure 2.2: The schematic diagram of scanning tunnelling microscope.

### 2.1.2 Tunnelling conductance

A first order perturbation theory yields, for the tunnelling current measured at a tip-sample bias ( $V$ )

$$I(V) = (2\pi e/\hbar) \sum_{\mu} f(E_{\mu})(1 - f(E_{\nu} + eV)) |M_{\mu\nu}|^2 \sigma(E_{\mu} - E'_{\nu}) \quad (2.5)$$

where  $f$  is the Fermi distribution function,  $M_{\mu\nu}$  is the tunnelling matrix element between state  $\psi_{\nu}$  of the tip and state  $\psi_{\nu}$  of the surface, and  $E_{\nu}$  is the energy of state  $\psi_{\nu}$  in the absence of tunnelling. In the limit of small  $V$ , this equation can be rewritten as [106] :

$$I = (2\pi/\hbar) e^2 V \sum_{\mu\nu} |M_{\mu\nu}|^2 \sigma(E_{\nu} - E_F) \sigma(E_{\mu} - E_F) \quad (2.6)$$

with  $E_F$  the Fermi energy.

According to the Bardeen theory [115], and assuming that the tip is ended with one atom, whose s-orbital dominates the tunnelling, this equation can be used to derive the conductance  $I/V$

$$\sigma \propto \rho_t(E_F)\rho_s(E_F) \quad (2.7)$$

where  $\rho_t$  and  $\rho_s$  are the tip and sample electronic densities of state (DOS). This expression shows that, in the the case of small tip-sample bias, which is in practice attained when recording the differential conductance, the signal gives direct access to the electronic density of states at Fermi level. The height measured in an STM experiment is hence not a true height. It is an apparent height, modulated by the local DOS, *i.e.* by the local composition of the sample.

Even if not fully rigorous, the intensity can be inferred from equation 2.7 in the case of large  $V$ , by summing contribution between Fermi level and tunnelling bias [57]

$$I \propto \int_{E_F}^{E_F+V} \rho_s(E)dE \quad (2.8)$$

assuming a flat tip DOS (see next section).

As shown in Figure 2.3, this expression implies that for a negative  $V$  applied to the substrate, STM will probe the occupied DOS of the sample, while for positive  $V$  applied to sample STM will probe unoccupied DOS of the sample. Overall, strong changes of the contrast may be expected upon varying the tip-sample bias sign.

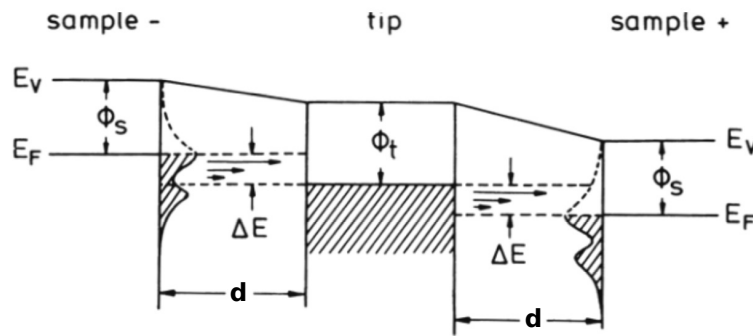


Figure 2.3: Tunnelling process between the tip and the sample surface with (left) negative bias to sample and (right) positive bias to the sample. Adapted from [9].

---

### 2.1.3 Choice and preparation of the STM tip

As apparent in equation 2.7, the DOS of the top modulates the conductance measured in STM. Tips with flat DOS, made of metals like Pt, Pt-Ir alloys, Au, or W are often used to perform scanning tunnelling microscopy with the purpose of determining the DOS of the sample. When thinned down to an apex of one atom, the influence of the tip of such metals is well accounted for by assuming a s-like spherical orbital [24]. Other kinds of tips, with specific termination, are not properly described under this assumption [76].

It is the case of metal tips functionalised with H<sub>2</sub>, D<sub>2</sub>, Xe, CH<sub>4</sub> [49] [105], CO [37] or carbon nanotube [95] for instance. Such tips may have, instead of a s-character, a p<sub>z</sub> or d<sub>z<sup>2</sup></sub> orbital termination. Besides being more directional, than s-type tips, such tips involve specific matrix elements in equation 2.5, associated with specific tunnelling selection rules. Overall, with such tips increased spatial resolution can be achieved and specific features or the sample DOS can be emphasised.

The preparation of metal tips varies from mere cut of a metal wires, as it is often the case with ductile materials such as Pt or Au, to more advanced processes involving electrochemical etching, as it is the case for W. The latter makes it possible to control the shape of the tip in a rather reproducible way. Due to the propensity to oxidation moderate annealing and ion beam etching are often performed. We use this method to prepare our STM tips.

On purpose of preparation of a non-s-type tips usually involves adsorption of, *e.g.* CO molecules on a clean metal surface at low temperature (when molecular surface diffusions are hindered), followed by controlled pick-up with the STM tip thanks to a short tunnelling current pulse forcing the tip to approach close to the surface. Picking-up of surface ad-species can also occur in a regular STM experiment in a less controlled fashion. This is usually apparent as an abrupt increase of the lateral resolution or change in imaging contrast. An example of such an event is shown in Figure 2.4, which reveals a marked change of contrast when imaging the (2 × 1) – O reconstruction of Ru(0001). The highest-resolution STM data presented in Chapter 3, which show strong chemical contrast between Si and O

---

atoms, presumably was obtained with W tips possessing specific (uncontrolled) termination.

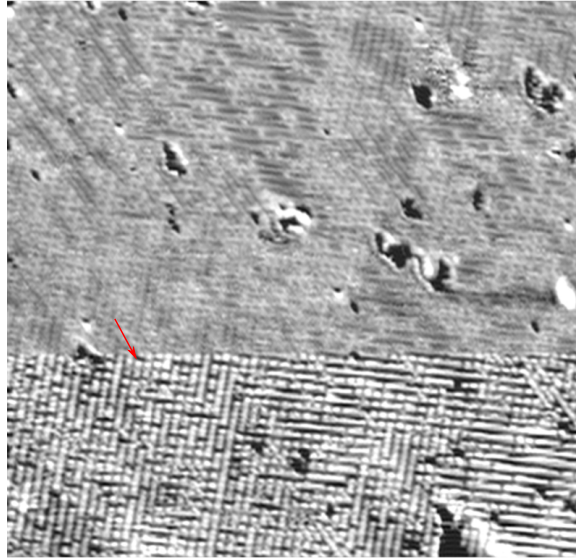


Figure 2.4: Change of tip middle of the scanning on  $(2 \times 1)$  oxygen reconstruction on Ru(0001). The angle between the dense O rows is not  $120^\circ$  as it is expected, due drift during imaging.

## **2.2 Reflection high energy electron diffraction (RHEED)**

---

Reflection high-energy electron diffraction (RHEED) is a versatile technique for examining the structure of the surface and for monitoring the epitaxial growth of surfaces in UHV conditions. It employs a high energy collimated electron beam, typically a few 10 keV in energy, from the electron gun that is directed to the surface at a grazing angle. The energy component perpendicular to the surface (on order of 100 eV), yields low penetration depth of the incident electron beam limited to only the first few atomic planes. The surface atomic rows act like a grating that diffracts the electron beam. The diffraction pattern, in form of spots or streaks is formed on a fluorescent screen placed opposite to the electron gun. The pattern can be recorded through a high speed camera from the screen.



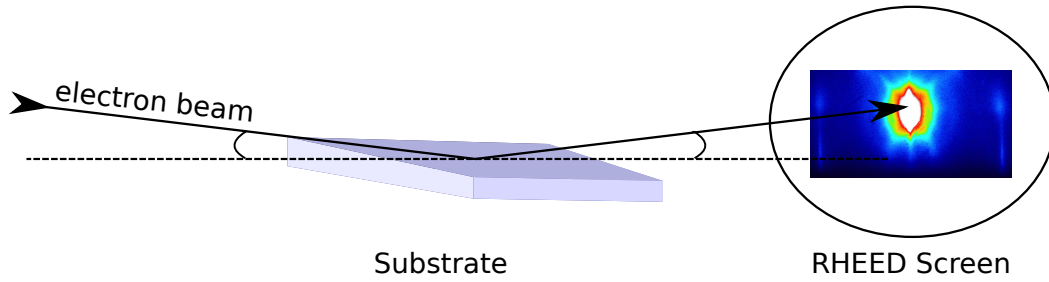


Figure 2.5: RHEED geometry.

The reciprocal lattice for a crystal surface consists of 2D array of narrow crystal truncation rods perpendicular to the surface spaced  $2\pi/a$  apart, where  $a$  is the surface lattice constant. The incidence wave vector is given as  $k_0 = 2\pi/\lambda$ . Considering elastic scattering only, the final wave vector of electrons  $k$  has the same absolute value as the wave vector of the incident electrons,  $k_0 = k$ . The difference between the two vectors defines the scattering vector,  $\vec{Q} = \vec{k}_0 - \vec{k}$ . Since the length of the two is equal, the scattering vector must lie on the surface of a sphere of radius  $2\pi/\lambda$ . This sphere is called the Ewald's sphere (Figure 2.6) [69]. The points where  $\vec{Q} = \vec{G}$ , a reciprocal lattice vector, intersects the Ewald's sphere, defines a diffraction condition. Due to the non-zero energy distribution of the electron beam, the Ewald's sphere has a certain thickness. This, combined to the broadening of the crystal structure rods due to either the coherence length of the electron or the finite size of the crystal, yields streaks, instead of spots in the diffraction pattern.

The  $k$  vectors are indexed according to the angles they make with the substrate. The smallest angle gives rise to the (00) streak. In surface diffraction, the (00) rod necessarily intersects the Ewald's sphere, making the diffraction conditions for it to be always satisfied. Thus the corresponding streak is always seen. This streak is known as the specularly reflected streak. The following rods intersecting the sphere are labelled sequentially. According to the geometry of the RHEED setup, only low order streaks can be detected.

The coherence length, across which the electron wave remains coherent (in phase) is written as:

$$L_c = \lambda/2\beta \quad (2.9)$$

---

where  $\lambda$  is the wavelength of the electrons and  $\beta$  is the electron beam divergence.

At 10 keV,  $L_c = 10$  nm. When discussing whether a sample has crystalline domains where size could be linked to the diffraction streaks width (accounting for instance to Scherrer formula), one first needs to ensure that  $L_c$  is larger than the expected size.

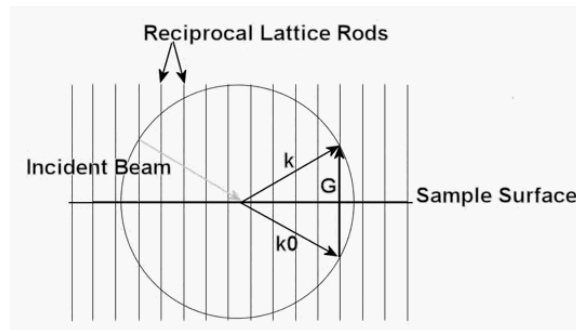


Figure 2.6: Construction of Ewald's sphere.

### 2.2.1 Data interpretation

During the film growth, a high speed camera was used to record the continuously evolving RHEED pattern in real time. The movie recorded was in a 16 bit format, not readable by most movie players or image processing softwares. So prior to treatment, each frame of the movie were first extracted using the FFMPEG program. Afterwards, a code written in Python language was used to read the frames, and to export and analyse the relevant data. To extract the information regarding the RHEED streaks from each frame, the user defines a region of interest (ROI) carefully. From the ROI specified, intensity profiles are plotted against position. To these profiles, gaussian peaks were fitted, using a least squared algorithm, to extract information related to the position of the intensity maxima and the width, of the streak. The ROI needs to be selected carefully. As too large ROIs for instance give too much weight to the tails of the intensity profiles. The ROI can also be extracted from which the intensity can be summed up. This summed up intensity, from all the frames can then be plotted as a function of the duration of the movie recorded.

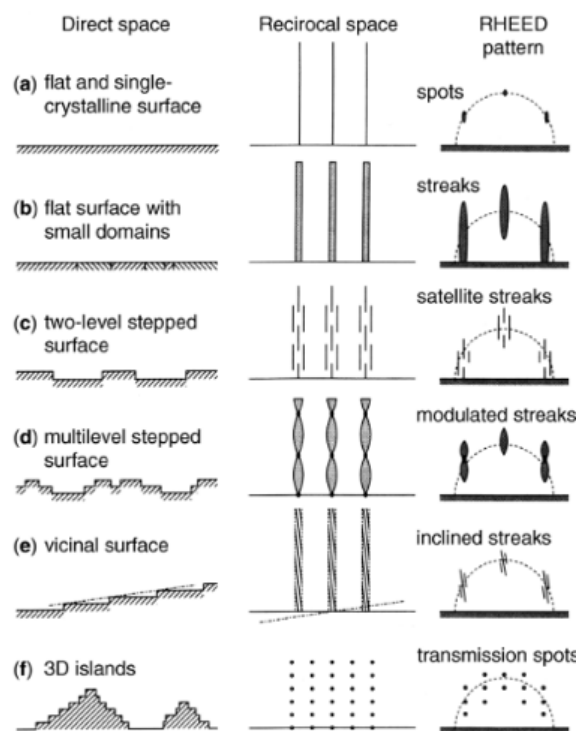


Figure 2.7: Reciprocal lattices and RHEED patterns expected from different surfaces.

---

Such waterfall plots are discussed in the Chapter 4.

## **2.3 Surface preparations of the single crystals**

---

A single crystal of Ru(0001), bought from Surface Preparation Laboratory was borrowed from the ID3 beam line of European Synchrotron Radiation Facility (ESRF). Single crystal can have rough defective surface and impurities dissolved into the bulk all of which needs to be removed to achieve a clean and flat surface appropriate for growth of monolayers. In the case of Ru(0001), the main bulk impurities are C. The surface of the single crystal was cleaned by repeated cycles of sputtering by 1 keV Ar<sup>+</sup> ions from a plasma gun. This step is followed by cycles of annealing the crystal under oxygen back pressure of 10<sup>-8</sup> mbar in which the temperature is raised to 1000° C and then reduced, multiple times, to segregate the dissolved impurities, prominently carbon, which are etched at the surface by the oxygen flux. Then, the crystal is flash annealed to a temperature of 1150° C without oxygen back pressure. This cycling process is continued until a sharp RHEED pattern is achieved (shown in Figure 2.8 (a)). The STM performed on the cleaned surface (Figure 2.8 (b)) shows large terraces on the Ru(0001) surface. During the process of sputtering, argon atoms get implanted into the surface yielding Ar bubbles [38] [44]. These bubbles should leave the crystal during the annealing step, provided the temperature reaches ~1350° C. The bubbles locally strain the Ru lattice in the form of a bulging out of the atomic planes (Figure 2.8 (d)) that correspond to the bright protrusions observed in the STM image (Figure 2.8 (c-d)).

## **2.4 DFT Calculations**

---

Density functional theory (DFT) calculations were carried out using the general gradient approximation (GGA) for the exchange-correlation potential in the PBE version as implemented in BigDFT, a real-space wavelet-based approach. An orthorhombic supercell with

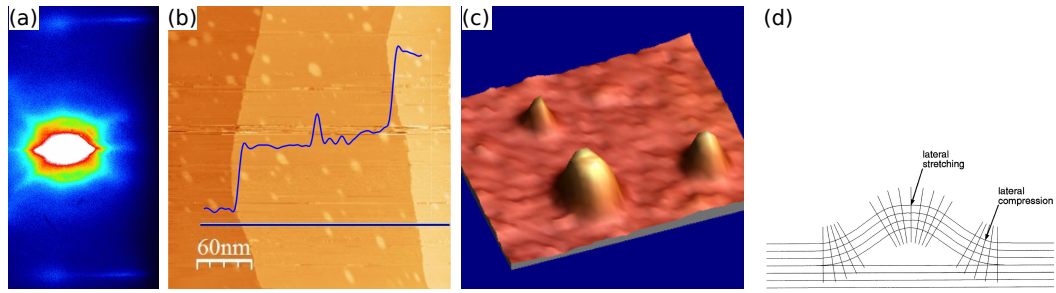


Figure 2.8: (a) RHEED pattern after flash annealing at  $1200^\circ$  and (b) STM image of clean Ru(0001) surface. (c) 3D view and (d) schematic of the argon bubbles. The schematic was adapted from [38].

three layers of Ru atoms was used to model the Ru(0001) surface, onto in which the silica is supported. A 841  $k$ -mesh was used to sample the Brillouin zone of the surface, hence the simulation box had no explicit periodicity in the perpendicular direction of the layer. Geometry optimisations were made using FIRE algorithm. All atoms except those for the bottom Ru layer were fully relaxed until the residual force on any atom in the system was less than  $0.015 \text{ eV/\AA}$ . The STM simulation images were calculated using the Tersoff-Hamann approximation in which the tunnelling current is proportional to the local density of states of the sample at the tip position, and of the tip itself, by integrating both densities of states from the Fermi level to the bias voltage. We assume constant density of states for the tip.

## Chapter 3

# Atomic structure of epitaxial 2D-silicon oxide

As discussed in the introduction, crystalline 2D silicon oxide is proposed to have a honeycomb lattice consisting in two covalently bonded mirrored layers of corner sharing  $[\text{SiO}_4]$  tetrahedrons, forming a bilayer, of which one layer, or a monolayer, can be stabilised on surfaces with similar crystal symmetry like Ru(0001). The Ru(0001) surface has a lattice parameter close to half that of the oxide and thus a priori stabilises the monolayer without (or with few) stress relief defects such as misfit dislocations. The strong interaction between the Ru and oxygen atoms at the tetrahedra bottom apex, presumably, prevents the in-plane mis-orientation between the monolayer and the ruthenium lattice leading to a single crystallographic orientation, evident in diffraction studies [121] [124]. Determining the precise nature of the bonding between the Ru(0001) and silicon oxide and the imposed structure remains pivotal in understanding defect formation, that could open routes to large-area high quality preparation of the ultra thin oxide. A model, predicted stable according to DFT simulations, was proposed that is sufficient to account for photoelectron spectroscopy and STM imaging data. Yet, due to the limited chemical and spatial resolution of the latter data, some of the key features of this model could not be challenged. Here, an analysis of the precise atomic structure of the monolayer silicon oxide on Ru(0001) is presented based on scanning tunnelling microscopy (STM) and density functional theory based calculations (DFT).

---

### 3.1 Probing the atomic structure of monolayer silicon oxide on Ru(0001)

---

Direct imaging of well-defined monolayer silicon oxide grown on Ru(0001) at high resolution has been performed. Here, a room temperature STM was employed in the constant current mode. After extensive tip preparation, atomically resolved images of monolayer silicon oxide could be obtained. The STM topograph (scan size = 2.76 nm  $\times$  2.41 nm) shown in Figure 3.1(a) was recorded at a tunnelling bias of 0.9 V and current of 2 nA. These parameters were maintained to keep the tip-sample distance lower by an order of magnitude, in comparison to earlier reports [121] [63] [113] [107], to 10 M $\Omega$ . This allows to access the fine features in the atomic structure of monolayer silicon oxide on Ru(0001). The topographic intensity profile, of the red dotted line marked with numerals 1-4 in the STM image, shown in the Figure 3.1(b), was studied. Four modulations in the topography could be observed. The triangular arrangement of the atoms was revealed by connecting three nearest neighbouring features of similar intensity. The triangles formed by the most intense features (shown with white sides in Figure 3.1(a)) arrange in a hexagon. These could be assigned as the base of individual [SiO<sub>4</sub>] tetrahedron (pointing towards the Ru surface), in which case the topographic features (marked 2) should be the shared oxygen in the 2D network. The centre of the white triangles overlap with the corners of light and dark blue triangles. These are the expected positions for the silicon atoms according to the structure of the [SiO<sub>4</sub>]. The silicon atoms, as expected, form the corners of the hexagons. These corners show a modulation in the intensity (highlighted by light and dark blue) with one half (marked 1, dark blue) appearing higher (or brighter) than the other half (marked 3, light blue) (appearing lower or darker) according to a three-fold symmetry. These silicon atoms bind to the Ru(0001) via the fourth oxygen atom of the tetrahedra which is not directly accessible to the STM. Besides, each hexagon presents a bright protrusion at the centre, marked by the red dotted circle in the Figure 3.1(a). This central position inside the hexagonal ring of monolayer silicon oxide was proposed to be occupied by an extra

oxygen atom in the DFT calculations performed earlier, but the STM could not detect the oxygen atom at this location to the best of our knowledge.

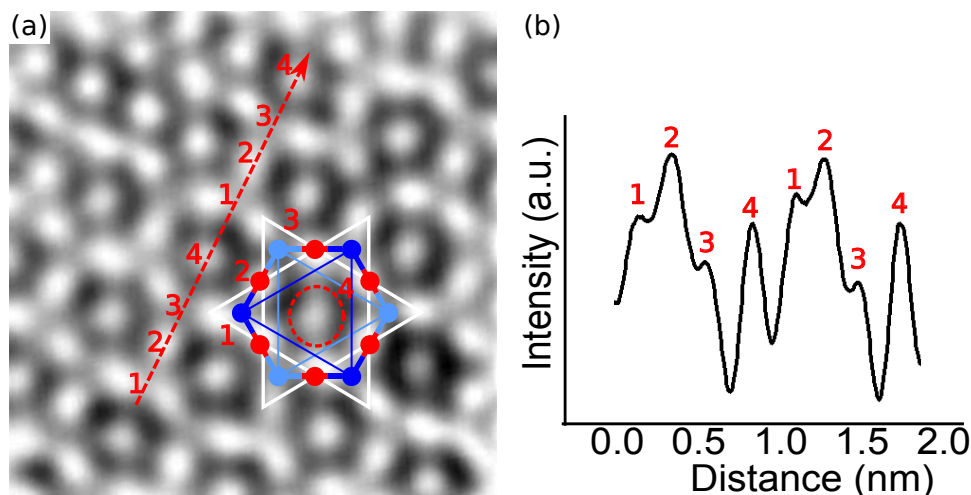


Figure 3.1: (a) Topographic STM image ( $2.76 \text{ nm} \times 2.41 \text{ nm}$ ) taken at  $0.9 \text{ V}$  and  $2 \text{ nA}$  showing the hexagonal arrangement of the  $[\text{SiO}_4]$  tetrahedra (white triangles). The corners of the hexagons consist in silicon atoms (blue) that are bridged by oxygen atoms (red). The bright protrusion at the centre is marked by the dotted red circle. The red dotted line marked with 1-4 indices is the one along which the intensity profile is shown in (b) is extracted. Points 1-4 show the modulation in the intensity according to the four features seen in the STM image.

The observed features provide hints about the epitaxial relation between the monolayer silicon oxide and the Ru(0001) surface. DFT calculations have reported very small ground state energy differences,  $75 \text{ meV}$  [7], in the different possible registries. These registries differ by the occupation of hcp-hollow sites (hexagonal close packed; hollow site formed between three Ru atoms with a Ru atom of the second layer directly underneath), fcc-hollow sites (face centred cubic, hollow site formed between three Ru atoms with a Ru atom of the third layer directly underneath) and top sites (directly top of the Ru atom), shown in Figure 3.2, and are discussed below.

- **Model 1** The corners of hexagons of monolayer silicon oxide



---

occupying fcc-hollow and hcp-hollow sites with centre coinciding with a top-site on Ru(0001) surface (Figure 3.2(a))

- **Model 2** The corners of hexagons of monolayer silicon oxide occupying top- and hcp-hollow sites with centre coinciding with a fcc-hollow site on Ru(0001) surface (Figure 3.2(b))
- **Model 3** The corners of hexagons of monolayer silicon oxide occupying fcc-hollow and top- sites with centre coinciding with a hcp-hollow site on Ru(0001) surface (Figure 3.2(c))

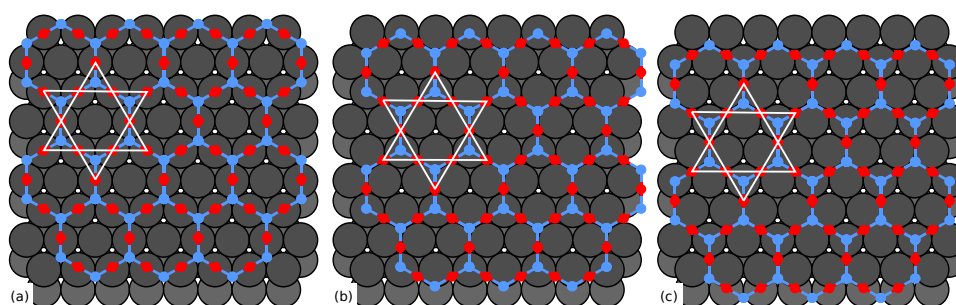


Figure 3.2: Three possible configurations of monolayer silicon oxide on Ru(0001). (a) The monolayer occupies fcc-hollow and hcp-hollow sites with top-sites in the centre. (b) The monolayer occupies hcp-hollow and top sites with fcc-hollow sites in the centre. (c) The monolayer occupies fcc-hollow and top sites with hcp-hollow sites in the centre.

## 3.2 Epitaxial relation between the monolayer and Ru(0001)

---

We calculated partial electron density maps (PEDMs) for the DFT predicted most stable configuration (Figure 3.3 (a)), according to refs [7] [121] to interpret the intensity corrugations observed in the STM micrographs and relate them with the structural registry between monolayer silicon oxide and Ru(0001). In this configuration, there are four kinds of oxygen atoms involved. The silicon atoms, at the centre of the  $[\text{SiO}_4]$  tetrahedra, are expected at the corners of the

---

hexagons formed by Si-O-Si segments (the oxygen atom bridging two silicon atoms is referred as  $O_b$ ). These silicon atoms are bonded to the Ru(0001) surface via oxygen atoms; half directly on top of Ru atoms (referred as  $O_t$ ) and the other half in the fcc-hollow sites (referred as  $O_{fcc}$ ). An additional oxygen atom, not bound to Si atoms, occupies the hcp-hollow sites at the centre of each hexagonal ring of silicon oxide on the Ru surface (referred as  $O_{hcp}$ ). The DFT relaxed model from this configuration is shown in the Figure 3.3 (a). The energy cuts in the PEDMs were taken at two different heights to mimic the different heights the STM probe would have scanned to maintain the constant current via the feedback loop. The constant height PEDM at  $3.5 \text{ \AA}$  from the Ru(0001) surface, (Figure 3.3(c)), shows a single prominent intensity contribution at the position of the  $O_b$  sites where the oxygen atoms terminate the surface. No significant contributions from  $O_t$ ,  $O_{fcc}$  or  $O_{hcp}$  sites were observed. Here, the features of the  $O_t$  and  $O_{fcc}$  may appear lower due to the silicon atom sitting on top of these oxygen atoms and presumably donating electrons to the underlying oxygen, diminishing the density of states available for probing by the STM. The vertically lower position of the  $O_{hcp}$  sites does not allow significant density of states to contribute to the PEDM cut taken at higher position. However, the PEDM cut taken  $2.2 \text{ \AA}$  from the surface (Figure 3.3(d)), to mimic a lower STM probe position, shows more features (three). Two originate from the oxygen atoms at the  $O_t$  and  $O_{fcc}$  sites (which are not directly accessible to the STM probe) where the monolayer silicon oxide binds to the Ru(0001) surface. At the  $O_t$  sites a higher apparent height than at the  $O_{fcc}$  sites is observed in the PEDM cut. This is in very good agreement with the observed intensities along the apparent height profile extracted from the STM image (Figure 3.1(b)). The extra oxygen atoms bound to the hcp-hollow sites,  $O_{hcp}$ , gives the third contribution in the PEDM cut close to the surface and is part of a O-( $2 \times 2$ ) reconstruction on Ru(0001), coexisting with silicon oxide. As seen in the partial overlays of the STM images with PEDM cuts with ball models (Figure 3.3), an overall qualitative agreement is observed, supporting the energetically stable model, by real space imaging. So far, to our best knowledge the resolution of STM images was too limited to support the DFT model in such a direct manner and with such a degree of

---

detail.

By DFT, the coexisting ( $2 \times 2$ ) oxygen lattice in the hcp-hollow sites,  $O_{hcp}$ , was shown to stabilise the system marginally, by  $< 0.1\%$  [7]. The formation of this lattice is proposed as a reminiscent of the precursor to the monolayer and is explained in the next chapter.

As discussed in the introduction chapter, the vibrational and photoelectron spectroscopy data was rationalised by simulations of the spectra on the basis of the stable DFT deduced model. Vibrational spectroscopy performed on monolayer silicon oxide on Mo surfaces is suggested to exhibit features similar in frequency to those expected from monolayer on Ru surface. The vibrational spectroscopy on the monolayer on Mo surface revealed features corresponding to the asymmetric vibration of Si–O–Mo surface at  $1050 \text{ cm}^{-2}$  and symmetric vibrations at  $675 \text{ cm}^{-1}$  and  $771 \text{ cm}^{-1}$ . The stable DFT deduced model (Figure 3.4 (a)) has corroborated these observations [92]. Moreover, based on the stable DFT deduced model, a vibration originating from O–metal bonds at  $671 \text{ cm}^{-1}$  is expected that is clearly originating from the sample surfaces suggesting the presence of extra oxygen atoms bound to the metal (M) [96] (figure 3.4). Such monolayer films have been termed as "O-rich". Furthermore, in the X-ray photoelectron spectroscopy, on monolayer silicon oxide grown on Ru(0001), the asymmetry of the O 1s core level peak, which exhibits a shoulder at low binding energies, indicates that oxygen atoms are involved in different kinds of bonds [92]. The main component of the peak is reasonably attributed to Si-O-Si bonds, while the shoulder component points to mixed Si-O-M and/or M-O bonds. Due to the too limited energy resolution however, it is not possible based on this sole data to clarify which contribution these bonds have, or even if the two kinds of bonds (Si-O-M and M-O) coexist. In simulations of the X-ray photoelectron spectra, based on the DFT model, indeed contributions from Si-O-M and O-M bonds appear very close in binding energy, within 1 eV (Figure 3.4). The comparison between our high resolution STM data and simulations of the images based on DFT calculations makes it possible to lift the ambiguity, and to indeed confirm that the previously published XPS data comprise four components, i.e. that O atoms are involved in four kinds of inequivalent bonds.

Further experimental observations clearly supporting the struc-

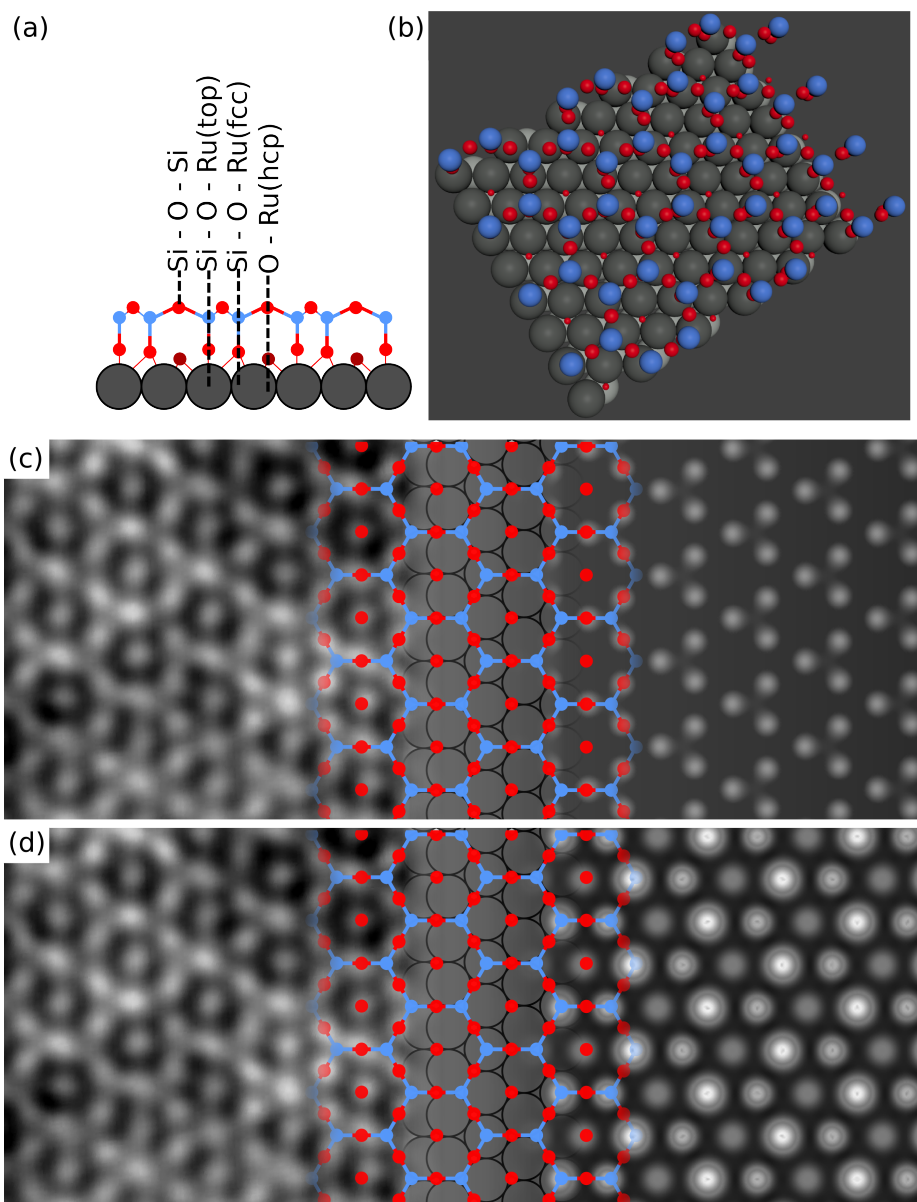


Figure 3.3: DFT relaxed model of the most stable configuration of monolayer silicon oxide on Ru(0001) with (a) side-view and (b) top view. Overlay between STM images ( $2.76 \text{ nm} \times 2.41 \text{ nm}$ ) (taken at 0.9 V and 2 nA) and the DFT based calculation of the partial electron density maps (PEDMs). (c) The right column shows the PEDM cut taken at  $3.5 \text{ \AA}$  above the Ru(0001) surface. The ball model overlaying the PEDM with the STM image (left panel) allows for identifying the feature observed at  $O_b$ , the oxygen atoms bridging silicon atoms. (d) PEDM cut taken at  $2.2 \text{ \AA}$  above the Ru(0001) surface (right panel).

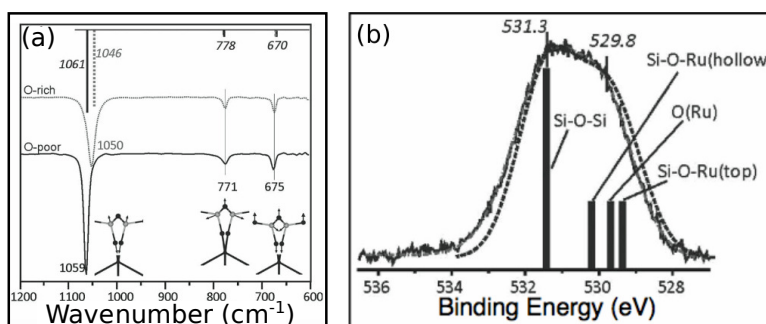


Figure 3.4: (a) Vibrational spectroscopy data of monolayer silicon oxide on Mo(112), both experimental and DFT calculated. (b) XPS data of the monolayer silicon oxide on Ru(0001) (solid line) compared to calculated spectra for the stable DFT model (dotted line with bars). Adapted from [92].

tural model discussed above over the other possible configurations are obtained in vicinity of the silicon deficient regions for partial coverages of monolayer silicon oxide on Ru(0001) (Figure 3.5). The region highlighted by a dotted contour corresponds to monolayer silicon oxide. Bright intensity patches can be seen at the upper edge of the monolayer silicon oxide lattice. These features can correspond to defects in silicon oxide or the oxygen reconstruction underneath. Surrounding the monolayer a  $(2 \times 2)$  reconstruction can be seen. In more accurate terms, this structure is the so-called  $(2 \times 2) - 3O$  (because of involvement of three oxygen atoms) reconstruction on Ru(0001) that is formed alongside the growth protocol (described in the following chapter) employed. Knowing that oxygen atoms exclusively occupy hcp-sites of Ru(0001), this micrograph allows a relative assignment of the centres of the hexagons of the close-by monolayer silicon oxide and of its edges.

In Figure 3.5 (b), a network of lines (green) is drawn, which connects the locations of the O atoms at hcp-sites in the  $(2 \times 2) - 3O$  region, and this network is extrapolated to the silicon oxide region. A network of lines (blue) passing through the centres of the hexagonal rings of silicon oxide is also drawn. We observe that the nodes of these two networks very closely match. As shown in the ball models of the three possible monolayer silicon oxide registries on Ru(0001),

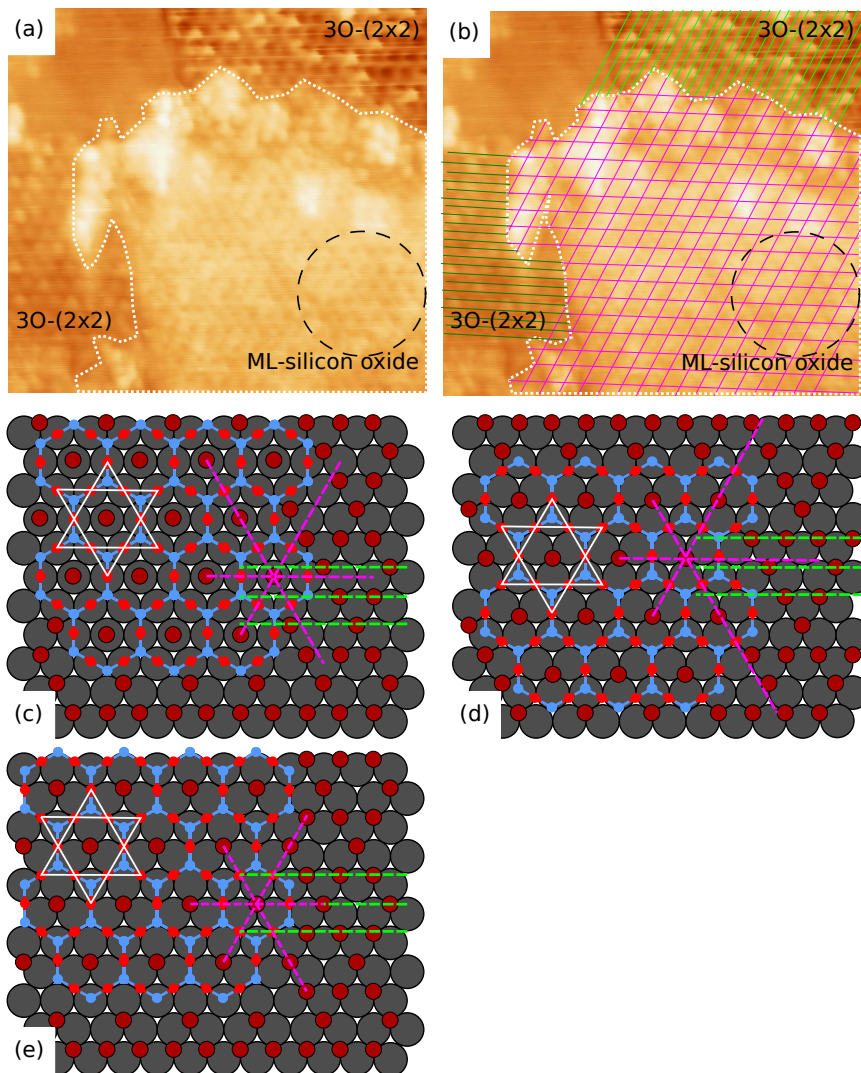


Figure 3.5: STM image ( $12 \text{ nm} \times 13.5 \text{ nm}$ ) of low coverage monolayer silicon oxide. (a) The patch of monolayer silicon oxide is marked in a white border and is surrounded by  $(2 \times 2) - 3\text{O}$  reconstructed Ru(0001) on top and the left sides. (b) Image (a) overlaid by two network of lines, one (green) passing through oxygen atoms (hcp-hollow sites) in the  $(2 \times 2) - 3\text{O}$  phase, the other (pink) passing through centres of hexagonal rings of silicon oxide. The two networks match perfectly. (c-e) Three models, from Figure 3.2, with monolayer surrounded by  $(2 \times 2) - 3\text{O}$  reconstructed Ru(0001) surface. Only model (e) exclusively shows an overlap between the centre of the hexagon and a hcp-hollow site.

---

that were discussed earlier, only model 3 allows the centre of the monolayer hexagon to overlap with the hcp-hollow site of Ru(0001). According to this model, the monolayer binds to the ruthenium lattice in fcc-hollow and top sites, via Si-O-Ru bonds. Taking this analysis into account, the other models (1 & 2), from Figure 3.2, with different epitaxial relation can be discarded.

A similar observation could actually be made from the STM image of 0.3 ML silicon oxide grown on Ru(0001) shown in the PhD thesis of L. Lichtenstein [62], although this analysis was not made so far. The corresponding STM micrograph is shown in Figure 3.6, where a patch of monolayer silicon oxide can be seen as the brighter region and a neighbouring  $(2 \times 2) - 3O$  reconstruction of oxygen can be seen in the darker region. In Figure 3.6(b), the green lines drawn over the oxygen atoms are well aligned with the blue lines drawn through the centre of the hexagons confirming once more the above discussed model of the epitaxial relationship between monolayer silicon oxide and the Ru(0001) surface.

### **3.3 Degenerate epitaxy leading to formation of domains**

---

According to the previous discussion and diffraction experiments (LEED [121] [124]), monolayer silicon oxide has a commensurate structure on Ru(0001) where one hexagon matches two unit cells of the Ru(0001) surface and aligns with the  $[10\bar{1}0]$  direction. No rotational domains are observed. This suggests that the monolayer exists with a very high crystalline quality. Yet it is interesting to note that on the Ru(0001) surface, there exist three equivalent preferential fcc-hollow and top- binding sites for monolayer silicon oxide. The reason for this equivalency is the distinct number of atomic sublattices in Ru(0001) surface and in monolayer silicon oxide. This situation is typical of oxide thin films on metals. In other words, the epitaxial relationship between monolayer silicon oxide and Ru(0001) is degenerate which gives rise to domains, shown as yellow, green and purple coloured hexagonal lattices in Figure 3.7. These domains are laterally shifted one with respect to each other, by a nearest neighbour



---

silica with lines.pdf

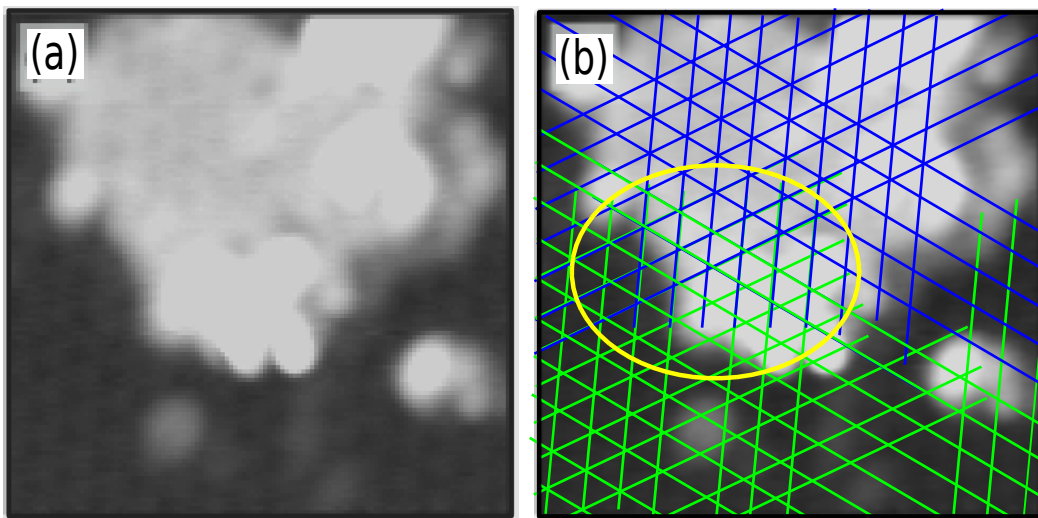


Figure 3.6: (a) STM micrograph of 30 % covering monolayer silicon oxide reported in the PhD thesis of L. Liechtenstein. The bright region is the monolayer silicon oxide surrounded by  $(2 \times 2) - 3O$  reconstructed Ru(0001) surface. Lines drawn in the oxygen lattice (green) marking the oxygen atoms or hcp-sites along with the centre of the hexagons (shown by blue lines). Adapted from [62].



---

distance in Ru(0001), *i.e.*  $2.7 \text{ \AA}$ , which is also half the lattice of monolayer silicon oxide [121] [124]. These domains are termed as anti phase domains. The formation of these anti phase domains can be explained by a global displacive recrystallisation process undergone by the precursor surface in specific crystallographic direction on the Ru(0001) surface corresponding to the zig-zag edges of monolayer silicon oxide. This mechanism is discussed in more detail in the next chapter.

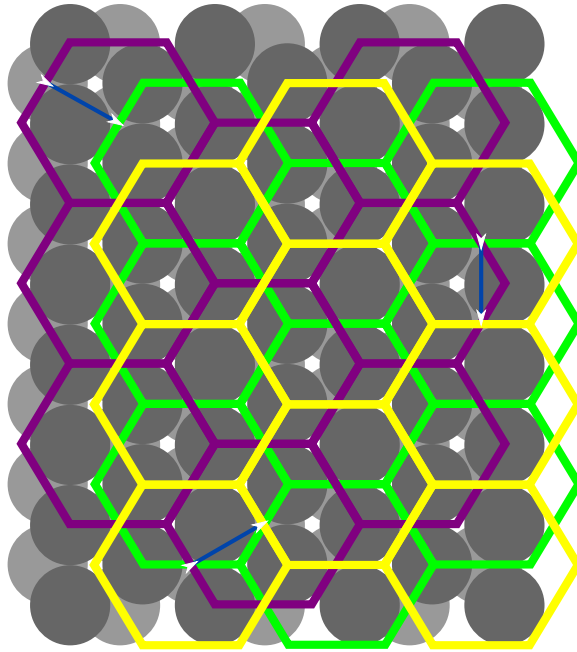


Figure 3.7: The possible degenerate epitaxial relationship of monolayer silicon oxide are seen in green, yellow and purple. The hexagons on Ru(0001) are mutually mis-aligned.

The large scale STM micrograph taken over complete monolayer silicon oxide covered ruthenium reveals anti-phase domains extending across  $7 - 8 \text{ nm}$  laterally, highlighted in yellow, purple and green (Figure 3.8). These degenerate domains are pinned to the support via  $\text{Si-O-Ru}_{\text{top}}$  and  $\text{Si-O-Ru}_{\text{fcc}}$  bonds, with a binding energy of  $-3 \text{ eV}$  per Si atom [7]. This strong interaction maintains a unique crystallographic orientation across the domains (Figure 3.7). This is in contrast to bi-layer silicon oxide on graphene which exhibits rotated domains [42] and to other two dimensional materials, for instance graphene

---

on SiC and metals (e.g. Pt, Ir, Cu) with which it weakly interacts. The weak interaction with the support does not hinder rotation of the crystalline lattice with respect to the substrate surface lattice. In the case of monolayer silicon oxide on Ru(0001), it seems that the strong interaction between the support and the monolayer oxide prevents the formation of large single crystalline domain presumably by hindering translations of the neighbouring domains of monolayer silicon oxide that would be required to align them. This imposes the formation of 1D (line) defects, or anti-phase domain boundaries (APDBs) stitching together and ensuring the continuity of the atomic lattices across laterally shifted domains.

The presence of such anti phase domains in sufficiently small crystals can be detected by diffraction experiments [108]. Such domains, with a mutual translation give rise to a splitting of diffraction spots along the zone parallel to the interface, for the spots for which the product of the structure factor and the displacement vector is a non-integer. The splitting direction is parallel to the normal to the anti phase boundary and the magnitude of splitting is inversely related to the size of anti phase domains. Figure 3.9 shows an optical simulation from sets of 8 points arranged in anti phase domains along with their respective optical diffraction patterns. In Figure 3.9 (a) the displacement vector is  $\mathbf{R}_1 = 1/2 [100]$ ; in the corresponding diffraction pattern the spots along odd  $h$  values are split. Similarly, in Figure 3.9 (b), where the displacement vector is  $\mathbf{R}_2 = 1/2 [010]$ , the spots corresponding to odd  $k$  values are split. Finally in Figure 3.9 (c), the displacement vector is  $\mathbf{R}_3 = 1/2 [\bar{1}10]$ , the spots for which  $-h + k$  is odd are split. Interestingly, such features are apparent in Fast Fourier transforms (FFT) of the STM images (Figure 3.8 (b)), which mimics a diffraction pattern according to the kinematic theory of diffraction. In the FFT calculated through the WSxM software, the splitting of the spots corresponding to monolayer silicon oxide is clearly visible. Since the anti phase domains are shifted in three crystallographic directions, all spots are observed to be split (marked with white arrows with black pointers in Figure 3.8(b)).

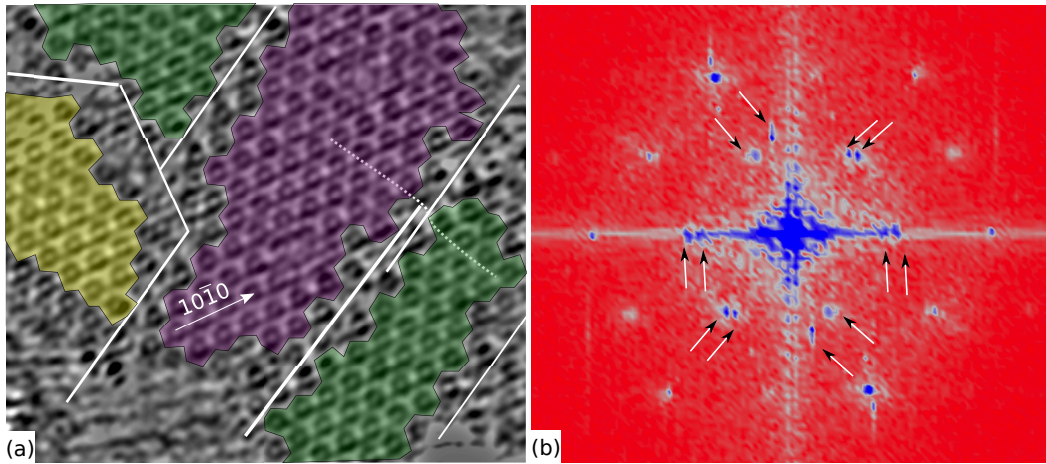


Figure 3.8: (a) Large scale STM image ( $9.5 \text{ nm} \times 8.5 \text{ nm}$ ) taken at  $0.9 \text{ V}$  tunnel bias and  $2 \text{ nA}$  tunnelling current. The anti phase domains of monolayer silicon oxide are highlighted in green, yellow and purple. The white lines mark the anti phase domain boundaries' orientation. (b) FFT of the STM image in (a). The splitting in the spots is demarcated by the white arrows with black pointers.

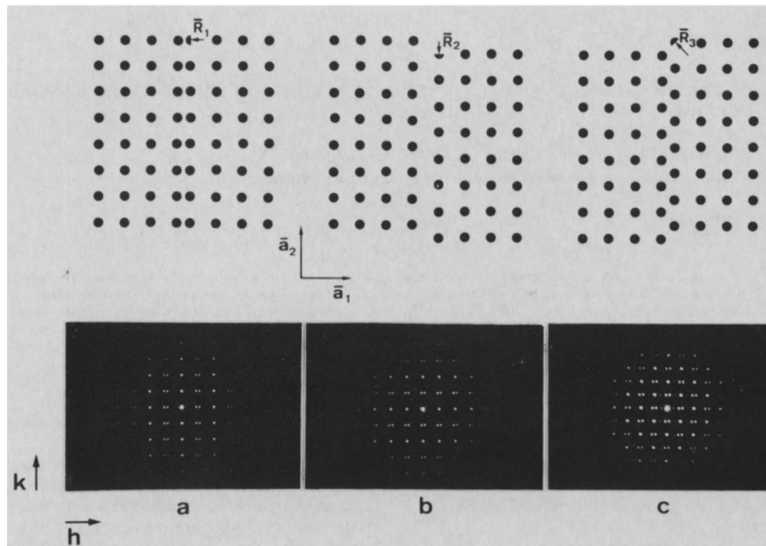


Figure 3.9: Three  $8 \times 8$  dot arrays containing one anti-phase domain boundary. The displacements are marked as  $R_1$ ,  $R_2$  and  $R_3$ . The corresponding diffraction patterns with split diffraction spots are seen in the lower panel. Adapted from [108].

---

### 3.4 Degeneracy driven defects: anti-phase domain boundaries

---

At the interface of these anti-phase domains, discussed above, different kinds of periodic domain boundaries can be constructed depending on the relative direction of the shift. Here we address two limit cases, the most general situation being essentially a combination of both cases. The lateral shift between the domains are all along a armchair direction of monolayer silicon oxide. Two situations may be encountered:

- the lateral shift is perpendicular to the anti-phase domain boundary
- the shift is the resultant sum of two shifts, one cell perpendicular to the boundary and one cell parallel to the boundary

In the first case, when the resultant of two in-plane shifts is perpendicular to the domain boundary, polygons with even number of sides are required to accommodate the mutually shifted domains in a single lattice. For armchair-oriented boundary, pairs of a square and an octagon (8-4-) are expected, shown in Figure 3.10(a). This kind of boundary was observed on the monolayer silicon oxide grown on Mo(112) in previous reports. In case of the monolayer silicon oxide grown on Ru(0001), these can be expected between the domains of monolayer silicon oxide growing at the boundaries of the degenerate reconstruction of the precursor surface of  $(2 \times 2) - 3O$ , as explained in the next chapter. On the contrary, for a zigzag-oriented boundary corresponding to such a shift discussed above, chain of decagons, pentagons and squares are expected (Figure 3.10 (b)).

In the second case, a perpendicular mis-alignment of atomic rows in the hexagonal lattice can only be stitched together by anti-phase domain boundaries comprising polygonal rings with odd numbers of sides. The distinctive apparent heights in the topography of the STM image can be assigned to the corners of the polygonal rings, forming the APDB, occupying the fcc-hollow and top- sites of the Ru(0001) surface. This analysis of the complex topography of the STM image reveals the nature of the APDBs as pairs of pentagons and heptagons,

---

5577, in the armchair direction (Figure 3.11 (a-b)). Further, counting the nearest neighbours to a ring in the boundary also provides clear direct evidence regarding its nature. The heptagons maintain the co-existing oxygen lattice, observed in the hexagonal domains. Inside the pentagons, the presence of central oxygen could not be confirmed by STM as it might have remained hidden from the probe due to the steric hinderance faced in entering the small ring. Another situation, shown in Figure 3.11(b) is an APDB along the zig-zag direction. Our analysis shows that chains containing pairs of two pentagons and one octagon, 855-, can stitch the misaligned domains.

It is noteworthy that solely the domain boundaries in armchair direction mentioned in the first case, discussed above, where the shift is perpendicular to the atomic rows of the lattice, are observed [71]. The boundaries corresponding to the zig-zag direction, in the same case, or others discussed in the second case could never be observed. The structure of these boundaries was only predicted on the basis of a simple analysis of ball models. Rationalising their non-formation or absence on the surface is difficult. The high energetic cost or the cost of corresponding bond breaking/rearrangement for the formation of such boundaries could be the reason behind their absence.

### **3.5 Conclusions**

---

A critical analysis of the atomic structure of monolayer silicon oxide grown on Ru(0001) surface was presented. The precise nature of the bonding between the monolayer and Ru(0001) was rationalised in the vicinity of silicon-deficient regions in the monolayer that maintain the  $(2 \times 2) - 3O$  reconstruction. The alignment between the hcp-hollow sites and the centre of the hexagons provides conclusive evidence of a bonding of the monolayer oxide through O atoms with Ru atoms in fcc-hollow and top sites of Ru(0001). Thanks to the high resolution of the STM images, the apparent height modulation in the silicon oxide hexagons could be interpreted as originating from the varying local chemical environment. Due to the existence of distinct sub-lattices in monolayer silicon oxide, a degeneracy in the epitaxy leading to formation of anti phase domains is discussed. These

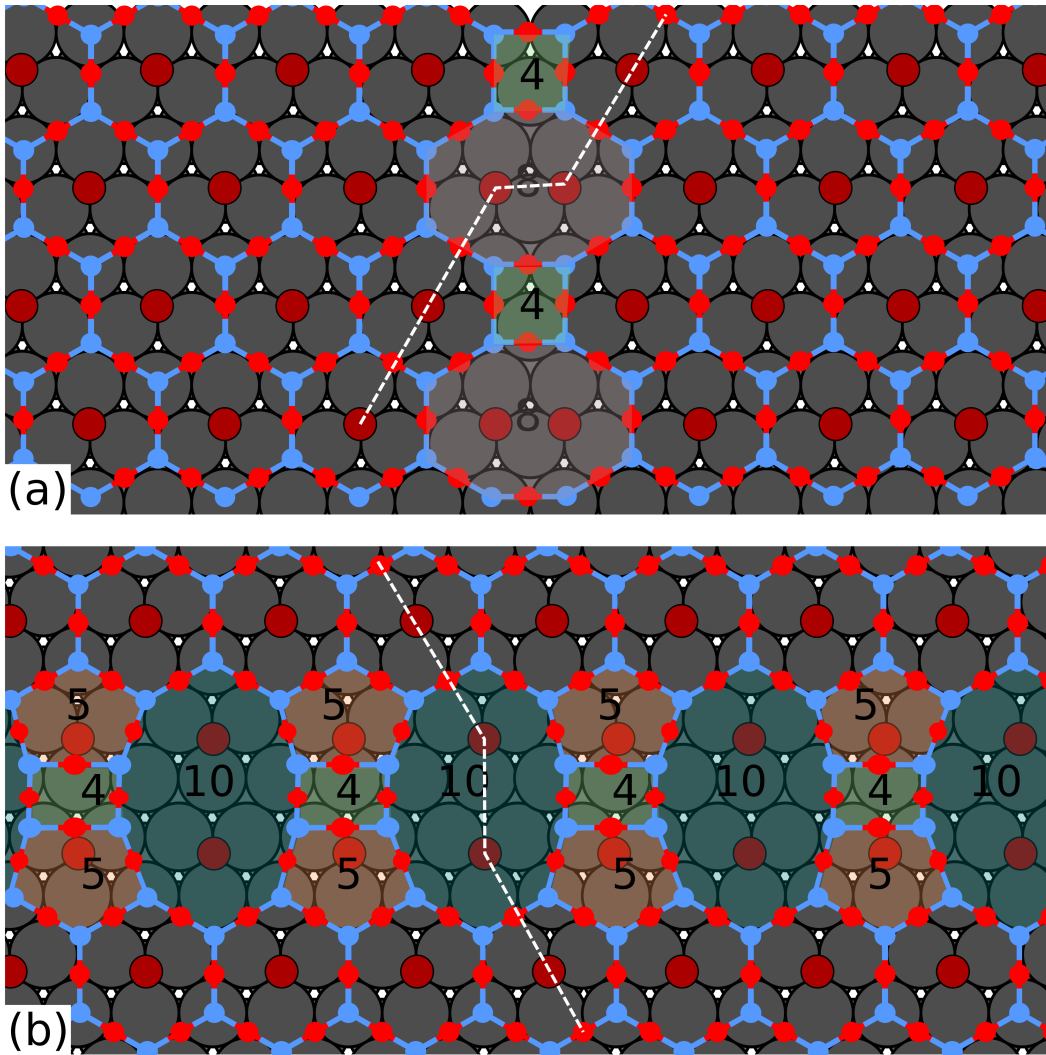


Figure 3.10: Models for anti phase domain boundaries when the shift is in-plane to the atomic rows in the domains are shown in (a) arm-chair direction, 84-, and (b) in zigzag direction, 55410- arrangement.

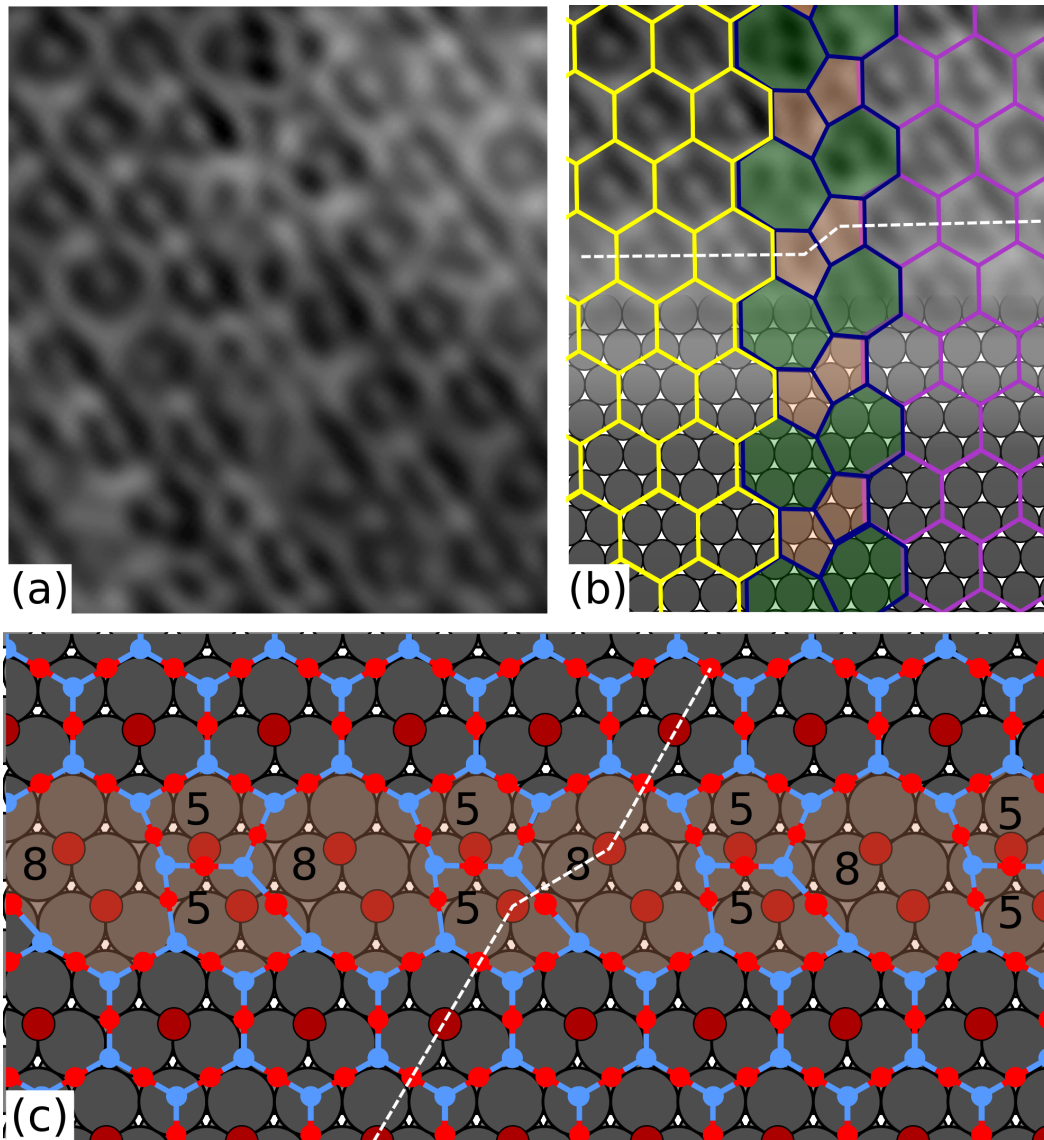


Figure 3.11: Models for anti phase domain boundaries when the shift is perpendicular to the atomic rows in the domains. (a) STM image ( $2.81 \text{ nm} \times 3.17 \text{ nm}$ ;  $+0.9 \text{ V}$  and  $2 \text{ nA}$ ) with the anti phase domain boundary parallel to the arm-chair direction of the silicon oxide hexagons running through the centre. (b) A ball-model overlay of the STM image shows the boundary to comprise in 5577 structure. (c) Ball model of the anti phase domain boundary expected in the zigzag direction.

---

APDs are laterally mis-aligned by  $2.7\text{\AA}$ , *i.e.* the nearest-neighbour distance in  $\langle 1\bar{1}00 \rangle$  directions of Ru(0001), and half the lattice constant of monolayer silicon oxide. Stitching these domains together to accommodate the lateral mis-alignments, pushed us to consider different kinds of boundaries (APDBs). However, only a single kind of APDB, made of 5577- species, in the arm-chair direction of the silicon oxide ( $\langle 11\bar{2}0 \rangle$  direction of the Ru(0001)) is observed in the STM images. Noteworthy, the monolayer silicon oxide domains coexist with a  $(2 \times 2)$  oxygen reconstruction of the Ru(0001) surface inside the hexagons. This oxygen lattice has been suggested to stabilise the system [71].



## **Chapter 4**

# **Step-by-step analysis of monolayer silicon oxide growth**

Heteroepitaxial systems are composed of two distinct crystalline materials forming an interface, which may be more or less well-defined due to the possible intermixing of atoms from the two materials. The interface nature depends on the kind of interaction binding the two materials together. In the case of two-dimensional materials, strong, covalent-like and, weak, van der Waals-like bonds can be formed with the substrate; yet in any case the in-plane atomic bonds must be sufficient to preserve the integrity of the two-dimensional material. In some cases, this requires efforts to avoid the complex formation of undesired compounds. In the case of oxide of silicon on metals, strategies need to be implemented which prevent the formation of silicides, which we will describe. Heteroepitaxy is usually accompanied by effects not found in the idealistic case of isolated materials. Indeed, due to the interfacial bonds with the substrate, and considering the mismatch of the structure between substrate and overlayer (or heteroepitaxial) stresses develop, that are accommodated either elastically by elastic strains in the overlay noticeably, or plastically by defect formation. Defect formation might occur directly at the growth temperature, or as well, when the overlayer and substrate are of different chemical nature, as the temperature is decreased after the growth, due to the mismatch in thermal expansion coefficients. Both

---

situations are typical of two-dimensional materials on substrates.

In this chapter, the growth of the monolayer silicon oxide is analysed step-by-step, and the structure of the material is accessed from the onset of its temperature-induced crystallisation. We pay special attention to strain and associated domain formation.

## **4.1 Growth protocol**

---

The growth of the monolayer silicon oxide on Ru(0001) was performed via post oxidation method, discussed in Chapter 1. This method comprises four steps:

1. Oxygen reconstruction of the clean Ru(0001) surface, protecting the metal surface from silicide formation in the next step.
2. Silicon deposition from an electron beam assisted evaporation system under oxygen back pressure of  $1.2 \times 10^{-7}$  mbar
3. Post-oxidation at  $850^\circ\text{C}$  under  $3 \times 10^{-6}$  mbar of oxygen
4. Slow cooling at a rate of  $\sim 10^\circ\text{C}$  per minute

Steps 1-3 were studied in detail to rationalise the formation of defects and of strain, and are discussed in the following sections.

## **4.2 Oxygen reconstruction on Ru(0001)**

---

Besides preventing silicide formation in the next step, the dissociative adsorption of  $\text{O}_2$  on Ru(0001) into a surface reconstruction of the surface with O atoms provides a reservoir of accessible and reactive species for silicon oxide formation. Maximising the surface coverage with O atoms is hence desirable. The phase diagram of O on Ru(0001) has been extensively explored in the literature from the 1990's where the catalytic activity of Ru surfaces was explored [97]. As the dose of  $\text{O}_2$  delivered at the surface is increased, O reconstructions of increasing O concentrations are formed [73] [72]. The densest O phase is within reach only with molecules other than  $\text{O}_2$ , *e.g.*  $\text{NO}_2$  [99], whose strong oxidising character compensates the decreased

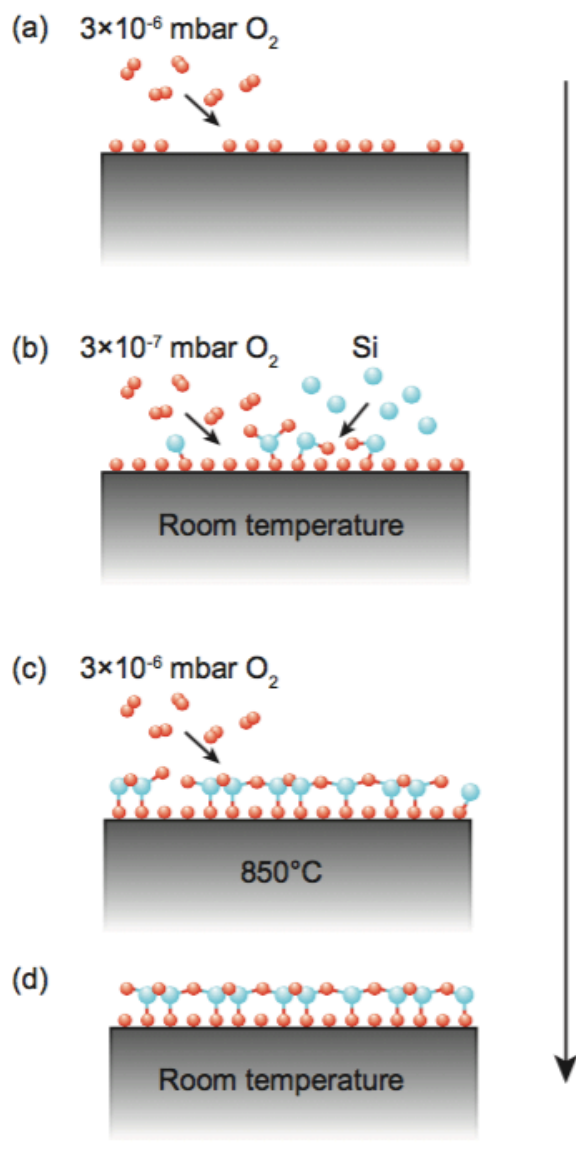


Figure 4.1: The growth protocol for preparation of monolayer silicon oxide on Ru(0001).

probability of dissociative adsorption due to the presence of already chemisorbed O atoms.

Once in the form of atomic O, oxygen binds highly preferentially to hcp-hollow sites on the Ru(0001) [97]. The binding energy decreases as the concentration of the reconstruction increases, due to O–O repulsive interactions [98]. The lowest density phase of O is a  $(3 \times 3)$  reconstruction with one atom per unit cell. Increasing dose yields a succession of phases, from a  $(3 \times 3)$  with 2 atoms per unit cell, a  $(2 \times 2)$  with one O atom per unit cell, a  $(\sqrt{3} \times \sqrt{3})R30^\circ$  with one atom per unit cell, a  $(2 \times 1)$  with one atom per unit cell, a  $(\sqrt{3} \times \sqrt{3})R30^\circ$  with two atoms per unit cell, a  $(2 \times 2)$  with three atoms per unit cell, and finally a  $(1 \times 1)$  with one atom per unit cell [97] (Figure 4.2).

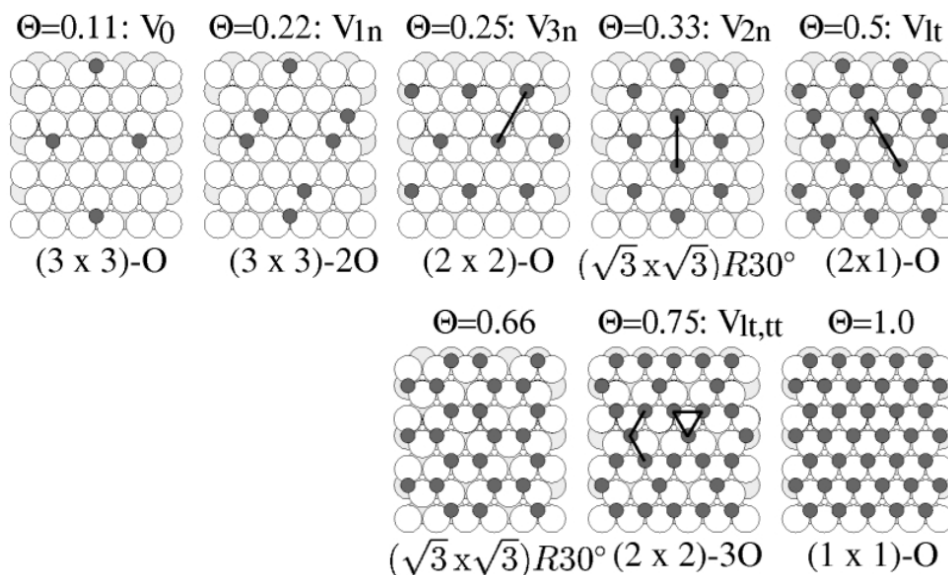


Figure 4.2: Eight theoretically studied phases of oxygen on the surface of Ru(0001).  $\Theta$  denotes the coverage and  $V$  the nearest neighbour energy. Adapted from [97].

In the following, we present RHEED measurements made under a  $10^{-8}$  mbar  $O_2$  pressure in the UHV chamber, while the surface temperature of the sample is  $25^\circ$  C. The study was focussed to a range when the  $(2 \times 2)$  and the  $(2 \times 1)$  reconstructions form. Due to their lattice periodicity twice larger than that of the Ru(0001) surface, the phases yield diffraction streaks half-way between the Ru(0001)

---

streaks and the specularly reflected streak. As the O<sub>2</sub> dose increases, the intensity of the reconstruction streaks varies in a non-continuous manner (Figure 4.3 (c - red curve)).

We first observe an increase of the intensity from 0.7 to 2 langmuirs (L) of O<sub>2</sub> dosed on the Ru(0001) surface (*i.e.* from 70 seconds at the 10<sup>-8</sup> mbar of O<sub>2</sub> back pressure). The intensity then decreases, by ~ 20%, reaching a minimum for a 2.7L O<sub>2</sub> dose. The intensity increases again after this value, first rapidly, then with a much reduced rate.

STM images were taken for the sample exposed to 2.8 and 5 L of O<sub>2</sub> (Figure 4.4 (a,c)). They reveal, respectively, a (2 × 2) (Figure 4.4 (a,b)), and a (2 × 1) reconstruction (Figure 4.4 (c,d)) of O atoms. In the former we note also the presence of lines of O atoms, which are reasonably identified as precursors of the (2 × 1) domains [73]. In the latter case, we note the existence of domains with different orientation of the denser O lines. These orientations are of three kinds, rotated 120° one with respect to the other. We find that the size of the domains is on the order of 7 ± 1 nm (laterally), and in principle are expected in the (2 × 2) phase as well, which are not revealed in Figure 4.4 (a). This point will be discussed in more detail at the end of this chapter.

In the light of STM observations, we now interpret the RHEED data. Each increase of intensity is associated with an increase of the size of the structurally coherent diffraction (2 × 2) or (2 × 1) domains. The dip in the intensity at 2.7L marks the coexistence of (2 × 1) and (2 × 2) domains, and correspond to the resulting maximum disorder.

The first marked intensity maxima allows for estimating the amount O provided through the gas phase and to compare it to the amount of O actually staying at the surface, which is close to 25% for the (2 × 2) O reconstructions. In the framework of kinetic gas theory, the flux of O<sub>2</sub> atoms hitting the surface is  $\phi = P.t / \sqrt{2\pi M k_B T}$ , where  $M$  is the molecular mass,  $k_B$  is the Boltzmann constant,  $T = 300$  K,  $P$  is pressure and  $t$  is the exposure time. Assuming that the coverage is  $\Theta = 25\% = S \times \phi \times \omega$ , where  $\omega$  is the adsorption site area of an O atom, we deduce a sticking coefficient  $S = 0.001$  for O<sub>2</sub> (dissociating into O upon adsorption).

It was unfortunately not possible to observe the transition from

the  $(2 \times 1)$  to the  $(2 \times 2)$  – 3O with RHEED, as it implied the use of higher doses of  $O_2$  pressure, of  $10^{-6}$  mbar which is harmful for the filament of the RHEED electron gun.

We also performed RHEED experiments to study the formation of the reconstructions at a higher temperature of  $350^\circ\text{C}$  (Figure 4.3 (c- blue curve)). In this experiment, in contrast to the former case, the intensity rises much slower. The formation of  $(2 \times 2)$  is observed at a dose of 1.8L, much higher in comparison to the earlier case. The intensity of the reconstruction then falls by  $\sim 50\%$  and stabilises therein. The STM experiments on this surface will be discussed later in section 4.5.

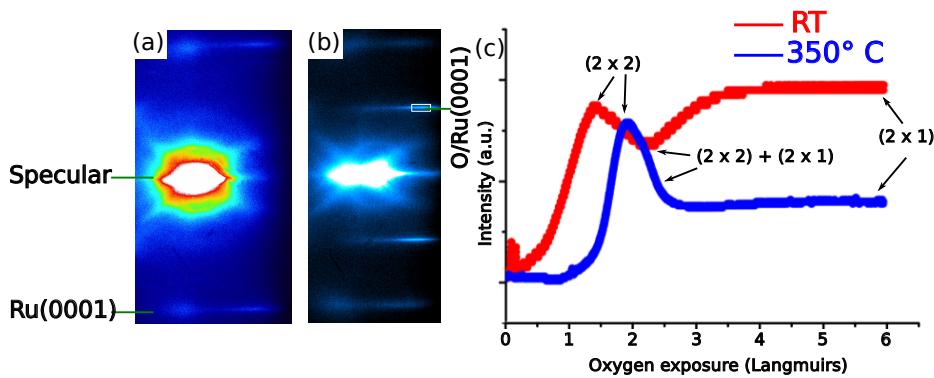


Figure 4.3: RHEED patterns (10keV) from (a) bare Ru(0001) and (b) Ru(0001) exposed to 900L of  $O_2$ . (c) The intensity modulation of the reconstruction streak as a function of oxygen dose.

### 4.3 Silicon deposition

In the second step, the oxygen reconstructed surface of Ru(0001) was exposed to a flux of silicon atoms at room temperature under  $2.5 \times 10^{-7}$  mbar of oxygen. Such a back pressure of O is required to provide the necessary amount of oxygen needed to reach the desired stoichiometry of the silicon oxide. The amount of silicon atoms,  $8 \times 10^{14}$  atoms /  $\text{cm}^2$ , is known to be crucial in determining the thickness of the two-dimensional silicon oxide and thus needs to be controlled precisely. Slight increase leads to the formation of patches

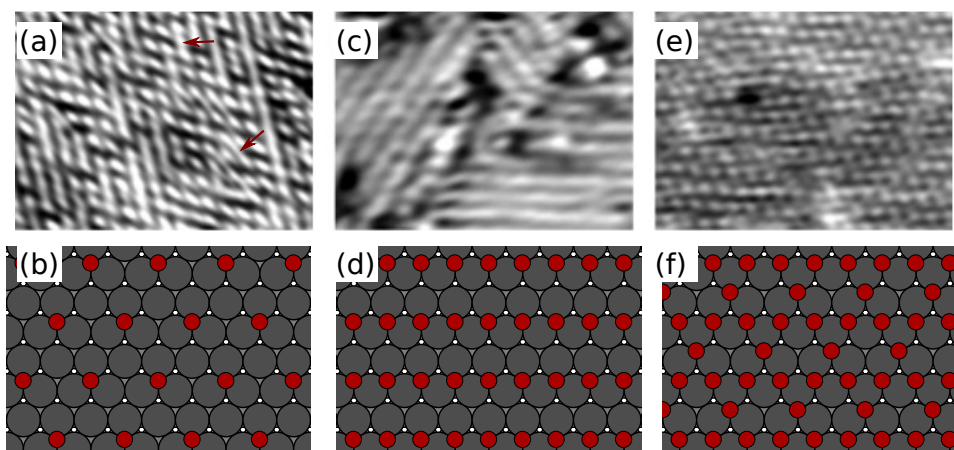


Figure 4.4: STM images and ball-models of various oxygen phases on Ru(0001): (a-b)  $(2 \times 2)$  – O/Ru(0001) mixed with few atom long fragments (exposure of Ru(0001) to 2.5L) (1.4V, 1.7nA). The red arrows mark the nucleation of the  $(2 \times 1)$  reconstruction. (c-d)  $(2 \times 1)$  – O/Ru(0001) (2V, 2nA) (exposure of Ru(0001) to 5L), (e-f)  $(2 \times 2)$  – 3O/Ru(0001) (2V, 0.9nA)(exposure of Ru(0001) to 900L).

of bilayer silicon oxide that might alter the dynamics of the growth [121]. Upon deposition of silicon on the oxygen reconstructed surface, a strong increase of the diffuse intensity of the background of the RHEED pattern is observed. Despite this increase, we still observe the Ru and reconstruction streaks, even if they are weak (Figure 4.5 (a)). This observation suggests that the surface now comprises both crystalline features, which could correspond to the underlying O reconstruction, and possibly as well to a fraction of Si atoms ordered on this reconstruction, as well as a strong degree of disorder.

On a different substrate, Pd(111), DFT calculations suggest that, Si–O dimers form a  $(2 \times 2)$  structure, shown in Figure 4.5 (1-6) [48]. We postulate that such a situation is also relevant on Ru(0001), but that it is associated with a substantial disorder.

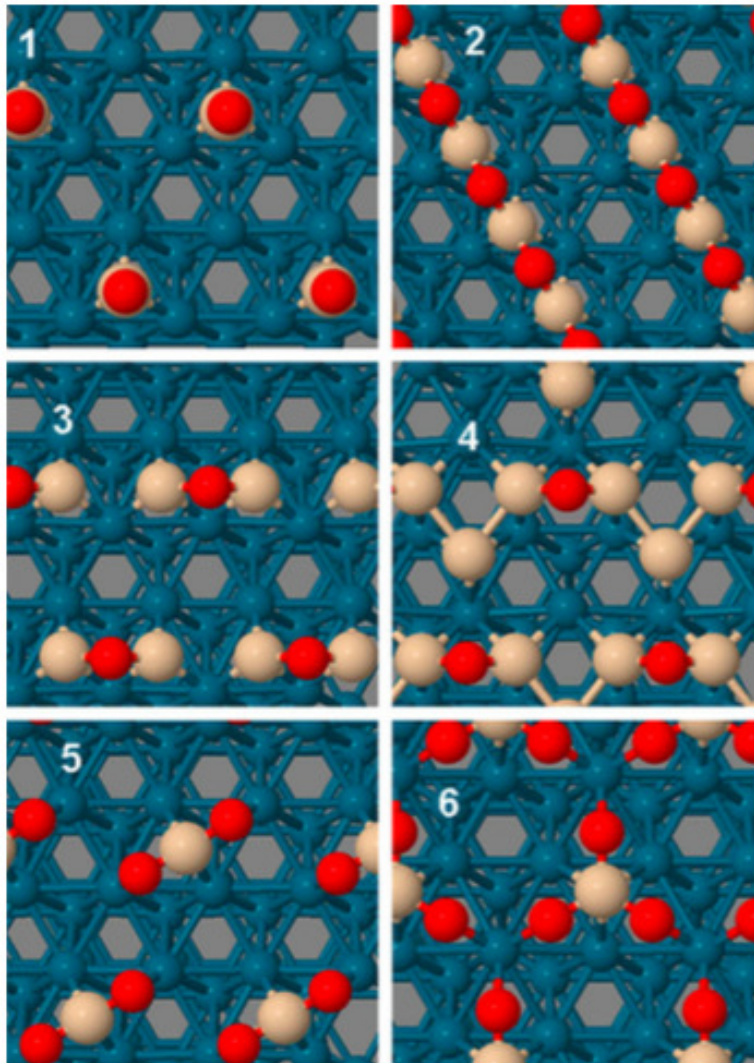
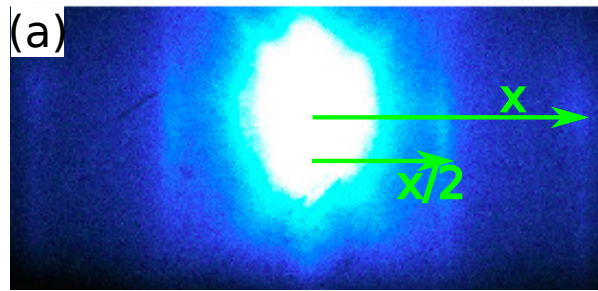


Figure 4.5: (a) RHEED pattern obtained from Si deposited  $(2 \times 2) - 30$  surface. (1-6) models of oxygen (red) and silicon (yellow) forming a  $(2 \times 2)$  structure on the Pd(111) surface are shown, adapted from [48].



---

## 4.4 Crystallisation leading to silicon oxide

---

We started our experiments with growing very low coverage of monolayer silicon oxide. To perform this, very low amount of silicon was evaporated on the surface, following which the sample is annealed to  $850^{\circ}\text{C}$  under an oxygen back pressure of  $3 \times 10^{-6}$  mbar (to compensate the O desorption, which is substantial at  $850^{\circ}\text{C}$  [117]) and then cooled down at the rate of  $\sim 10^{\circ}\text{C} / \text{min}$ . The very low coverage could not be studied *via* RHEED, but STM image of a small patch composed in honeycomb lattice was recorded, shown in Figure 4.6. It was established that the monolayer silicon oxide nucleates at the step edges of the Ru(0001) substrates, similar to the previous observations made earlier by Romdhane *et al.* [6] and Klemm *et al.* [52]. The major presence of arm-chair edges provided hints to the formation of the monolayer, and its understanding was our next resort.

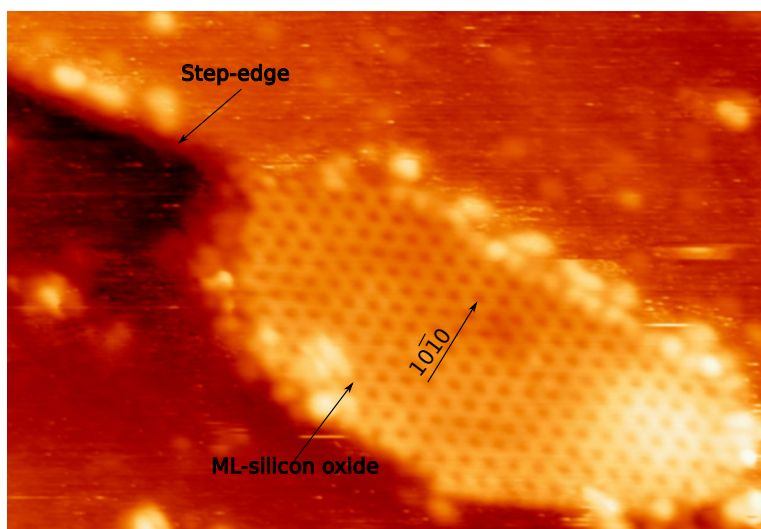


Figure 4.6: STM image ( $11 \times 17$  nm) taken at 1 V and 0.5 nA of a monolayer silicon oxide patch growing at a step edge of Ru(0001). Image courtesy: Sergio Vlaic.

We repeated the experiments with complete monolayer coverage, where a transformation of the silicon and oxygen species into an ordered phase displaying a roughly twice larger lattice parameter than Ru(0001) was observed, as apparent from the RHEED pattern shown in Figure 4.7 (a). STM reveals, indeed, the same honeycomb

---

lattice of silicon oxide (see Figure 3.1 (a) of Chapter 3). The evolution of the RHEED pattern was monitored with a sub-second time resolution to study the lattice dynamics during annealing and cool down. Between 30 seconds to 150 seconds the temperature of the sample increases from room temperature to 850° C. Then it is stable until 900 seconds, and finally the temperature is decreased after 900 seconds. The frames extracted from the movie were used to extract information regarding the positions of the streaks and their widths. For each frame the intensity profiles corresponding to the specular reflection, silicon oxide streaks and the Ru streaks were extracted using a python code (see Chapter 2). Fitting gaussian peaks to the intensity profiles provided with information regarding the position of the streaks and their full-width at half maxima (FWHM) which are later used to determine details about the structure. The intensity profile with gaussian fits to the silicon oxide streaks from specific frames are shown in Figure 4.7 (e-j). Most obvious is (i) the increased uncertainty associated to the data at 170 seconds, which translates to the lower statistics (lower intensity) at this stage of the process, and (ii) the increased width of the streak at this stage. The intensity corresponding to the silicon oxide and the specular reflection streaks between 200 seconds and 550 seconds are shown stacked in waterfall plots together with contour plots in Figure 4.7 (b-d). The higher intensities are coded by the shade of green colour, with dark green corresponding to highest intensity. It is noteworthy that the intensity distribution in the silicon oxide streak (Figure 4.7 (b) & (d)), is characterised by anisotropic contours indicative of that the streaks shift toward the specular streak as time increases. Like the specular streak, the Ru(0001) streaks also do not move with time.

In Figure 4.8 (a), the absolute position of the streak, as deduced from gaussian fits at each time, is shown. During the initial 300 seconds the streak shows dramatic dynamics. While a strong variation of the streak position is observed between 100 and 200 seconds due to the very weak intensity of the reconstruction/silicon oxide streak, which renders the gaussian fits difficult, a steady decrease of the position is observed from 200 seconds. This decrease is first rapid, then much slower. We note that the final position of the streak is slightly, but significantly, distinct from that corresponding to the

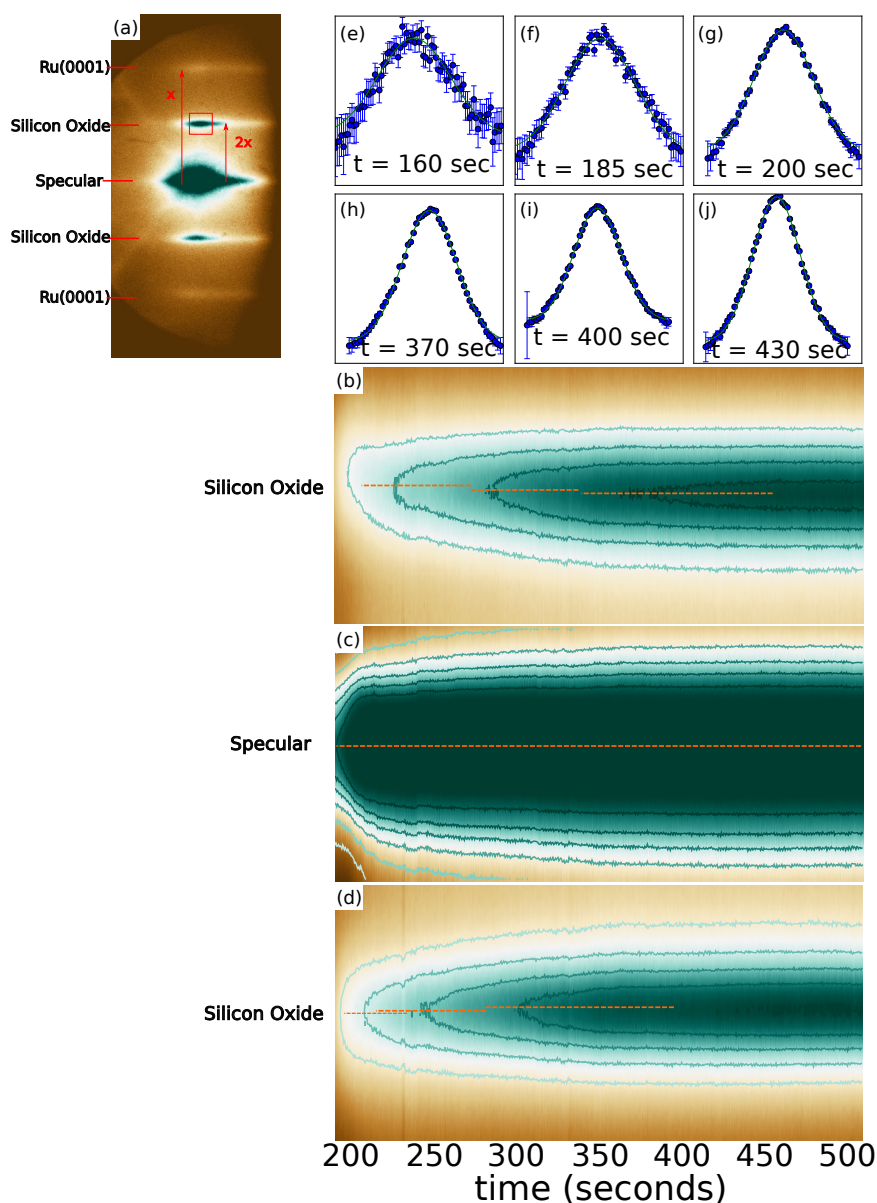


Figure 4.7: (a) RHEED pattern obtained (at 10 keV) from the monolayer silicon oxide grown on Ru(0001). From the white square marked, the intensity was extracted and summed up horizontally and then stacked as a function of time. The corresponding stack for top and bottom reconstruction streaks is shown in (b) and (d) respectively together with the stack for the specular streak in (c). The dotted orange lines are guides for the eyes to highlight the position of the maximum intensity, at a few given times. The sample temperature during the time interval of 200 - 550 seconds was 850° C. (e-j) Gaussian fits to the intensity profile at different times during the experiment.

reconstruction pattern prior to annealing. The absolute distance between the specularly reflected beam and the Ru(0001) streaks remains constant in the experiment. This implies that the measurement does not detect the  $0.01 \text{ \AA}$  variation of the lattice parameter of Ru(0001) corresponding to thermal expansion [3], which informs on the sensitivity of the technique. The absolute distance between the specularly reflected streak and the silicon oxide streak can be translated into the lattice parameter,  $a_{\text{SiO}}$ . Starting from the value of  $5.4 \text{ \AA}$  from the silicon covered  $(2 \times 2) - 3\text{O}/\text{Ru}(0001)$ , silicon oxide exhibits a  $5.3 \pm 0.02 \text{ \AA}$  lattice parameter at the end of the recrystallisation process. This value corresponds to a  $1.8 \pm 0.4 \%$  smaller lattice parameter than that of the  $(2 \times 2) - 3\text{O}$ . Strikingly as well, the lattice parameter reduces to very small values, as low as  $4.9 \pm 0.05 \text{ \AA}$  at 200 seconds, which corresponds to a  $9 \pm 1\%$  decrease of the lattice parameter compared to  $(2 \times 2) - 3\text{O}$ .

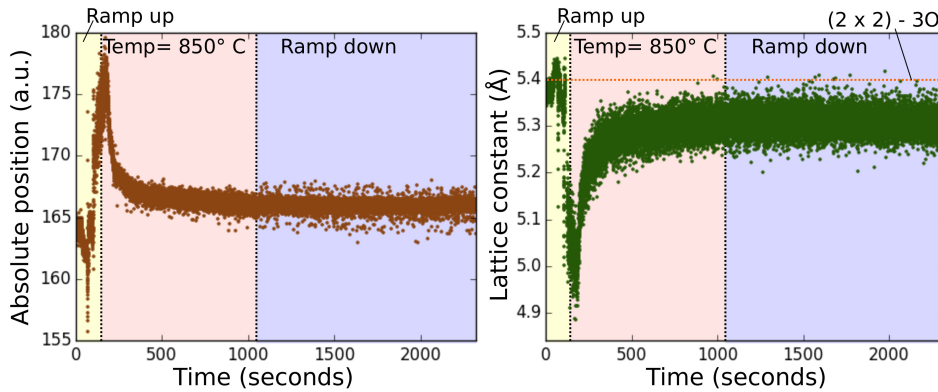


Figure 4.8: (a) Absolute position of the reconstruction streak in reference to specular streak extracted from gaussian fits and (b) the corresponding lattice parameter of monolayer silicon oxide as a function of time.

In Figure 4.9 a, the evolution of the FWHM of the silicon oxide streak is shown. After the first rapid erratic increase associated to the low intensity, broad streaks between 100 and 200 seconds, the FWHM decreases, first rapidly and then slowly, and stabilises at a value about 15% larger than for the  $(2 \times 2) - 3\text{O}$  reconstruction. Diffraction with high energy electrons does not allow for straightforward quantitative analysis of the FWHM along a simple kinematic diffraction framework.

---

Yet for the purpose of a qualitative analysis only we will now use this framework. In this framework, the broadening of the streaks can be due to either finite size ( $\tau$ ) effects, or the presence of a distribution of lattice parameter (a strain field) or both. In the first case, the finite size of the fully coherent crystalline domains sets a FWHM ( $\beta$ ) obeying Scherrer's formula [82] given as

$$\beta = k\lambda/\tau\cos\theta \quad (4.1)$$

here  $\tau$  is the crystallite size,  $k$  is shape factor which we assume equal to 1 for simplicity,  $\lambda$  is the wavelength of the electrons,  $\beta$  is the FWHM and  $\theta$  is the Bragg angle.

The evolution of  $\tau$  with time is shown in Figure 4.9 (b). We note that the obtained values stay below the coherence length ( $L_c$ ) of the electron beam,  $L_c = 10$  nm. (see discussion in chapter 2).

Figure 4.9 (b) suggests that the domain size of the silicon oxide single crystalline domains is smaller than that of the single crystal  $(2 \times 2) - 3O$  domains, which is constant with the STM observation (Figure 4.10), and will be discussed more into details later. The evolution of the domain size is also consistent with a crystallisation process, along which small silicon oxide grains crystallise and grow in size. The second possible source of broadening is the presence of a strain field ( $\Delta a_{SiO}$ ) about a mean lattice parameter value  $a_{SiO}$ , which would yield a FWHM equal to  $\Delta a_{SiO}/a_{SiO}$ . In this scenario a 2% strain field would exist after silicon oxide crystallisation, while a large, almost 10% strain field would be present in silicon oxide at the initial stages of crystallisation (Figure 4.9 (b)).

We now turn to the possible origin of a global lattice parameter in silicon oxide being smaller than that of the  $(2 \times 2) - 3O$  reconstruction, *i.e.* smaller than twice the Ru(0001) lattice parameter. Assuming that monolayer silicon oxide would be stretched if in a  $(2 \times 2)$  commensurate configuration with respect to the Ru(0001), the measured lattice parameters would point to the existence of misfit dislocations (Figure 4.11) typically one every 80 silicon oxide unit cells.

Another possible situation is linked to the role of edges. To account for the smaller lattice parameter than for the  $(2 \times 2) - 3O$  reconstruc-

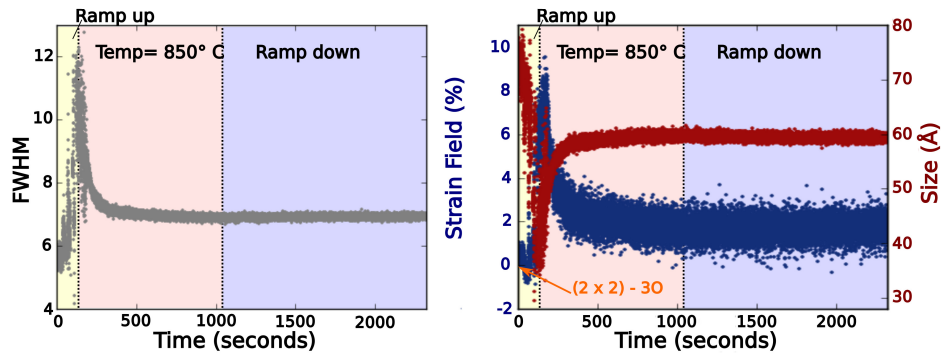


Figure 4.9: (a) FWHM of the silicon oxide streak extracted from gaussian fits and (b) corresponding strain field and domain size as function of time at different temperature. The orange arrow marks the strain field (0%) expected in the  $(2 \times 2) - 30$  domains.

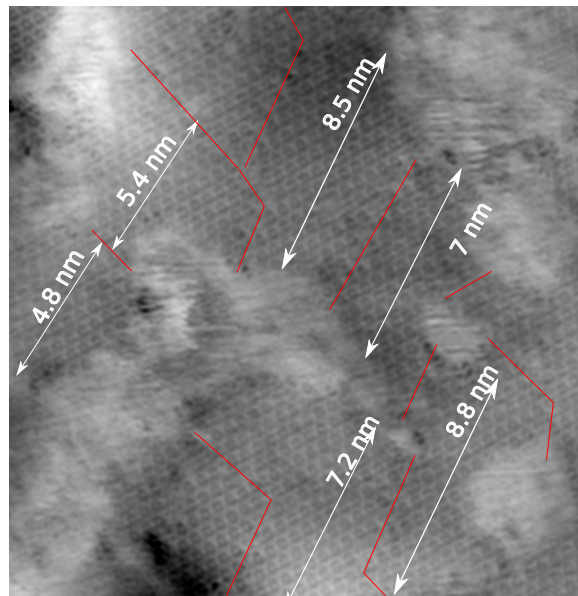


Figure 4.10: STM image ( $20 \text{ nm} \times 20 \text{ nm}$ ) taken at  $0.9 \text{ V}$  and  $2 \text{ nA}$ . The domain boundaries are marked in red lines. The yellow dotted line marks the lateral shift between two domains. The lateral extension of the domains is depicted.

---

tion, one has to assume that silicon oxide would tend to adopt a  $(2 \times 2)$  commensurability on Ru(0001), and under-coordinated edge atoms would tend to form shorter bonds with their neighbour Si or O atoms (Figure 4.11). Alternatively, grain boundaries composed of non-hexagonal silicon oxide rings (see discussion in the previous chapter) could have a similar effect. They could also be responsible for strain fields, whose extend would be all the more important as the size of the single crystal domains would be smaller.

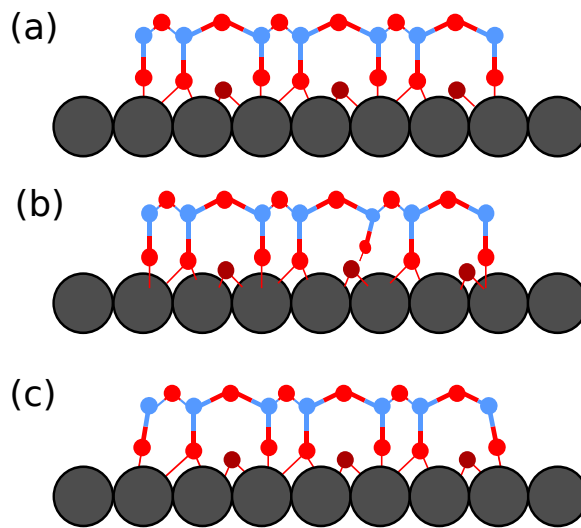


Figure 4.11: Models of monolayer silicon oxide with strain. (a) DFT relaxed model (of an infinite two-dimensional monolayer silicon oxide), (b) misfit dislocation in the monolayer silicon oxide, (c) Lattice distortion induced at the edges of the silicon oxide domain.

We note that more complex processes for accommodating heteroepitaxial stress between Ru and silicon oxide could be relevant as well, for instance distortion of the hexagons of silicon oxide, which was predicted by DFT calculations [7] [2] (Figure 4.12).

## 4.5 Optimisation of the domain size

---

It is interesting to note that the size of the single crystal domain monolayer silicon oxide,  $\sim 7$  nm, is comparable to the size of the domains of the  $(2 \times 2) - 3O$  reconstruction. In both cases the domains



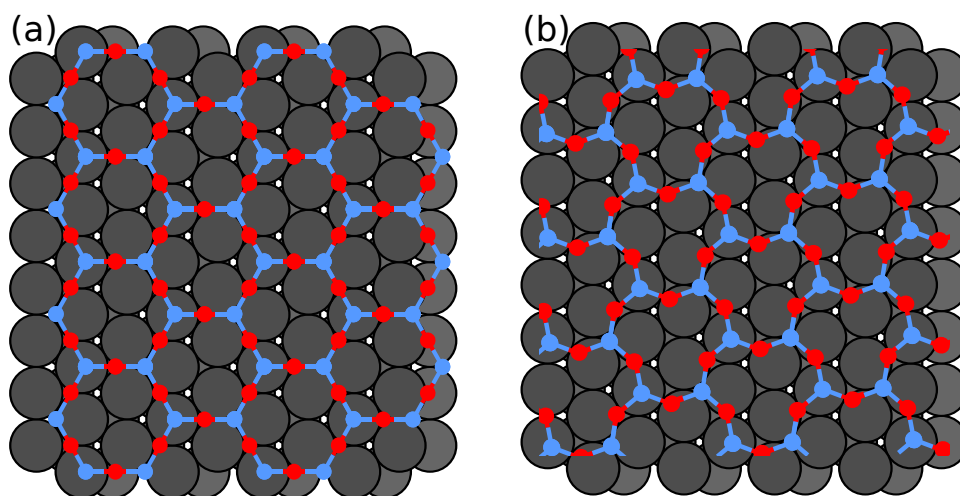


Figure 4.12: (a) Monolayer silicon oxide on Ru(0001). (b) Monolayer silicon oxide on Ru(0001) with rotated [SiO<sub>4</sub>] tetrahedra due to compression as predicted in [7] [2].

are anti phase. The natural prolongation of the work was to try to increase the monolayer domain size of silicon oxide, , which we attempted by tuning the size of domains of the precursor oxygen reconstructed metal support.

The oxygen adsorption on Ru(0001) is highly dependent on the surface temperature due to the varying surface mobility and desorption rate of oxygen atoms [117], as also seen in the section 4.2. Understanding this, the Ru(0001) surface held at 350° C (instead of room temperature; see RHEED analysis discussed in section 4.2 and Figure 4.3) was exposed to  $1 \times 10^{-8}$  mbar of oxygen for 5 min and then the oxygen back pressure was increased to  $3 \times 10^{-6}$  mbar. Due to high desorption at higher temperatures, lower nucleation of the rotated domains of the  $(2 \times 1)$  reconstruction occurred which led to large domains, revealed by STM (Figure 4.13 (a)), with extension more than 100 nm. Since the desorption rate is high at this temperature, the domains were found to exhibit vacancies. The high density of vacancies could be seen in the STM image. During the second step, these large domains were seen to convert into large domains of  $(2 \times 2) - 3O$  reconstruction (Figure 4.13 (b)).

This surface containing large domains of  $(2 \times 2) - 3O$  was then converted into monolayer silicon oxide by following the previously de-



---

scribed steps of the growth protocol. However, no noticeable change in the domain size could be observed indicating that the recrystallisation of the silicon oxide itself imposes the formation of domains, which is presumably driven by kinetic parameters, that we have not tried to control yet. One of these parameters could be the rate of increase of temperature leading to crystallisation. We note that in addition, thermodynamics could be relevant as well, and that, for instance, the formation of defects such as grain boundaries could help stabilising the system.

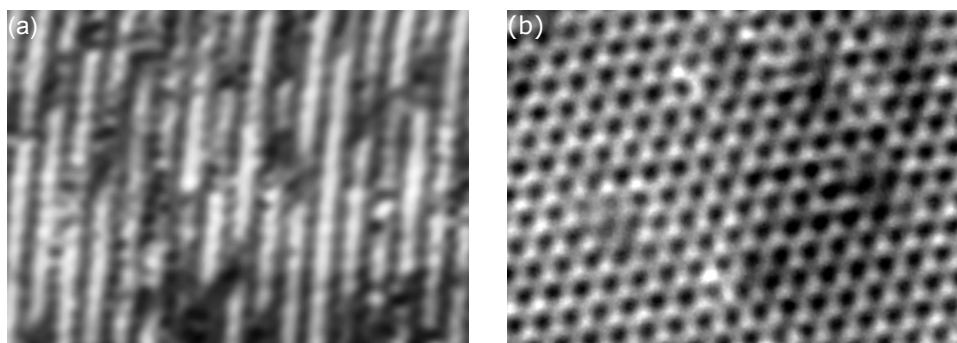


Figure 4.13: STM images for oxygen reconstruction grown at 350° C. (a)  $(2 \times 1)$  (1.2V, 1.4nA) and (b)  $(2 \times 2) - 3O$  (2V, 2nA).

## 4.6 Tentative Mechanism of monolayer silicon oxide formation

---

A recrystallisation mechanism of monolayer silicon oxide formation comprising in geometrical displacements of the surface species is proposed. It is based on the four critical observations made in this thesis:

1. Coexistence of the monolayer silicon oxide with a  $(2 \times 2)$  oxygen reconstruction on Ru(0001) (see previous chapter)
2. Partial preservation of the atomic order upon silicon deposition on the  $(2 \times 2) - 3O$  reconstructed surface of Ru(0001) (as seen in RHEED in section 4.3)

- 
3. Limited size of the monolayer silicon oxide domains, smaller than that of  $(2 \times 2) - 3\text{O}$  reconstruction
  4. Formation of anti-phase domain boundaries

This mechanism considers that the oxygen atoms from the precursor  $(2 \times 2) - 3\text{O}$  reconstruction act as a bridge between the monolayer and the Ru(0001) surface. This would leave also 33% extra O atoms available for completing the assembly of silicon oxide. Since the oxygen atoms exclusively occupy hcp-hollow sites in the  $(2 \times 2) - 3\text{O}$  reconstruction while the monolayer binds in fcc-hollow and top sites, this mechanism suggests a translation of the surface oxygen atoms. This translation requires a short displacement of two of the three sub lattices of the  $(2 \times 2) - 3\text{O}$  reconstruction: A first sub lattice moves from hcp-hollow to fcc-hollow sites, while second sub lattice moves from hcp-hollow to top sites, as shown in Figure 4.14 (a-c). The third sub lattice does not move. The transformation occurs with a mixed order-disordered phase leading to a crystalline monolayer silicon oxide, upon annealing to  $850^\circ \text{C}$ . This translative recrystallisation is expected to occur with small global shifts of part of the oxygen lattice. In this case, the transformation is three-fold degenerate since it can occur in three-equivalent,  $120^\circ$  rotated,  $\langle 1\bar{1}00 \rangle$  directions of Ru(0001), or zigzag direction of the monolayer (seen in blue, green and yellow colours in Figure 4.14). The over-lapping of these coloured lattices shown in Figure 4.14 (d) depicts the degeneracy in a clear manner, as the hexagons do not match and are instead mutually shifted. Thus, these coloured lattices would in experiment result in the anti phase domain formation, observed in the STM imaging.

It is striking to note, in Figure 4.14, that the hexagons of the monolayer form around the oxygen atoms belonging to the third sub lattice that does not move. These oxygen atoms may correspond to those which were imaged in the STM experiments to coexist with the monolayer silicon oxide, discussed in the previous chapter. The presence of this extra oxygen has been argued to stabilise the monolayer silicon oxide, although marginally ( $< 0.1\%$ ). Thus the absence of this extra oxygen would not hinder the formation of monolayer silicon oxide. We rather expect that the observation of these oxygen atoms

---

is a signature of the history of the process, and is a remainder of the initial  $(2 \times 2) - 3O$  reconstruction.

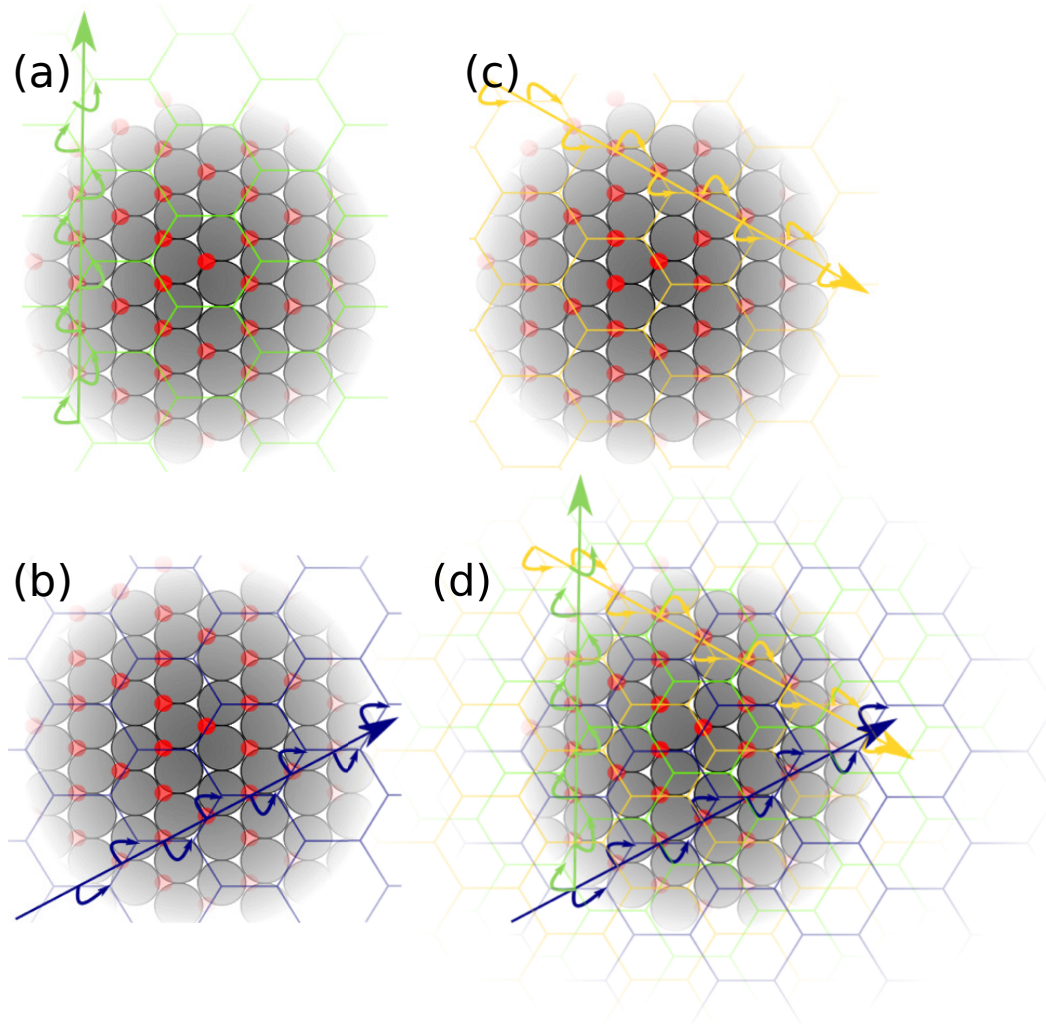


Figure 4.14: (a-c) Translative recrystallisation mechanism of the formation of monolayer silicon oxide in three direction leads to formation of anti phase domains whose mutual shifts are evident by overlapping the three kinds of domains (d).

## 4.7 Conclusions

---

In this chapter, insights in the formation of the monolayer silicon oxide were presented. The inheritance of the structure of mono-

---

layer from the precursor  $(2 \times 2) - 3O$  reconstruction was understood through the continuous observation of RHEED pattern during the growth process. The *in operando* studies unravelled a crystallisation of the surface and provide real-time access to strain in the monolayer during crystallisation at fixed temperature. These strains can be considerable, reaching almost 10% at the beginning of the crystallisation process and decreasing to 1% at the end, and are expected to arise from the finite size of the small silicon oxide domains due to strong fraction of edges (or boundaries) and/or from misfit dislocations in the silicon oxide. The size of the monolayer domain is argued to be limited by the displacive recrystallisation mechanism which is consistent with various observations.

# Chapter 5

## Conclusions

In this thesis we studied the two-dimensional silicon oxide grown on Ru(0001) surface. This two-dimensional silicon oxide is proposed as an ultra thin dielectric material and also is a model system for catalysts, mimicking the atomic structure of the inner walls of mesoporous catalysts. As we discussed, both of its phases: bilayer and monolayer, have well defined structures that can be readily accessed by surface science techniques like scanning tunnelling microscopy (STM) and electron diffraction (LEED and RHEED). In the first part we discussed on the aspects of the structure of the bilayer and monolayer silicon oxide and showed their selective formation on different metals. It was shown that the bilayer is weakly interacting with the substrate while the monolayer is covalently bonded. Since the resolution of the atomic structure of two-dimensional silicon oxide was limited according to the experimental techniques, studies so far relied heavily on density functional theory (DFT) calculations. The structure of the monolayer phase in particular, was so far discussed in the light of a limited set of experimental results. The literature lacks any information on the formation of defects, both in monolayer and bilayer. These defects often accompany strain fields, as shown in the bilayer but reports corresponding to propagation of such strain fields were missing for the case of monolayer.

During this thesis, we demonstrated direct imaging of the monolayer silicon oxide on Ru(0001) down to unprecedented atomic resolution by room temperature high-resolution scanning tunnelling microscopy. In this atomic structure the monolayer was resolved to

---

comprise in hexagonal arrangement of  $[\text{SiO}_4]$  tetrahedra, all of them pointing towards Ru(0001) support. In the STM study, we presented the structure with chemical sensitivity, according to which the monolayer binds in two kinds of sites on the Ru(0001). The precise nature of bonding was rationalised in the vicinity of the silicon deficient regions which comprise in  $(2 \times 2) - 3\text{O}$  reconstruction. These different (two) occupation sites correspond to two sub-lattices in the monolayer which imposes a degeneracy leading to formation of anti phase domains (APDs). These APDs were revealed to stitch together by one-dimensional line defects composed of pentagon-heptagon pairs. The monolayer hexagons were revealed to coexist with a  $(2 \times 2) - \text{O}$  reconstruction, the presence of which was, so far, debated and was argued to provide higher stability to the monolayer (by  $< 1\%$ ) by DFT calculations. Our theoretical calculations performed to calculate the partial electron density maps (PEDMs) from the surface of monolayer silicon oxide on Ru(0001) depicted a perfect match with the STM images further corroborating the obtained results.

The next goal was to understand the formation mechanism of monolayer silicon oxide. The continuous RHEED monitoring suggested that the monolayer inherits the reconstruction from the  $(2 \times 2) - 3\text{O}$  surface. Upon annealing under oxygen back pressure, the silicon containing oxygen pre-covered surface was shown to undergo a crystallisation process by means of *in operando* RHEED, leading to monolayer silicon oxide. This crystallisation is accompanied by development of considerable strains in the monolayer, up to  $\sim 10\%$  during initial phase and  $\sim 1\%$  at the end, during the growth. The finite size of the small domain with large amount of edges or misfit dislocations are the two possible origins of the strains observed. Correspondingly, we demonstrate that the domain size of the monolayer silicon oxide is limited by a translative recrystallisation mechanism which is rationale with other observations.

---

## Perspectives

---

### Phase transformation

Upon external stimulation, like a charge transfer from an alkali atom, transition metal di-chalcogenides are known to undergo reversible structural transformation from 2H phase  $\rightarrow$  1T phase. This phase transformation is accompanied by alteration in the electronic properties, which transform from metallic to semiconducting, and *vice versa*. During our experiments, the monolayer silicon oxide was observed as well to undergo a phase transformation upon vacuum annealing. In this transformation, the monolayer forms a  $30^\circ$  rotated phase with respect to the Ru(0001) support. In the literature, this transformation is very little discussed. The rotated phase is suggested to be stabilised with the formation of defects [119] (as discussed in section 1.3.4). Supporting the preliminary RHEED results that we obtained on this rotated phase, a detailed *in operando* study of the phase transformation will be performed with diffraction (RHEED) and direct imaging (Low Energy Electron Microscopy). A dedicated STM study will then be conducted to analyse the defects formed due to the phase transformation.

### Electronic Properties

The bulk crystalline phases of silicon oxide are known for their insulating nature with an electronic band gap of 8 eV. Having optimised their growth, we now plan to turn to the study of the electronic properties of monolayer and bilayer silicon oxide. The work function measurements can be performed with LEEM, or with the Kelvin probe mode of an atomic force microscope. The two-dimensional silicon oxide phases will also be studied by angle resolved photoelectron spectroscopy (ARPES) through which the information regarding the electronic band structure can be attained. We expect to be able to identify the nature of the orbitals involved at the interface between monolayer silicon oxide and Ru(0001), and to demonstrate the possibility to electronically dope silicon oxide.

---

## **Heterostructures**

The system of bilayer silicon oxide on top of graphene that was grown accidentally in [42] and intercalation of silicon oxide between graphene and Ru(0001) [65] are examples of vertical heterostructure. We intend to perform studies relating to optimising the two kinds of junctions. The growth would be performed in UHV and monitored by diffraction, LEEM and STM imaging. Under these conditions, heterostructure with atomically clean interfaces may be formed. The intercalation mechanism can efficiently decouple the graphene sheet from its metallic substrate without the need for transfer using strong etchants which can induce defects in graphene. We need to generate different levels of doping and decoupling with respect to the substrate in graphene.

## **Route to two-dimensional silicon carbide**

The only reports of growth of low-dimensional silicon carbide in a honeycomb lattice were obtained from a reaction between carbon nanotube and silicon oxide vapours [101]. At the interface between the nanotubes and silicon oxide layers, researchers suspected formation of a  $sp^2$  hybridised silicon carbide, through electron energy loss spectroscopy. We plan to perform a similar experiment with the monolayer silicon oxide and carbon species either segregating out of the bulk of the metal substrate or already present in form of graphene.



# Bibliography

- [1] Takashi Aizawa, Shigeru Suehara, and Shigeki Otani. Silicene on zirconium carbide (111). *The Journal of Physical Chemistry C*, 118(40):23049–23057, 2014.
- [2] Eric I Altman, Jan Götzen, Niveditha Samudrala, and Udo D Schwarz. Growth and Characterization of Crystalline Silica Films on Pd (100). *The Journal of Physical Chemistry C*, 117(49):26144–26155, 2013.
- [3] John W Arblaster. Crystallographic properties of ruthenium. *Platinum Metals Review*, 57(2):127–136, 2013.
- [4] Sukang Bae, Hyeongkeun Kim, Youngbin Lee, Xiangfan Xu, Jae-Sung Park, Yi Zheng, Jayakumar Balakrishnan, Tian Lei, Hye Ri Kim, Young Il Song, et al. Roll-to-roll production of 30-inch graphene films for transparent electrodes. *Nature Nanotechnology*, 5(8):574–578, 2010.
- [5] Mario Norberto Baibich, Jean Marc Broto, Albert Fert, F Nguyen Van Dau, Frédéric Petroff, P Etienne, G Creuzet, A Friederich, and J Chazelas. Giant magnetoresistance of (001) Fe/(001) Cr magnetic superlattices. *Physical Review Letters*, 61(21):2472, 1988.
- [6] Ferdaous Ben Romdhane, Torbjörn Björkman, Arkady V Krasheninnikov, and Florian Banhart. Solid-state growth of one- and two-dimensional silica structures on metal surfaces. *The Journal of Physical Chemistry C*, 118(36):21001–21005, 2014.

- 
- [7] Ferdaous Ben Romdhane, Torbjörn Björkman, Julio A Rodríguez-Manzo, Ovidiu Cretu, Arkady V Krasheninnikov, and Florian Banhart. In situ growth of cellular two-dimensional silicon oxide on metal substrates. *ACS Nano*, 7(6):5175–5180, 2013.
- [8] J Bernhardt, J Schardt, U Starke, and K Heinz. Epitaxially ideal oxide–semiconductor interfaces: silicate adlayers on hexagonal (0001) and (000 $\bar{1}$ ) SiC surfaces. *Applied Physics Letters*, 74(8):1084–1086, 1999.
- [9] Flemming Besenbacher. Scanning tunnelling microscopy studies of metal surfaces. *Reports on Progress in Physics*, 59(12):1737, 1996.
- [10] Torbjörn Björkman, Simon Kurasch, Ossi Lehtinen, Jani Kotakoski, Oleg V Yazyev, Anchal Srivastava, Viera Skakalova, Jurgen H Smet, Ute Kaiser, and Arkady V Krasheninnikov. Defects in bilayer silica and graphene: common trends in diverse hexagonal two-dimensional systems. *Scientific Reports*, 3, 2013.
- [11] Nils Blanc, Fabien Jean, Arkady V Krasheninnikov, Gilles Renaud, and Johann Coraux. Strains induced by point defects in graphene on a metal. *Physical Review Letters*, 111(8):085501, 2013.
- [12] M Boudart. Catalysis by supported metals. *Adv. Catal*, 20:153–166, 1969.
- [13] Christin Büchner, Leonid Lichtenstein, Stefanie Stuckenholz, Markus Heyde, Franziska Ringleb, Martin Sterrer, William E Kaden, Livia Giordano, Gianfranco Pacchioni, and Hans-Joachim Freund. Adsorption of Au and Pd on Ruthenium-Supported Bilayer Silica. *The Journal of Physical Chemistry C*, 118(36):20959–20969, 2014.
- [14] Christin Büchner, Leonid Lichtenstein, Xin Yu, J Anibal Boscoboinik, Bing Yang, William E Kaden, Markus Heyde, Shamil K Shaikhutdinov, Radosław Włodarczyk, Marek Sierka,

- 
- et al. Ultrathin silica films: The atomic structure of two-dimensional crystals and glasses. *Chemistry—A European Journal*, 20(30):9176–9183, 2014.
- [15] Li-Wu Chang, Marin Alexe, James F Scott, and J Marty Gregg. Settling the "dead layer" debate in nanoscale capacitors. *Advanced Materials*, 21(48):4911–4914, 2009.
- [16] M. S. Chen, A. K. Santra, and D. W. Goodman. Structure of thin SiO<sub>2</sub> films grown on Mo(112). *Physical Review B - Condensed Matter and Materials Physics*, 69:1–7, April 2004.
- [17] Manish Chhowalla, Hyeon Suk Shin, Goki Eda, Lain-Jong Li, Kian Ping Loh, and Hua Zhang. The chemistry of two-dimensional layered transition metal dichalcogenide nanosheets. *Nature Chemistry*, 5(4):263–275, 2013.
- [18] Daniele Chiappe, Emilio Scalise, Eugenio Cinquanta, Carlo Grazianetti, Bas van den Broek, Marco Fanciulli, Michel Houssa, and Alessandro Molle. Two-Dimensional Si Nanosheets with Local Hexagonal Structure on a MoS<sub>2</sub> Surface. *Advanced Materials*, 26(13):2096–2101, 2014.
- [19] Eric Cockayne, Gregory M Rutter, Nathan P Guisinger, Jason N Crain, Phillip N First, and Joseph A Stroscio. Grain boundary loops in graphene. *Physical Review B*, 83(19):195425, 2011.
- [20] Johann Coraux, Alpha T N'Diaye, Carsten Busse, and Thomas Michely. Structural coherency of graphene on Ir (111). *Nano Letters*, 8(2):565–570, 2008.
- [21] Johann Coraux, Tim N Plasa, Carsten Busse, Thomas Michely, et al. Structure of epitaxial graphene on Ir (111). *New Journal of Physics*, 10(4):043033, 2008.
- [22] CJ Dawson, MAB Pope, M O'Keeffe, and MMJ Treacy. Low-density, low-energy, zeolites assembled from double-layer silica sheets. *Chemistry of Materials*, 25(19):3816–3821, 2013.
- [23] Walt A De Heer, Claire Berger, Xiaosong Wu, Phillip N First, Edward H Conrad, Xuebin Li, Tianbo Li, Michael Sprinkle,
-

- 
- Joanna Hass, Marcin L Sadowski, et al. Epitaxial graphene. *Solid State Communications*, 143(1):92–100, 2007.
- [24] AL Vázquez de Parga, OS Hernán, R Miranda, A Levy Yeyati, N Mingo, A Martin-Rodero, and F Flores. Electron resonances in sharp tips and their role in tunneling spectroscopy. *Physical Review Letters*, 80(2):357, 1998.
- [25] Cory R Dean, Andrea F Young, Inanc Meric, Chris Lee, Lei Wang, S Sorgenfrei, K Watanabe, T Taniguchi, P Kim, KL Shepard, et al. Boron nitride substrates for high-quality graphene electronics. *Nature Nanotechnology*, 5(10):722–726, 2010.
- [26] JA Duffy. Chemical bonding in the oxides of the elements: A new appraisal. *Journal of Solid State Chemistry*, 62(2):145–157, 1986.
- [27] Goki Eda, Takeshi Fujita, Hisato Yamaguchi, Damien Voiry, Mingwei Chen, and Manish Chhowalla. Coherent atomic and electronic heterostructures of single-layer MoS<sub>2</sub>. *Acs Nano*, 6(8):7311–7317, 2012.
- [28] Goki Eda, Hisato Yamaguchi, Damien Voiry, Takeshi Fujita, Mingwei Chen, and Manish Chhowalla. Photoluminescence from chemically exfoliated MoS<sub>2</sub>. *Nano Letters*, 11(12):5111–5116, 2011.
- [29] Nicola Ferralis, Roya Maboudian, and Carlo Carraro. Evidence of structural strain in epitaxial graphene layers on 6H-SiC (0001). *Physical Review Letters*, 101(15):156801, 2008.
- [30] Antoine Fleurence, Rainer Friedlein, Taisuke Ozaki, Hiroyuki Kawai, Ying Wang, and Yukiko Yamada-Takamura. Experimental evidence for epitaxial silicene on diboride thin films. *Physical Review Letters*, 108(24):245501, 2012.
- [31] C Franchini, R Podloucky, F Allegretti, F Li, G Parteder, S Surnev, and FP Netzer. Structural and vibrational properties of two-dimensional Mn<sub>x</sub>O<sub>y</sub> layers on Pd (100): Experiments and density functional theory calculations. *Physical Review B*, 79(3):035420, 2009.

- 
- [32] C Franchini, J Zabloucil, R Podloucky, F Allegretti, F Li, S Surnev, and FP Netzer. Interplay between magnetic, electronic and vibrational effects in monolayer  $\text{Mn}_3\text{O}_4$  grown on Pd (100). *arXiv preprint arXiv:0902.1953*, 2009.
- [33] Hans-Joachim Freund and Gianfranco Pacchioni. Oxide ultra-thin films on metals: new materials for the design of supported metal catalysts. *Chemical Society Reviews*, 37(10):2224–2242, 2008.
- [34] Christoph Freysoldt, Patrick Rinke, and Matthias Scheffler. Structural and electronic heterogeneity of two dimensional amorphous silica layers. *Advanced Materials Interfaces*, 1(7), 2014.
- [35] Andre K Geim and Irina V Grigorieva. Van der waals heterostructures. *Nature*, 499(7459):419–425, 2013.
- [36] Livia Giordano, Davide Ricci, Gianfranco Pacchioni, and Piero Ugliengo. Structure and vibrational spectra of crystalline  $\text{SiO}_2$  ultra-thin films on Mo(112). *Surface Science*, 584(2):225–236, 2005.
- [37] Leo Gross, Nikolaj Moll, Fabian Mohn, Alessandro Curioni, Gerhard Meyer, Felix Hanke, and Mats Persson. High-resolution molecular orbital imaging using a p-wave STM tip. *Physical Review Letters*, 107(8):086101, 2011.
- [38] M Gsell, P Jakob, and D Menzel. Effect of substrate strain on adsorption. *Science*, 280(5364):717–720, 1998.
- [39] H Hakan Gürel, V Ongun Özçelik, and S Ciraci. Effects of charging and perpendicular electric field on the properties of silicene and germanene. *Journal of Physics: Condensed Matter*, 25(30):305007, 2013.
- [40] Jasmine Hargrove, HB Mihiri Shashikala, Lauren Guerrido, Natarajan Ravi, and Xiao-Qian Wang. Band gap opening in methane intercalated graphene. *Nanoscale*, 4(15):4443–4446, 2012.

- 
- [41] Pinshane Y Huang, Simon Kurasch, Jonathan S Alden, Ashivni Shekhawat, Alexander A Alemi, Paul L McEuen, James P Sethna, Ute Kaiser, and David A Muller. Imaging atomic rearrangements in two-dimensional silica glass: Watching silica's dance. *Science*, 342(6155):224–227, 2013.
- [42] Pinshane Y Huang, Simon Kurasch, Anchal Srivastava, Viera Skakalova, Jani Kotakoski, Arkady V Krasheninnikov, Robert Hovden, Qingyun Mao, Jannik C Meyer, Jurgen Smet, et al. Direct imaging of a two-dimensional silica glass on graphene. *Nano Letters*, 12(2):1081–1086, 2012.
- [43] Sumio Iijima et al. Helical microtubules of graphitic carbon. *Nature*, 354(6348):56–58, 1991.
- [44] P Jakob, M Gsell, and D Menzel. Interactions of adsorbates with locally strained substrate lattices. *The Journal of Chemical Physics*, 114(22):10075–10085, 2001.
- [45] Thaneshwor P Kaloni, YC Cheng, and Udo Schwingenschlögl. Hole doped dirac states in silicene by biaxial tensile strain. *Journal of Applied Physics*, 113(10):104305, 2013.
- [46] Abdelkader Kara, Hanna Enriquez, Ari P Seitsonen, LC Lew Yan Voon, Sébastien Vizzini, Bernard Aufray, and Hamid Oughaddou. A review on silicene—new candidate for electronics. *Surface science reports*, 67(1):1–18, 2012.
- [47] Jakub Kedzierski, Pei-Lan Hsu, Paul Healey, Peter W Wyatt, Craig L Keast, Mike Sprinkle, Claire Berger, and Walt A De Heer. Epitaxial graphene transistors on sic substrates. *Electron Devices, IEEE Transactions on*, 55(8):2078–2085, 2008.
- [48] Dylan C Kershner, Matthew P Hyman, and J Will Medlin. Density functional theory studies of submonolayer oxidized silicon structures on Pd (111) and Pt (111). *Surface Science*, 602(23):3603–3610, 2008.
- [49] Georgy Kichin, Christian Weiss, Christian Wagner, F Stefan Tautz, and Ruslan Temirov. Single molecule and single atom sensors for atomic resolution imaging of chemically

- 
- complex surfaces. *Journal of the American Chemical Society*, 133(42):16847–16851, 2011.
- [50] Amina Kimouche, Olivier Renault, Sayanti Samaddar, Clemens Winkelmann, Hervé Courtois, Olivier Fruchart, and Johann Coraux. Modulating charge density and inelastic optical response in graphene by atmospheric pressure localized intercalation through wrinkles. *Carbon*, 68:73–79, 2014.
- [51] Tetsuhiro Kinoshita and Seigi Mizuno. Surface structure determination of silica single layer on Mo (112) by LEED. *Surface Science*, 605(13):1209–1213, 2011.
- [52] HW Klemm, Gina Peschel, Ewa Madej, Alexander Fuhrich, Martin Timm, Dietrich Menzel, Th Schmidt, and H-J Freund. Preparation of silica films on Ru (0001): A LEEM/PEEM study. *Surface Science*, 643:45–51, 2016.
- [53] G Kresse, S Surnev, MG Ramsey, and FP Netzer. First-principles calculations for V x O y grown on Pd (111). *Surface Science*, 492(3):329–344, 2001.
- [54] H W Kroto, J R Heath, S C O'brien, R F Curl, and R E Smalley. C<sub>60</sub> buckminsterfulleren. *Nature*, 318:162163, 1985.
- [55] Jayeeta Lahiri, You Lin, Pinar Bozkurt, Ivan I Oleynik, and Matthias Batzill. An extended defect in graphene as a metallic wire. *Nature Nanotechnology*, 5(5):326–329, 2010.
- [56] Boubekour Lalmi, Hamid Oughaddou, Hanna Enriquez, Abdelkader Kara, Sébastien Vizzini, Bénédicte Ealet, and Bernard Aufray. Epitaxial growth of a silicene sheet. *Applied Physics Letters*, 97(22):223109, 2010.
- [57] ND Lang. Spectroscopy of single atoms in the scanning tunneling microscope. *Physical Review B*, 34(8):5947, 1986.
- [58] Irving Langmuir. The mechanism of the surface phenomena of flotation. *Transactions of the Faraday Society*, 15(June):62–74, 1920.

- 
- [59] Irving Langmuir. Forces near the surfaces of molecules. *Chemical Reviews*, 6(4):451–479, 1930.
- [60] Xuesong Li, Weiwei Cai, Jinho An, Seyoung Kim, Junghyo Nah, Dongxing Yang, Richard Piner, Aruna Velamakanni, Inhwa Jung, Emanuel Tutuc, et al. Large-area synthesis of high-quality and uniform graphene films on copper foils. *Science*, 324(5932):1312–1314, 2009.
- [61] Xuesong Li, Yanwu Zhu, Weiwei Cai, Mark Borysiak, Boyang Han, David Chen, Richard D Piner, Luigi Colombo, and Rodney S Ruoff. Transfer of large-area graphene films for high-performance transparent conductive electrodes. *Nano Letters*, 9(12):4359–4363, 2009.
- [62] Leonid Lichtenstein. *The structure of two-dimensional vitreous silica*. PhD thesis, Freie Universität Berlin, 2012.
- [63] Leonid Lichtenstein, Markus Heyde, and Hans-Joachim Freund. Atomic arrangement in two-dimensional silica: from crystalline to vitreous structures. *The Journal of Physical Chemistry C*, 116(38):20426–20432, 2012.
- [64] Leonid Lichtenstein, Markus Heyde, and Hans-Joachim Freund. Crystalline-vitreous interface in two dimensional silica. *Physical Review Letters*, 109(10):106101, 2012.
- [65] Silvano Lizzit, Rosanna Larciprete, Paolo Lacovig, Matteo Dalmiglio, Fabrizio Orlando, Alessandro Baraldi, Lauge Gammelgaard, Lucas Barreto, Marco Bianchi, Edward Perkins, et al. Transfer-free electrical insulation of epitaxial graphene from its metal substrate. *Nano Letters*, 12(9):4503–4507, 2012.
- [66] Daniel Löffler, John J Uhlrich, M Baron, Bing Yang, Xin Yu, Leonid Lichtenstein, Lars Heinke, Christin Büchner, Markus Heyde, Shamil Shaikhutdinov, et al. Growth and structure of crystalline silica sheet on Ru (0001). *Physical Review Letters*, 105(14):146104, 2010.
-



- 
- [67] Renzhi Ma and Takayoshi Sasaki. Two-dimensional oxide and hydroxide nanosheets: controllable high-quality exfoliation, molecular assembly, and exploration of functionality. *Accounts of Chemical Research*, 48(1):136–143, 2014.
- [68] Yuqiang Ma, Bilu Liu, Anyi Zhang, Liang Chen, Mohammad Fathi, Chenfei Shen, Ahmad N Abbas, Mingyuan Ge, Matthew Mecklenburg, and Chongwu Zhou. Reversible Semiconducting-to-Metallic Phase Transition in Chemical Vapor Deposition Grown Monolayer WSe<sub>2</sub> and Applications for Devices. *ACS Nano*, 9(7):7383–7391, 2015.
- [69] John E Mahan, Kent M Geib, GY Robinson, and Robert G Long. A review of the geometrical fundamentals of reflection high-energy electron diffraction with application to silicon surfaces. *Journal of Vacuum Science & Technology A*, 8(5):3692–3700, 1990.
- [70] Kin Fai Mak, Changgu Lee, James Hone, Jie Shan, and Tony F Heinz. Atomically thin MoS<sub>2</sub>: a new direct-gap semiconductor. *Physical Review Letters*, 105(13):136805, 2010.
- [71] Shashank Mathur, Sergio Vlaic, Eduardo Machado-Charry, Anh-Duc Vu, Valérie Guisset, Philippe David, Emmanuel Hadji, Pascal Pochet, and Johann Coraux. Degenerate epitaxy-driven defects in monolayer silicon oxide on ruthenium. *Physical Review B*, 92(16):161410, 2015.
- [72] J-S McEwen, SH Payne, and Cathy Stampfl. Phase diagram of O/Ru (0001) from first principles. *Chemical Physics Letters*, 361(3):317–320, 2002.
- [73] K Meinel, H Wolter, Ch Ammer, A Beckmann, and H Neddermeyer. Adsorption stages of O on Ru (0001) studied by means of scanning tunnelling microscopy. *Journal of Physics: Condensed Matter*, 9(22):4611, 1997.
- [74] Lei Meng, Rongting Wu, Haitao Zhou, Geng Li, Yi Zhang, Linfei Li, Yeliang Wang, and H-J Gao. Silicon intercalation at the
-

- 
- interface of graphene and Ir (111). *Applied Physics Letters*, 100(8):083101, 2012.
- [75] Lei Wang Meng, Yeliang Zhang, Lizhi Du, Shixuan Wu, Rongting Li, Linfei Zhang, Yi Li, Geng Zhou, Haitao Hofer, Werner A. Gao, Hong-Jun Meng, Lei Wang, Yeliang Zhang, Lizhi Du, Shixuan Wu, Rongting Li, Linfei Zhang, Yi Li, Geng Zhou, Haitao Hofer, Werner A. Gao, and Hong-Jun. Buckled Silicene Formation on Ir(111). *Nano Letters*, 13:685, 2012.
- [76] V Meunier and Ph Lambin. Tight-binding computation of the STM image of carbon nanotubes. *Physical Review Letters*, 81(25):5588, 1998.
- [77] Alessandro Molle, Carlo Grazianetti, Daniele Chiappe, Eugenio Cinquanta, Elena Cianci, Grazia Tallarida, and Marco Fanciulli. Hindering the oxidation of silicene with non-reactive encapsulation. *Advanced Functional Materials*, 23(35):4340–4344, 2013.
- [78] AH Castro Neto, F Guinea, NMR Peres, Kostya S Novoselov, and Andre K Geim. The electronic properties of graphene. *Reviews of modern physics*, 81(1):109, 2009.
- [79] Kostya S Novoselov, Andre K Geim, SV Morozov, D Jiang, Y Zhang, SV Dubonos, , IV Grigorieva, and AA Firsov. Electric field effect in atomically thin carbon films. *Science*, 306(5696):666–669, 2004.
- [80] KS Novoselov, D Jiang, F Schedin, TJ Booth, VV Khotkevich, SV Morozov, and AK Geim. Two-dimensional atomic crystals. *Proceedings of the National Academy of Sciences of the United States of America*, 102(30):10451–10453, 2005.
- [81] Minoru Osada and Takayoshi Sasaki. Two-dimensional dielectric nanosheets: Novel nanoelectronics from nanocrystal building blocks. *Advanced Materials*, 24(2):210–228, 2012.
- [82] AL Patterson. The Scherrer formula for X-ray particle size determination. *Physical Review*, 56(10):978, 1939.
-

- 
- [83] Linus Pauling. The nature of silicon-oxygen bonds. *American Mineralogist*, 65:321–323, 1980.
- [84] Karin M Rabe. Nanoelectronics: New life for the 'dead layer'. *Nature Nanotechnology*, 1(3):171–172, 2006.
- [85] Karsten Reuter, Catherine Stampfl, M Verónica Ganduglia-Pirovano, and Matthias Scheffler. Atomistic description of oxide formation on metal surfaces: the example of ruthenium. *Chemical Physics Letters*, 352(5):311–317, 2002.
- [86] Ferdaous Ben Romdhane. *Synthèse et caractérisation de nouvelles phases bidimensionnelles par microscopie électronique in-situ*. PhD thesis, Institut Néel, 2015.
- [87] Nicolas Rougemaille, AT N'Diaye, Johann Coraux, Chi Vo-Van, Olivier Fruchart, and AK Schmid. Perpendicular magnetic anisotropy of cobalt films intercalated under graphene. *Applied Physics Letters*, 101(14):142403, 2012.
- [88] Th Schroeder, M Adelt, B Richter, M Naschitzki, M Bäumer, and H-J Freund. Growth of well-ordered silicon dioxide films on Mo (112). *Microelectronics Reliability*, 40(4):841–844, 2000.
- [89] Th Schröder, A Hammoudeh, M Pykavy, N Magg, M Adelt, M Bäumer, and H-J Freund. Single crystalline silicon dioxide films on Mo (112). *Solid-State Electronics*, 45(8):1471–1478, 2001.
- [90] Thomas Schröder, Javier B Giorgi, Marcus Bäumer, and H-J Freund. Morphological and electronic properties of ultrathin crystalline silica epilayers on a Mo (112) substrate. *Physical Review B*, 66(16):165422, 2002.
- [91] Stefan Schumacher, Daniel F Förster, Malte Rösner, Tim O Wehling, and Thomas Michely. Strain in epitaxial graphene visualized by intercalation. *Physical review letters*, 110(8):086111, 2013.
-

- 
- [92] Shamil Shaikhutdinov and Hans-Joachim Freund. Ultrathin silica films on metals: The long and winding road to understanding the atomic structure. *Advanced Materials*, 25(1):49–67, 2013.
- [93] Shamil Shaikhutdinov and Hans-Joachim Freund. Ultra-thin silicate films on metals. *Journal of Physics: Condensed Matter*, 27(44):443001, 2015.
- [94] Sheh-Yi Sheu and Dah-Yen Yang. Gap opening and tuning of the electronic instability in an intercalated bilayer graphene. *Carbon*, 71:76–86, 2014.
- [95] Y Shingaya, T Nakayama, and M Aono. Carbon nanotube tip for scanning tunneling microscopy. *Physica B: Condensed Matter*, 323(1):153–155, 2002.
- [96] Marek Sierka, Tanya K Todorova, Joachim Sauer, Sarp Kaya, Dario Stacchiola, Jonas Weissenrieder, Shamil Shaikhutdinov, and H Freund. Oxygen adsorption on Mo (112) surface studied by ab initio genetic algorithm and experiment. *Journal of Chemical Physics*, 126(23):234710, 2007.
- [97] Catherine Stampfl, HJ Kreuzer, SH Payne, H Pfnür, and Matthias Scheffler. First-principles theory of surface thermodynamics and kinetics. *Physical Review Letters*, 83(15):2993, 1999.
- [98] Catherine Stampfl and Matthias Scheffler. Theoretical study of O adlayers on Ru (0001). *Physical Review B*, 54(4):2868, 1996.
- [99] Catherine Stampfl, S Schwegmann, Herbert Over, Matthias Scheffler, and Gerhard Ertl. Structure and stability of a high-coverage (1× 1) oxygen phase on Ru (0001). *Physical Review Letters*, 77(16):3371, 1996.
- [100] AJ Stone and DJ Wales. Theoretical studies of icosahedral C<sub>60</sub> and some related species. *Chemical Physics Letters*, 128(5):501–503, 1986.

- 
- [101] Xu-Hui Sun, Chi-Pui Li, Wing-Kwong Wong, Ning-Bew Wong, Chun-Sing Lee, Shuit-Tong Lee, and Boon-Keng Teo. Formation of silicon carbide nanotubes and nanowires via reaction of silicon (from disproportionation of silicon monoxide) with carbon nanotubes. *Journal of the American Chemical Society*, 124(48):14464–14471, 2002.
- [102] Peter Sutter, Jerzy T Sadowski, and Eli Sutter. Graphene on Pt (111): Growth and substrate interaction. *Physical Review B*, 80(24):245411, 2009.
- [103] Peter Sutter, Jerzy T Sadowski, and Eli A Sutter. Chemistry under cover: tuning metal- graphene interaction by reactive intercalation. *Journal of the American Chemical Society*, 132(23):8175–8179, 2010.
- [104] Kyozauro Takeda and Kenji Shiraishi. Theoretical possibility of stage corrugation in Si and Ge analogs of graphite. *Physical Review B*, 50(20):14916, 1994.
- [105] R Temirov and FS Tautz. Scanning tunnelling microscopy with single molecule force sensors. In *Noncontact Atomic Force Microscopy*, pages 275–301. Springer, 2015.
- [106] J Tersoff and DR Hamann. Theory of the scanning tunneling microscope. In *Scanning Tunneling Microscopy*, pages 59–67. Springer, 1985.
- [107] Tanya K Todorova, Marek Sierka, Joachim Sauer, Sarp Kaya, Jonas Weissenrieder, J-L Lu, H-J Gao, Shamil Shaikhutdinov, and H-J Freund. Atomic structure of a thin silica film on a Mo (112) substrate: A combined experimental and theoretical study. *Physical Review B*, 73(16):165414, 2006.
- [108] D Van Dyck, G Van Tendeloo, and S Amelinckx. Diffraction effects due to a single translation interface in a small crystal. *Ultramicroscopy*, 15(4):357–370, 1984.
- [109] G Vitins and Keld West. Lithium intercalation into layered limno<sub>2</sub>. *Journal of the Electrochemical Society*, 144(8):2587–2592, 1997.

- 
- [110] Patrick Vogt, Paola De Padova, Claudio Quaresima, Jose Avila, Emmanouil Frantzeskakis, Maria Carmen Asensio, Andrea Resta, Bénédicte Ealet, and Guy Le Lay. Silicene: compelling experimental evidence for graphene-like two-dimensional silicon. *Physical Review Letters*, 108(15):155501, 2012.
- [111] Qing Hua Wang, Kouros Kalantar-Zadeh, Andras Kis, Jonathan N Coleman, and Michael S Strano. Electronics and optoelectronics of two-dimensional transition metal dichalcogenides. *Nature Nanotechnology*, 7(11):699–712, 2012.
- [112] Rong Wang, Xiaodong Pi, Zhenyi Ni, Yong Liu, Shisheng Lin, Mingsheng Xu, and Deren Yang. Silicene oxides: formation, structures and electronic properties. *Scientific Reports*, 3, 2013.
- [113] Jonas Weissenrieder, Sarp Kaya, J-L Lu, H-J Gao, Shamil Shaikhutdinov, H-J Freund, Marek Sierka, Tanya K Todorova, and Joachim Sauer. Atomic structure of a thin silica film on a Mo(112) substrate: A two-dimensional network of SiO<sub>4</sub> tetrahedra. *Physical Review Letters*, 95(7):076103, 2005.
- [114] Martin Weser, EN Voloshina, Karsten Horn, and Yu S Dedkov. Electronic structure and magnetic properties of the graphene/Fe/Ni (111) intercalation-like system. *Physical Chemistry Chemical Physics*, 13(16):7534–7539, 2011.
- [115] Roland Wiesendanger and Hans-Joachim Güntherodt. *Scanning tunneling microscopy III: theory of STM and related scanning probe methods*, volume 29. Springer Science & Business Media, 2013.
- [116] JA Wilson and AD Yoffe. The transition metal dichalcogenides discussion and interpretation of the observed optical, electrical and structural properties. *Advances in Physics*, 18(73):193–335, 1969.
- [117] J Wintterlin, J Trost, S Renisch, R Schuster, T Zambelli, and G Ertl. Real-time STM observations of atomic equilibrium fluctuations in an adsorbate system: O/Ru (0001). *Surface Science*, 394(1):159–169, 1997.

- 
- [118] Xueping Xu and DW Goodman. New approach to the preparation of ultrathin silicon dioxide films at low temperatures. *Applied physics letters*, 61(7):774–776, 1992.
- [119] Bing Yang, Jorge Anibal Boscoboinik, Xin Yu, Shamil Shaikhutdinov, and Hans-Joachim Freund. Patterned defect structures predicted for graphene are observed on single-layer silica films. *Nano Letters*, 13(9):4422–4427, 2013.
- [120] Bing Yang, Emre Emmez, WE Kaden, Xin Yu, Jorge Anibal Boscoboinik, Martin Sterrer, S Shaikhutdinov, and H-J Freund. Hydroxylation of metal-supported sheet-like silica films. *The Journal of Physical Chemistry C*, 117(16):8336–8344, 2013.
- [121] Bing Yang, William E Kaden, Xin Yu, Jorge Anibal Boscoboinik, Yulia Martynova, Leonid Lichtenstein, Markus Heyde, Martin Sterrer, Radosław Włodarczyk, Marek Sierka, et al. Thin silica films on Ru(0001): monolayer, bilayer and three-dimensional networks of [SiO<sub>4</sub>] tetrahedra. *Physical Chemistry Chemical Physics*, 14(32):11344–11351, 2012.
- [122] D Yang, S Jiménez Sandoval, WMR Divigalpitiya, JC Irwin, and RF Frindt. Structure of single-molecular-layer MoS<sub>2</sub>. *Physical Review B*, 43(14):12053, 1991.
- [123] Oleg V Yazyev and Yong P Chen. Polycrystalline graphene and other two-dimensional materials. *Nature nanotechnology*, 9(10):755–767, 2014.
- [124] Xin Yu. *Ultra-thin silicate films on metal single crystals*. PhD thesis, Technische Universität Berlin, 2013.
- [125] Xin Yu, Bing Yang, Jorge Anibal Boscoboinik, Shamil Shaikhutdinov, and Hans-Joachim Freund. Support effects on the atomic structure of ultrathin silica films on metals. *Applied Physics Letters*, 100(15):151608, 2012.
- [126] Shinji Yuasa, Taro Nagahama, Akio Fukushima, Yoshishige Suzuki, and Koji Ando. Giant room-temperature magnetoresistance in single-crystal Fe/MgO/Fe magnetic tunnel junctions. *Nature Materials*, 3(12):868–871, 2004.

- 
- [127] William Houlder Zachariasen. The atomic arrangement in glass. *Journal of the American Chemical Society*, 54(10):3841–3851, 1932.
- [128] Yi Zhang, Luyao Zhang, and Chongwu Zhou. Review of chemical vapor deposition of graphene and related applications. *Accounts of Chemical Research*, 46(10):2329–2339, 2013.
- [129] Yu Zhang, Yanfeng Zhang, Qingqing Ji, Jing Ju, Hongtao Yuan, Jianping Shi, Teng Gao, Donglin Ma, Mengxi Liu, Yubin Chen, et al. Controlled growth of high-quality monolayer WS<sub>2</sub> layers on sapphire and imaging its grain boundary. *ACS Nano*, 7(10):8963–8971, 2013.
- [130] Huijuan Zhao. Strain and chirality effects on the mechanical and electronic properties of silicene and silicane under uniaxial tension. *Physics Letters A*, 376(46):3546–3550, 2012.
- [131] Wu Zhou, Xiaolong Zou, Sina Najmaei, Zheng Liu, Yumeng Shi, Jing Kong, Jun Lou, Pulickel M Ajayan, Boris I Yakobson, and Juan-Carlos Idrobo. Intrinsic structural defects in monolayer molybdenum disulfide. *Nano Letters*, 13(6):2615–2622, 2013.



## **Shashank Mathur**

*Institute Neel- CNRS*

*F-38042 Grenoble France*

*Phone: +33 7 61 94 61 57*

*Email: shashank.mathur@neel.cnrs.fr  
mathur.shashank07@gmail.com*

*Date of Birth: 07<sup>th</sup> October 1988*

*Nationality: Indian*

*Languages: Hindi, English, French (A2)*

## **PUBLICATIONS**

### ***Degenerate epitaxy driven defects in monolayer silicon oxide on ruthenium***

**Mathur, S.**, Vlaic, S., Machado-Charry, E., Vu, A.-D., Guisset, V., David, P., Hadji, E., Pochet, P., Coraux, J. **Phys Rev B 92, 161410(R) (2015)** .

### ***Strain relaxation in CVD Graphene: Wrinkling with shear lag***

Bronsgeest, M. S., Bendiab, N., **Mathur, S.**, Kimouche, A., Johnson, H. T., Coraux, J., Pochet, P. **Nano Letters 15(8) 55098-5104 (2015)**

## **EDUCATION**

**University of Grenoble Alps, France**

**2013-2016**

- PhD in Material Science (pursuing)

(expected)

**Amity University NOIDA, India**

**2007-2013**

- Master of Technology in Nanotechnology (Materials & Devices); GPA: **8.21/10**  
-An engineering degree

## **RESEARCH EXPERIENCE**

**Institute Neel-CNRS Grenoble & CEA-INAC-SP2M Grenoble France**

**PhD Research**

Thesis Title: “***Growth and characterization of bi-dimensional materials based on silicon and oxygen***”

Supervisor: *Dr. Johann Coraux*

Co-Supervisor: *Dr. Pascal Pochet*

Results: *Epitaxial growth of two-dimensional crystalline silicon oxide; atomic structure, growth mechanism and defect formation unveiled by surface scrutiny (by STM, RHEED).*

Outcomes: Phys. Rev. B 92 161410R (2015)

Research Grant: **Laboratory of Excellence LANEF-Grenoble**

**CEA-INAC-SP2M Grenoble France**

**Master’s Thesis**

Master’s Thesis Title: “***Growth and characterization of graphene-like bi-dimensional materials***”

Supervisor: *Dr. Thomas Charvolin;*

Co-Supervisor: *Dr. Merijntje Bronsgeest*

**National Physical Laboratory New Delhi &**

**Amity Institute of Nanotechnology NOIDA India**

**Term Project**

Thesis Title: “***Surface potential measurement of modified interfaces in organic light emitting diodes (OLEDs)***”

Supervisor: *Dr. O. P. Sinha;*

Co-Supervisor: *Dr. Ritu Srivastava*

## SUMMER INTERNSHIP & SHORT TERM PROJECTS

- **Larsen & Tubro (LnT) Mumbai India**  
*“Development of Nanocomposite Radomes”*
- **Amity Institute of Nanotechnology, NOIDA India**  
*“Slow and effective release of di-ethyl phenyl acetamide”*  
Supervisor: Dr. Arpita Bhattacharya

## CONFERENCES

- « **Growth and structure of monolayer silicon oxide on ruthenium** » talk at European Workshop on Epitaxial Graphene and 2D 2016, Cologne Germany
- « **2D phase of Silicon Oxide: Structure, Registry & Defects** » talk at GDR-GNT Meeting 2015, Aussois France
- « **Formation of anti phase domain boundaries in two dimensional crystalline silicon oxide** » oral talk at European Conference on Surface Sciences (ECOSS) 2015, Barcelona Spain
- « **Emergence and control of crystalline domains in two-dimensional silica** » oral talk accepted at American Physical Society (APS) March Meeting 2015, San Antonio Texas USA
- « **Emergence and control of crystalline domains in two-dimensional silica** » poster presentation at European Material Research Society (E-MRS) spring meeting 2015, Lille France  
**Awarded Best Poster Prize**
- « **Domain formation and engineering in 2D crystalline silica** » poster at Graphene at Grenoble meeting 2014, Grenoble France
- « **Surface potential measurements of modified interfaces in organic light emitting diodes (OLEDs)** » poster presentation at National Symposium on Recent Advances in Nano Sciences, Engineering and Technology 2011, Gwalior India  
**Awarded Best Poster Prize**
- « **Slow and effective release of di-ethyl phenyl acetamide** » poster presentation at International Conference on Nano Science and Technology 2010, Bombay India

## WORKSHOPS AND SUMMER SCHOOLS

- Summer school “Graphene & Co., Frontier Research in Graphene-based Systems”, by GDR-GNT in 2014, Cargèse France
- EICOON school on “Nanomaterials for sustainable energy”, organized by EU-India forum on sustainable energy in 2010, New Delhi India
- International Workshop on Electron Devices and Semiconductor Technology, IEEE-conference 2009, Bombay India
- Indian Nanoelectronics User Program (INUP) Workshop 2, 2009, Bombay India

## COMPETENCIES

- Operation of multi-technique Ultra high vacuum (UHV) ensemble
- Electron diffraction, Scanning tunneling Microscopy (STM), Atomic Force Microscopy (AFM), Raman scattering
- Growth of 2D materials (2D silica and graphene)
- Fabrication of organic light emitting diodes (OLEDs) and photovoltaic devices (OPVs)
- Certified in Technical communication, French as foreign language (A2)

## REFERENCES

Dr. Johann Coraux  
Institut Neel-CNRS  
38042 Rue des Martyrs  
Grenoble France  
johann.coraux@neel.cnrs.fr

Dr. Pascal Pochet  
CEA Grenoble-INAC-SP2M  
38054 Rue des Martyrs  
Grenoble France  
pascal.pochet@cea.fr

Dr. O. P. Sinha  
AINT, Amity University  
Sector-125, NOIDA  
Uttar Pradesh, India  
opsinha@amity.edu

---